

**Thermal Impacts on  
Building Integrated Photovoltaic (BIPV)  
(Electrical, Thermal and Mechanical Characteristics)**

Dissertation zur Erlangung des akademischen Grades  
Doktor der Ingenieurwissenschaften (Dr.-Ing.)

vorgelegt im Fachbereich Elektrotechnik/Informatik  
der Universität Kassel von

**Siwanand Misara**

**Die vorliegende Arbeit wurde vom Fachbereich Elektrotechnik/ /Informatik der Universität Kassel als Dissertation zur Erlangung des akademischen Grades eines Doktors der Ingenieurwissenschaften (Dr.-Ing.) angenommen.**

**Erster Gutachter: Prof. Dr.-Ing. habil. Peter Zacharias**

**Zweiter Gutachter: Dr.-Ing. Norbert Henze**

**Tag der mündlichen Prüfung 06. Oktober 2014**

## Erklärung

„Hiermit versichere ich, dass ich die vorliegende Dissertation selbstständig, ohne unerlaubte Hilfe Dritter angefertigt und andere als die in der Dissertation angegebenen Hilfsmittel nicht benutzt habe. Alle Stellen, die wörtlich oder sinngemäß aus veröffentlichten oder unveröffentlichten Schriften entnommen sind, habe ich als solche kenntlich gemacht. Dritte waren an der inhaltlich-materiellen Erstellung der Dissertation nicht beteiligt; insbesondere habe ich hierfür nicht die Hilfe eines Promotionsberaters in Anspruch genommen. Kein Teil dieser Arbeit ist in einem anderen Promotions- oder Habilitationsverfahren verwendet worden.“

---

Datum, Ort

---

Unterschrift  
(Siwanand Misarsa)

## Acknowledgements

I would like to thank all the people who have accompanied me throughout this thesis:

Prof. Dr.-Ing. Jürgen Schmid and Prof. Dr.-Ing. habil. Peter Zacharias for their valuable supervision and guidance.

Dr.-Ing. Norbert Henze, for giving me the motivation, inspiration and freedom to develop new ideas for this study.

Dr.-Ing. Christian Bendel and Dr.-Ing. Philipp Strauß, for giving me the chance to complete this work.

All my colleagues at Fraunhofer IWES; Peter Funtan, Maria Roos, Dr.-Ing. Thomas Glotzbach, Björn Schulz, Jörg Kirchhof, Gerald Klein, Axel Barahona, Zichuan Zhang and Florian Ackermann, as well as the students for all their support and help.

Prof. Dr.-Ing. Anton Maas, for his co-supervision, encouragement and valuable inspiration and Prof. Dr.-Ing. Thomas Glotzbach, for joining the commission.

I will always be grateful to my family; Shanti, Taywin, Anita, Sujata, Anand Misara together with Somnuk Kuhlmann, Sabo Maslicic, Martin Kuhlmann, Albert and Annegret Jansen for their wonderful love and endless encouragement, especially for giving me the opportunity to follow my dream.

My special thanks to Johanna Kuhlmann, who supported me throughout the thesis, for her patience, her encouragement and her constant support.

Finally, I would like to dedicate this work to my father, Diwakar Misara,

## Abstract

One third of the worldwide total energy demand is represented by building applications. Partially meeting this demand as well as reducing this considerable consumption while still maintaining other relevant building functions, Building Integrated Photovoltaic (BIPV) is one of the most-suited elements for building applications. With respect to a great variety of design possibilities, the boundary conditions of BIPV applications are completely different compared to standard PV applications, especially in terms of operating temperature. Up to now, there has not been much information available about the thermal impact on the electrical power output together with thermal and mechanical relevant building functions. Most manufacturers take these characteristics from standards of conventional PV modules and building products. Hence, the accuracy of the system and building design could not be achieved. Therefore, the investigation of thermal impact on electrical, thermal and mechanical characteristics is the main objective of this work.

At first, the temperature model with power balance concept was developed based on the dynamic and steady simulations, taking into account the different configurations and installation possibilities of the module. With regard to dynamic simulation, the real-time power output and energy yield can be achieved together with real-time building simulation. For steady state simulation, the relevant building functions of the BIPV modules can be obtained during summer and winter periods. Moreover, the model for mechanical characteristics was developed using various thermal and mechanically induced load scenarios together with a variation of load duration, a mounting system and encapsulation materials.

To validate the temperature and mechanical models, different test equipment was developed together with new test methods. By applying the test equipment “PV variable mounting system” and “mechanical testing equipment”, three key elements were emulated: the varying scenarios of mounting systems, multi-layered configurations, and mechanical loads. Additionally, it was possible to obtain the solar irradiation as well as certain operating temperatures with the new test method “back-bias current concept”.

Moreover, with the validated models previously mentioned, electrical, thermal and mechanical behaviour were further evaluated based on other configurations. As a result, these model developments were implemented in the software tools used directly by PV manufacturers.

## Zusammenfassung

Ein Drittel des weltweiten gesamten Energiebedarfs wird durch Gebäude verbraucht. Um diesen Energiebedarf teilweise zu decken, den erheblichen Energieverbrauch zu reduzieren und weiterhin andere Gebädefunktionen beizubehalten, ist Gebäudeintegrierte Photovoltaik (BIPV) eine der am besten geeigneten Lösungen für die Gebäudenanwendung. Im Bezug auf eine Vielzahl von Gestaltungsmöglichkeiten, sind die Randbedingungen der BIPV-Anwendungen eindeutig anders im Vergleich zu Standard-PV-Anwendungen, insbesondere bezüglich der Betriebstemperatur. Bisher gab es nicht viele Informationen zu den relevanten thermischen Auswirkungen auf die entsprechenden elektrischen Eigenschaften zusammen mit thermischen und mechanischen relevanten Gebäudenfunktionen. Die meisten Hersteller übernehmen diese Eigenschaften von entsprechenden PV-Modulen und konventionellen Bauprodukten Normen, die zur ungenauen System- und Gebäudeplanungen führen. Deshalb ist die Untersuchung des thermischen Einflusses auf elektrische, thermische sowie mechanische Eigenschaften das Hauptziel der vorliegenden Arbeit.

Zunächst wird das Temperatur-Model mit dem Power-Balance-Konzept erstellt. Unter Berücksichtigung der variablen Installationsmöglichkeiten und Konfigurationen des Moduls wird das Model auf Basis dynamischer und stationär Eigenschaften entwickelt. Im Hinblick auf die dynamische Simulation können der Energieertrag und Leistung zusammen mit der thermischen Gebäudesimulation in Echtzeit simuliert werden. Für stationäre Simulationen können die relevanten Gebäudenfunktionen von BIPV-Modulen sowohl im Sommer als auch im Winter simuliert werden. Basierend auf unterschiedlichen thermischen und mechanischen Last-Szenarien wurde darüber hinaus das mechanische Model zusammen mit Variationen von Belastungsdauer, Montagesystem und Verkapselungsmaterialien entwickelt.

Um die Temperatur- und Mechanik-Modelle zu validieren, wurden die verschiedenen Prüfeinrichtungen zusammen mit neuen Testmethoden entwickelt. Bei Verwendung der Prüfanlage „PV variable mounting system“ und „mechanical testing equipment“ werden zudem die verschiedenen Szenarien von Montagesystemen, Modul-Konfigurationen und mechanischen Belastungen emuliert. Mit der neuen Testmethode „back-bias current concept“ können zum einen die solare Einstrahlung und bestimmte Betriebstemperaturen eingestellt werden.

Darüber hinaus wurden mit den eingangs erwähnten validierten Modellen das jeweilige elektrische, thermische und mechanische Verhalten auf andere Konfigurationen bewertet. Zum Abschluss wird die Anwendung von Software-Tools bei PV-Herstellern im Hinblick auf die entsprechenden Modellentwicklungen thematisiert.

# Content

Acknowledgements .....	iv
Abstract .....	v
Zusammenfassung .....	vi
Content .....	vii
List of Figures .....	x
List of Tables .....	xiv
Nomenclature .....	xvi
1. Introduction .....	1
2. State of the Art and Technical Limits.....	3
2.1 Electrical Aspect .....	3
2.2 Thermal Aspect .....	5
2.3 Mechanical Aspect: .....	8
2.4 Objective .....	11
3. Temperature Model.....	13
3.1 State of the Art Temperature Models.....	13
3.1.1 NOCT-Model .....	13
3.1.2 Explicit Methods .....	14
3.1.3 Implicit Methods .....	17
3.2 Deficits on BIPV application .....	18
3.3 Real-Time Power Balance Model .....	21
3.3.1 Input Power .....	22
3.3.2 Electrical Power .....	28
3.3.3 Dissipation Power.....	31
3.3.4 Absorption Power .....	42
4. Mechanical Models .....	45
4.1 Physical parameters .....	45
4.2 Interlayer Properties .....	47
4.2.1 Shear Strength of the Polymeric Interlayer.....	47
4.2.2 Mechanical Models for the Interlayer.....	52

4.2.3	Determination of the Shear Modulus of Thermoplastic.....	54
4.3	Other influenced parameters .....	57
4.4	Legal allowance .....	58
4.5	Mechanical Modelling .....	59
4.5.1	Finite Element Modeling .....	59
4.5.2	Mathematic Mechanical Model .....	62
5.	Experimental Infrastructures .....	66
5.1	Outdoor Test Infrastructures.....	66
5.1.1	Solar Irradiation Measurement .....	66
5.1.2	Real-time Outdoor PV Module Measurement.....	67
5.2	Indoor Test Infrastructures .....	69
5.2.1	Back-bias Current Concept .....	69
5.2.2	PV Variable Mounting Equipment .....	72
5.2.3	Mechanical testing equipment.....	76
6.	Validation .....	81
6.1	Solar irradiation .....	82
6.1.1	Inclined Solar Irradiation Conversion Models .....	82
6.1.2	Distribution of Solar Irradiation .....	84
6.2	Thermal dissipation .....	86
6.2.1	Variable Operating Temperatures .....	86
6.2.2	Variable tilted angle.....	88
6.2.3	Variable gaps behind the panels .....	93
6.3	Electrical power and energy yields .....	94
6.4	Mechanical Behaviour .....	98
6.4.1	Standard-conform mounting system with PV-laminated glass .....	100
6.4.2	Manufacturer-conform mounting system with PV-laminated glass.....	105
6.4.3	Manufacturer-conform mounting system with PV-glass-backsheet.....	108
7	Evaluation .....	110
7.1	Power Dissipation components .....	110
7.1.1	Radiation heat transfer coefficient.....	110
7.1.2	Convection heat transfer coefficient .....	112



7.2	Thermal relevant building function.....	115
7.3	Mechanical Behaviour .....	120
7.3.1	Load scenarios.....	120
7.3.2	Mechanical evaluation.....	121
7.4	Software development.....	125
7.4.1	PV-Therm.....	125
7.4.2	PV-Mech .....	126
8	Conclusion .....	128
9	Outlook.....	133
10	Reference.....	135

## List of Figures

Figure 2-1	Thermal parameters of building products: U- and g-values.	6
Figure 2-2	Deflection behavior and stress distribution of (a) multilayer glasses without bond, (b) monolithic glass and (c) laminated glass.	9
Figure 3-1	Real-Time Power Balance Model concept	22
Figure 3-2	Correlation of zenith angle ( $\theta_z$ ), angle of incident ( $\theta_{in}$ ), PV module tilt angle ( $\alpha_{PV}$ ) and PV module azimuth angle ( $\beta_{PV}$ ).	23
Figure 3-3	Direct spectrum distribution at different AMs	25
Figure 3-4	Direct and diffuse solar spectral irradiance at different air mass	25
Figure 3-5	Equivalent circuit of 1- and 2-diode models together with their IV-curve equations.	28
Figure 3-6	spectrum response of each PV technology (a) and influence of solar spectral variation for different PV technologies, relative to the AM 1.5.	30
Figure 3-7	Holistic approach of convection heat transfer coefficients	34
Figure 3-8	Flow chart of natural convection with free ventilation at different tilted angles	35
Figure 3-9	Flow chart of natural convection in channel at different tilted angles	37
Figure 3-10	Flow chart of forced convection	39
Figure 3-11	Equivalent electrical circuit flow of heat transfer resistances together with temperature gradient from PV cell to ambient temperature	40
Figure 3-12	Time-delay operating temperatures to fluctuated solar irradiation	43
Figure 4-1	Compression/Tensile stress ( $\sigma$ ) and shear stress ( $\tau$ )	45
Figure 4-2	Deflection of object under load	46
Figure 4-3	Schematic dependency of the shear storage modulus of thermoplastics on temperature	48
Figure 4-4	Thermo-mechanic behaviour of various polymeric interlayer materials used in glass and PV industry	49
Figure 4-5	Creep and relaxation characteristics of interlayers.	50
Figure 4-6	Storage modulus of different interlayers with and without solar cell strings.	50
Figure 4-7	Creep characteristics of PVB based on different operating temperature over time	51

Figure 4-8	Relaxation characteristic of EVA based different operating temperatures over time	52
Figure 4-9	Rheological behaviour [Hooke element and Newton element]	53
Figure 4-10	Maxwell model, Kelvin-Voigt model and Burgers model	53
Figure 4-11	Shear modulus curve [Bennison, Jagota, Duser]	55
Figure 4-12	Graph of PVB-shear stiffness modulus against load duration, based on experimental data	56
Figure 4-13	Deformation behaviour and main stress directions of slabs supported on - a) four sides b) two sides c) four fixing points.	58
Figure 4-14	Simulation of bending stress and deflection of the PV modules (1200x1000 mm) for PVB interlayer under different PV multi-layered configuration and load scenarios.	61
Figure 5-1	ISETSensor Global at Fraunhofer IWES	67
Figure 5-2	PV module types at Fraunhofer IWES (PV-Testlab; front and backside	68
Figure 5-3	Equivalent circuit of PV Cell characteristic under solar irradiation (a) and without solar irradiation (b).	70
Figure 5-4	Heat flux plate (a), thermistor (b) and wind sensor (c)	74
Figure 5-5	Schematic of heat flux measurement together with surface and surrounding temperature measurement and wind sensor on both outside and inside	74
Figure 5-6	(a) Test infrastructure of feed-in thermal power with polycrystalline PV module and external power supply	75
Figure 5-7	Test bench with different ventilation system configuration; free-standing variable gaps and full-integrated configurations.	76
Figure 5-8	a) Wheatstone bridge connection together with strain calculation	78
Figure 5-9	Displacement sensor with product specification	79
Figure 5-10	Mechanical testing equipment with implementation of displacement sensor	80
Figure 6-1	Deviation of solar irradiation between conversion models and measured data in MBD and RMSD methods together with variation of angle of incident ( $\theta_{in}$ ) and zenith angles ( $\theta_z$ ) for 30°-South (a), 90°-South (b), 90°-East (c) and 90°-West (d) orientations.	83

Figure 6-2	Weighting factors of solar irradiation at different orientations compared to weighting factor at $\eta_{EU,new}$ obtained by in EN 50530	85
Figure 6-3	(a) operating temperature of conventional glass and PV Module with different solar irradiation, (b) heat transfer coefficient of PV module with different solar irradiances	87
Figure 6-4	Total heat transfer coefficients of PV-laminated glass and PV building element configurations on different tilted angles	93
Figure 6-5	Simulation and measurement of operating temperature of PV module and PV-composite element in summer (a) and in winter (b).	96
Figure 6-6	Simulation of operating temperature between with and without consideration of heat capacity of PV module in compared to the measurement of module temperature.	97
Figure 6-7	Simulated internal and external heat transfer coefficients;	98
Figure 6-8	Bending Strain at 40°C with own load, without applied mechanical load	101
Figure 6-9	Deflection at 40 °C with own load, without applied mechanical load.	101
Figure 6-10	Bending strain at 100% and 50% mechanical load for 20 minutes.	102
Figure 6-11	Deflection from 100% of mechanical load applied for 20 minute.	102
Figure 6-12	Combined bending strain from temperature at 40 °C with 75% of mechanical load and temperature at 60 °C with 50% of mechanical load for 20 minutes duration.	103
Figure 6-13	Deflection at temperature at 40 °C with 75% of mechanical load and temperature at 60 °C with 50% of mechanical load for 20 minutes duration.	104
Figure 6-14	Combined bending strain at temperature at 40 °C with 75% of mechanical load and temperature at 60 °C with 50% of mechanical load for 1 hour duration.	105
Figure 6-15	Deflection at temperature at 40 °C with 75% of mechanical load and temperature at 60 °C with 50% of mechanical load for 1 hour duration.	105
Figure 6-16	Bending strain at room temperature with 100% of mechanical load for 20 minutes.	106
Figure 6-17	Combined bending strain at temperature at 40° with 75% of mechanical load for 1 hour duration.	107

Figure 6-18	Bending strain at room temperature with 100% mechanical load for 20 min.	108
Figure 6-19	Bending strain at 60 °C, without mechanical load.	109
Figure 7-1	Radiation heat transfer coefficient on front- and backside of PV module with different backside emissivity at different tilt angles and temperature differences.	111
Figure 7-2	Wind speed at Fraunhofer IWES over 1 year with 15-sec time	113
Figure 7-3	Nusselt-number and heat transfer coefficient of natural and forced convection at different multi-layered configuration and wind speed, respectively.	113
Figure 7-4	Heat transfer coefficient of natural convection in channels at different distances and tilt angles.	114
Figure 7-5	Calculation methods for identify the U-value and secondary heat transfer coefficient emitted inside under consideration of percentage of PV cell coverage	118
Figure 7-6	Bending stress and deflection of laminated glass with PVB interlayer at different operating temperature and load duration; Dependency on operating temperature (a, b), Dependency on load duration (c, d)	122
Figure 7-7	Bending stress of monolithic glass (a) and laminated glass (b) under different load scenarios.	123
Figure 7-8	Bending stress and deflection of laminated glass with PVB and EVA interlayers at low operating temperature; (a) bending stress, (b) deflection	124
Figure 7-9	Mechanical behaviors (bending stress and deflection) of laminated glass with EVA and PVB interlayers at high operating temperature; with short load duration (a, b), with long load duration (c, d)	125
Figure 7-10	Graphic user interface of thermal relevant building function software (PV-Therm)	126
Figure 7-11	Graphic user interface of mechanical relevant building function software (PV-Mech)	127
Figure 7-12	Display of bending stress and deflection of certain multi-layered configuration.	127

## List of Tables

Table 3-1	Parameter b in Sauer model based on Germany locations	15
Table 3-2	Parameter k for PV-SOL Software (a) and SolEm (b)	15
Table 3-3	Parameter k for Sandia-SNL-Model	16
Table 3-4	Parameters a and b for empirically-based thermal SNL Model and temperature difference between cell and backside surface temperature ( $\Delta T$ )	16
Table 3-5	Example for variation of parameters $a_i$ and $b_i$ versus wind speed	17
Table 3-6	Calculation of zenith angles ( $\theta_z$ ), Air Mass (AM) and angle of incident ( $\theta_{in}$ ).	24
Table 3-7	Diffuse irradiation models on inclined surface; Jordan, Klucher, Hay and Reindl Models	27
Table 3-8	Short circuit current, power output, open circuit voltage and maximum voltage versus solar irradiation and temperature	30
Table 3-9	Material parameters of BIPV-Modules	32
Table 3-10	Radiation heat transfer coefficients; 2 parallel plates and surface-to surrounding	33
Table 3-11	Calculation of thermal power dissipation on both front- and backside	41
Table 4-1	Shear modulus of EVA	56
Table 4-2	Bending stress limits for various glass types in N/mm <sup>2</sup>	58
Table 4-3	Deflection limits for various types of glass.	59
Table 4-4	a) different module dimension with different multi-layered configuration and load scenarios	60
Table 4-5	Calculation of stress and deflection for monolithic (a), multilayer glass without bond (b) together with laminated glass (c)	64
Table 4-6	Parameters for shear and stiffness	64
Table 4-7	Parameter k1 and k2 for different mounting systems; 2-sided clamped, 4-sided clamped, 4-point fixing.	65
Table 5-1	Physical parameters of material used in PV-modules.	68
Table 5-2	module types with their specification	68
Table 5-3	PV-Module characteristics	71
Table 5-4	Feed-in thermal power with different solar irradiation from conventional glazing and PV Modules	72
Table 5-5	Variable possibilities in PV variable mounting equipment; multi-layered configuration and tilted angles	72

Table 5-6	Variable parameters in mechanical testing equipment	76
Table 6-1	Weighting factors of different orientations and the $\eta_{EU,new}$ in weak-light range, from 0 – 375 W/m <sup>2</sup>	85
Table 6-2	Comparison of heat transfer coefficient from EN 410, ISO 6946, Models and measurement for conventional glazing and PV modules at different solar irradiation at vertical installation	88
Table 6-3	Measured operating temperatures and heat transfer coefficients together with simulated heat transfer coefficients on both front- and backside of PV modules.	89
Table 6-4	Simulated of total heat transfer coefficients of both front- and backside together with composition of each natural and forced convection and radiation heat transfer coefficients.	90
Table 6-5	Measured operating temperature and external heat transfer coefficient together with simulated external heat transfer coefficients	92
Table 6-6	Measurement of operating temperature of PV module at backside and wall temperature and total gap heat transfer coefficient ( $h_{i,gap}$ ) together with corresponding simulated heat transfer coefficients.	94
Table 6-7	Mechanical test scenarios for validation of self-weight, operating temperature and load duration.	99
Table 7-1	Boundary conditions for determination U-value, g-value and Fc-value in summer and winter	116
Table 7-2	Operating temperature, surface temperature and thermal	117
Table 7-3	Comparison of simulated heat transfer coefficient (U-value) of different PV multi-layered configurations under consideration of new PV-specific thermal parameters and different percentage of PV cell coverage based on a validated model	119
Table 7-4	Comparison of simulated solar heat gain (g-value) in winter and summer under consideration of new PV-specific thermal parameters and different percentage of PV cell coverage based on validated model	119
Table 7-5	Wind load scenarios for the design of laminated glass	121

## Nomenclature

$P_{elec}$	= power output (W)
$E_{elec}$	= energy yield (Wh)
$G$	= global irradiation (W/m <sup>2</sup> )
$G_0$	= extraterrestrial solar irradiation ( $G_0=1367$ W/m <sup>2</sup> ).
$G_T$	= global irradiation on tilted angle (W/m <sup>2</sup> )
$G_b$	= beam solar irradiation (W/m <sup>2</sup> )
$G_d$	= diffuse solar irradiation (W/m <sup>2</sup> )
$G_r$	= ground reflected solar irradiation (W/m <sup>2</sup> )
$R_b$	= the geometric factor (-)
$AM$	= Air Mass (-)
$A$	= module area (m <sup>2</sup> )
$\eta$	= module efficiency (%)
$\eta_{STC}$	= module efficiency at STC condition (%)
$\eta_c$	= cell efficiency (%)
$\alpha_{coeff}$	= temperature co-efficiency of module (%/K)
$T_M$	= module temperature (K)
$T_{amb}$	= ambient temperature (K)
$T_{STC}$	= temperature at STC (25 °C)
$C_M$	= module heat capacity (J/K)
$U$ -value	= heat transmission coefficient (W/m <sup>2</sup> K)
$g$ -value	= solar heat gain coefficient (-)
$F_c$ -value	= solar reduction ratio (-)
$U_{PV}$	= total heat transmission coefficient of total BIPV element (W/m <sup>2</sup> K).
$\tau$	= transmission factor (-)
$\gamma$	= reflection factor (-)
$\alpha$	= absorption factor (-)
$f$	= front layer
$b$	= back layer
$E$	= Earth
$sky$	= sky
$PV$	= PV layer
$\alpha_{PV}$	= module tilted angle (degree)
$h_{e,i}$	= external and internal heat transfer coefficient (W/m <sup>2</sup> K)
$h_t$	= heat transmission coefficient of each layer in solid material (W/m <sup>2</sup> K)
$d$	= material thickness (m)
$\lambda$	= heat conductivity of material (W/mK)
$h_s$	= heat transmission coefficient of each layer in fluid material (W/m <sup>2</sup> K)



$\theta_{in}$	= angle of solar incident (°)
$SR$	= spectral response (-)
$\theta_z$	= zenith angle (°)
$\gamma_s$	= solar altitude angle (°)
$\beta_s$	= solar azimuth (°) (180° = south)
$\beta_{PV}$	= PV azimuth angle (°) (180° = south)
$\delta$	= declination angle (°)
$\omega$	= hour angles (°)
$\Phi$	= location latitude (°)
$\rho_g$	= average reflectance of the ground (-)
$\varepsilon$	= emissivity of surface (-)
$\sigma$	= Stefan–Boltzmann constant - $5.669 \times 10^{-8} \text{ W}/(\text{m}^2 \text{ K}^4)$
$Ra$	= Rayleigh number (-)
$Pr$	= Prandtl number (-)
$Gr$	= Grashof-number (-)
$g$	= gravity ( $9.81 \text{ m/s}^2$ )
$l$	= module length (m)
$\nu$	= viscosity of fluids
$\Delta\theta$	= temperature differences between surface and surrounding
$\beta$	= average temperature ( $T_{avg}^{-1}$ )
$Nu$	= Nusselt-number
$t_G$	= total glass thickness (mm)
$l_{min}$	= module width (mm)
$l_{max}$	= module length (mm)
$E$	= elasticity of glass ( $\text{N/mm}^2$ )
$\lambda$	= ratio of module width to module length
$\kappa$	= ratio of front glass pane to back glass pane
$\bar{h}$	= ratio of interlayer thickness to total thickness of two glass panes
$\beta_1$	= shear parameter
$\alpha$	= stiffness parameter

# 1. Introduction

One third of the worldwide total energy demand is represented by building applications [WBCSD]. Partially meeting this demand as well as reducing this considerable consumption while still maintaining the comfort of the building, Building Integrated Photovoltaic (BIPV) is one of the best suited elements for building applications. In addition to electric generation from the standard PV module, BIPV has to take on other relevant building functions, for example thermal insulation, noise protection, solar heat gain, etc. [DIN 0126-21]. Therefore, BIPV can also be estimated as multifunctional PV elements. With respect to its multifunctional properties, BIPV, as an element integrated in building envelopes, has to comply with the requirements of building products as defined in the Construction Products Directive [CPD-89/106/EEC];

- Mechanical resistance and stability
- Safety in case of fire
- Hygiene, health and the environment
- Safety in use
- Protection against noise
- Energy economy and heat retention

However, the market penetration of BIPV still remains small scale compared to the fast growing photovoltaic market. Significant obstacles are technical barriers, e.g. electrical, thermal and mechanical aspects, as well as legal and administrative processes [Sunrise-2008].

Up to now, the electrical properties of BIPV have been evaluated based on standard PV modules, while the thermal and mechanical properties of BIPV have been evaluated based on conventional building products. Moreover, the legal and administrative processes are considered based on conventional building products. Nevertheless, the PV specific characteristics have not yet been considered in the above-mentioned aspects. The significant PV specific characteristic is a higher operating temperature, compared to the standard PV module and conventional building products. The operating temperature of roof-integrated PV, PV tiles, can reach 90°C at a solar irradiation of 1000W/m<sup>2</sup>, ambient temperature of 30°C, ventilation rate of 0m/s and backside temperature of 20°C on the backside of the PV tiles [Mei-2009]. Meanwhile, the standard PV module and conventional transparent glazing can reach 50-60°C and 30°C, respectively. This leads to different electrical,

thermal and mechanical properties of BIPV compared to standard modules or conventional building products.

Together with 15 industrial partners, Fraunhofer Institute for Wind Energy and Energy System Technology (IWES) investigated the development of manufacturing, testing and installation methods of multifunctional photovoltaic devices / modules in buildings as a part of the BMU research project "MULTIELEMENT (FKZ 0325067) [Misara-2009]. In this project, the thermal impact on BIPV was investigated, especially the electrical, thermal and mechanical characteristics.

The thesis is structured in 10 chapters. Chapter 2 will review the significant technical barriers for the market penetration of BIPV; electrical, thermal and mechanical aspects. It exhibits the state of the art and limitations of previous mentioned aspects and finish with the objective of this thesis. In order to investigate the thermal impact of BIPV application on electrical, thermal and mechanical behaviors, the temperature and mechanical models will be describing in Chapter 3 and Chapter 4, respectively. Chapter 5 will demonstrate the related testing infrastructures in order to validate the temperature and mechanical models developed in previous chapters. Chapter 6 will present the validation results and chapter 7 will represent the additional evaluation possibilities based on models developed and validated in previous chapters, which will be mainly on thermal and mechanical characteristics of BIPV. Chapter 8 and Chapter 9 will describe the conclusion and future work of this thesis.

## 2. State of the Art and Technical Limits

The BIPV modules are manufactured with different multi-layered configurations (glass-glass, glass-glass-isolation, roof-tile, metal-sheet), orientations (west-east, horizontal-vertical), and mounting systems (roof-additive, -integrated, canopy, etc). Hence, the manufacturers offer a great variety of design possibilities. However, in regards to unavailable information about the thermal impact on the electrical power output and relevant building functions of BIPV products, the manufacturers consider these characteristics separately from the standard PV module and conventional building products, respectively. Therefore, the accuracy of the system and building design has not been able to be achieved yet.

The energy yields and power output of BIPV application have been investigated in comparison to conventional PV systems in order to describe the characteristics of BIPV mentioned above. With respect to the requirements of the Construction Production Directive [CPD-89/106-EEC], the technical barriers of 'mechanical resistance and stability' and 'energy economy and heat retention' have also been taken into account under the corresponding load bearing capacity and relevant thermal characteristics of building envelopes, respectively.

### 2.1 Electrical Aspect

The conventional PV system on a free-standing application has proven to provide a better performance compared to BIPV applications. With installation at the optimum tilt angle, the PV system receives maximum solar irradiation. Due to free thermal dissipation on the front- and backside of the PV module, a lower operating temperature can be achieved compared to BIPV applications, where the backside is normally closed due to the structure of the buildings. The simplest power output model can be used (2.1) to predict the power output ( $P_{elec}$ ) and energy yield ( $E_{elec}$ ) of PV systems. Inclined solar irradiation ( $G_T$ ), PV module efficiency at STC condition ( $\eta_{STC}$ ), PV temperature coefficient ( $\alpha_{PV}$ ), and operating temperature ( $T_C$ ) are the main parameters influencing the power output of PV systems.

$$\int P_{elec} dt = \int [\eta_{STC} \cdot (1 - \alpha_{PV}(T_C - T_{STC})) G_T] dt \quad 2.1$$

The power output and energy yield of conventional PV systems can be calculated using this simple model. The inclined solar irradiation can be obtained from the measurement either through a horizontal pyranometer or solar cell sensor together with inclined solar irradiation conversion models, or directly through a tilted

pyranometer or solar cell sensor. It can also be obtained from meteorological data services, e.g. meteonorm or other simulation software. With the pyranometer measurement, the reflection and spectrum losses are not taken into account, whereas they are considered in solar cell sensor measurements [Misara-2010b]. In the PV module standard EN-61215 and EN-61646 for corresponding crystalline and thin-film PV technologies, the PV module efficiency and PV temperature coefficient are measured under an STC condition: solar irradiation of  $1000\text{W/m}^2$ , ambient temperature of  $25^\circ\text{C}$  and Air Mass (AM) 1.5. This air mass value is the direct optical path length through the Earth's atmosphere, expressed as a ratio relative to the path length vertically upwards. However, operating temperature is an unpredictable parameter. It is influenced by various factors, such as multi-layered configurations, mounting systems, locations, etc. In order to achieve more predictable operating temperatures of PV modules, Nominal Operating Condition Temperature (NOCT) was introduced, which is measured under a solar irradiation of  $800\text{W/m}^2$ , wind speed  $1\text{ m/s}$  and AM 1.5.

### Limits of the Electrical Aspect

Compared to a conventional PV system, BIPV is mostly installed in flexible forms: at a non-optimum tilt angle with low ventilation, vertically integrated on the façade and horizontally integrated on the roof. Consequently, the operating temperature of a BIPV module at variable applications becomes higher and difficult to predict. Hence, the maximum performance could not be achieved for the generation of electrical energy. Moreover, the reflection and spectrum losses on PV modules increase with other module orientations and tilted angles.

The operating temperature of PV systems is the most critical parameter used when evaluating the energy yield and power output of BIPV application. It is directly coupled with the module's efficiency [Skoplaki-2009]. The operating temperature of BIPV modules is much higher compared to conventional PV systems due to the multi-layers of PV module configuration on its backside, which leads to poor ventilation and the corresponding lower thermal dissipation in its surroundings. Especially regarding the ventilation behind the PV in roof additive or integrated applications, there is still a lack of information to explain the operating temperature characteristics. Therefore, the NOCT temperature of standard PV modules is not really applicable for BIPV applications. Hence, with reference to these parameters, the electrical power output, and energy yield of BIPV is generally lower than that of standard PV modules. The time delay of the operating temperature and corresponding power output of BIPV-modules from solar irradiation occur due to the

heat capacity ( $C_M$ ) of the BIPV module with a higher multi-layered configuration from laminated glass to insulated glass, or the composite element with thermal insulation of the BIPV module compared to the standard PV module

In addition, PV module efficiency is not always constant. It is influenced by the weak-light characteristic of the PV module and shunt resistance [Grunow-2004]. The Energy Rating Standard [EN 61853-1] was introduced in order to describe PV module efficiency under the consideration of weak-light characteristics and operating temperature. Regarding spectrum and reflection loss compensation of PV modules, Friesen found that the use of the reference solar cell sensor instead of the pyranometer can reduce the uncertainty of the energy and power output prediction to +/- 5% [Friesen-2008]. However, these uncertainties were considered based on standard PV applications and not BIPV applications.

Regarding the market share and market growth of PV in the building sector, there are still many problems in terms of grid integration and self-consumption (grid-home-integration) of PV systems. These include the instability of low voltage grids due to numerous grid-connected PV systems as well as how to balance power producers and consumers locally. The energy yield is not the most relevant parameter of a PV system; the real-time power output fed into the grid or self-consumed in the household is also highly important [Ayompe-2010]. Therefore, the real-time power output prediction is necessary.

## 2.2 Thermal Aspect

In the Construction Product Directive, energy economy and heat retention are important aspects for all building products. Functioning as integrated elements in buildings, BIPV elements have to fulfil specific requirements: the newly modified European Energy Performance of Buildings Directive (EPBD), which states that all new buildings must be “nearly zero energy buildings” (NZE) by 2020; the German regulation for energy saving in building (EnEV), which states that buildings have to reduce their energy consumption and cover their own consumption. These energy economy and heat retention aspects of BIPV can be evaluated under the following functions: thermal insulation ( $U$ -value), solar heat gain in winter ( $g$ -value) and sun control in summer ( $F_c$ -value). Figure 2-1 describes the characteristics of the thermally relevant building functions.

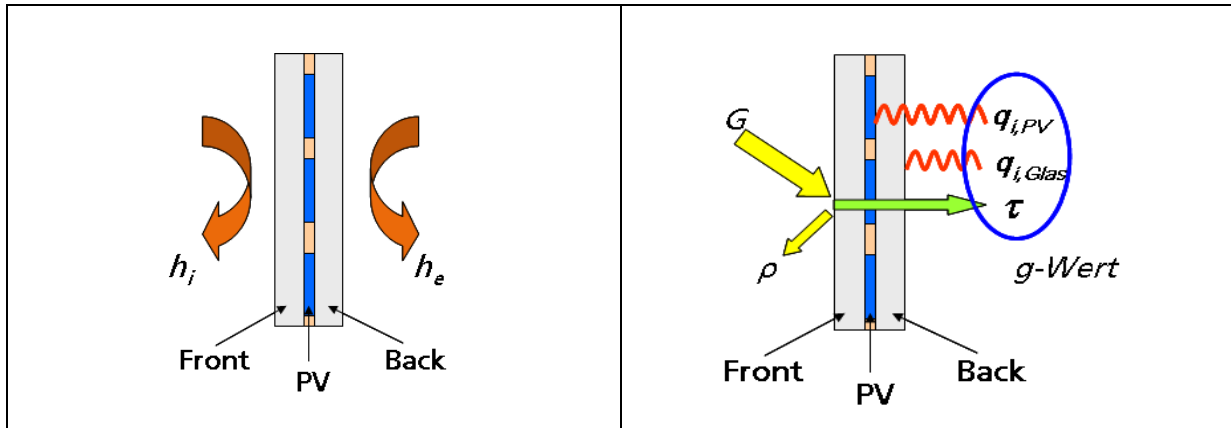


**Figure 2-1 Thermal parameters of building products: U- and g-values.**

The heat transmission coefficient (**U**-value) is a parameter of thermal insulation quality for building products, which means the amount of heat flow in Watt (W) transported through one square meter of building products at a temperature difference of 1 K. The **U**-value is composed of the heat transmission coefficients (**h<sub>t</sub>**) together with the internal and external heat transfer coefficient (**h<sub>i</sub>**, **h<sub>e</sub>**) (2.2) [EN 673]. The heat transmission coefficient (**h<sub>t</sub>**) composes heat transmission of each layer in solid material (**d/λ**) and in fluid material (**h<sub>s</sub>**); **d** and **λ** represent the thickness (m) and heat conductivity (W/mK) of each layer in solid material (2.3).

*Heat transmission coefficient (U-value)*

$$\frac{1}{U} = \frac{1}{h_e} + \frac{1}{h_t} + \frac{1}{h_i} \quad 2.2$$

$$\frac{1}{h_t} = \sum_1^N \frac{1}{h_{s,i}} + \sum_1^M \frac{d_i}{\lambda_i} \quad 2.3$$

In winter, the solar heat gain coefficient (**g**-value) is a parameter of total energy transmittance of transparent building products, e.g., glazing. This consists of the direct transmission of solar radiation (**τ<sub>e</sub>**) and the secondary heat dissipation toward the interior of the building (**q<sub>i</sub>**), which is the absorption part of the element (**α<sub>e</sub>**), dissipated toward the interior of the building (2.4, 2.5) [EN 410]. In summer, the solar reduction ratio (**Fc**-value) is a parameter of solar protection devices. It has a ratio of **g**-value of the solar protection device (**g<sub>PV</sub>**) to the **g**-value of glazing without shading elements (**g<sub>glass</sub>**) (2.6) [DIN 4108-2].

Solar heat gain coefficient (**g**-value)

$$g = \tau_e + q_i \quad 2.4$$

$$q_i = \alpha_e \cdot \frac{h_i}{h_i + h_e} \quad 2.5$$

Solar reduction ratio (**Fc**-value)

$$F_c = \frac{g_{PV}}{g_{glass}} \quad 2.6$$

### Limits of the Thermal Aspect

In regard to thermal relevant functions of BIPV modules, most BIPV manufacturers assume their products based on conventional building products. For instance, a PV-module with a laminated glass configuration has the same **U**-value of 5.5 W/m<sup>2</sup>K as standard laminated glass. Further, the **q<sub>i</sub>** in g-value depends on the percentage of PV-cell coverage together with the ratios of internal and external heat transfer coefficient of the conventional glazing.

Summer and winter conditions have not been taken into account during the identification of these functions by the manufacturers. The manufacturers consider their building functions based solely on the winter boundary condition (**h<sub>i</sub>** at 7.7 W/m<sup>2</sup>K and **h<sub>e</sub>** at 25.0 W/m<sup>2</sup>K) (EN 673). To identify the **U**-value and **g**-value, the winter boundary condition has to be considered, defined in EN 410. However, as a part of solar reduction ratio (**Fc**-value), the g-value has to be considered based on the summer boundary condition, defined in EN 13363-2.

The above conditions are applied only to glass, not to PV modules. As for the higher degree of absorption of solar cells in comparison to conventional glazing, the heat source occurs inside the BIPV-modules. This increases the operating and surface temperature of BIPV-modules. Therefore, the heat transfer coefficient (**h<sub>i</sub>**, **h<sub>e</sub>**) and the heat transmission coefficient in the cavity (**h<sub>s</sub>**) are varied compared to conventional glazing without internal heat sources. The relevant building functions are changed along with the deviation of these thermal parameters.

According to ISO 6946, the correlation of internal and external heat transfer coefficients (**h<sub>i</sub>**, **h<sub>e</sub>**) and the heat transmission coefficient (**h<sub>s</sub>**) has been defined under consideration of different operating temperatures. Regarding the winter and summer



boundary conditions above, the operating temperature and surface temperature differ based on an individual multi-layered configuration and different percentage of PV cell coverage. A certain operating temperature of each multi-layered configuration is not known. Therefore, this building code is not applicable for a variety of BIPV applications.

For the building planers and architects, there are no proper calculation methods for identifying these thermal parameters and corresponding relevant building functions of BIPV modules at present.

In this case, there are many measurements to identify these relevant building functions and corresponding thermal parameters, e.g. U-value by Hot-Box [EN 12567], Guarded Hot Plate [EN 674] and Heat Flow Meter methods and g-Value by Calorimetric [EN 410].

- U-value measurement: With respect to the boundary conditions above, however, the solar irradiation and corresponding internal heat source of PV-specific characteristic have not been considered for BIPV applications yet. For conventional building products, the heat flux only flows in one direction. In BIPV application with internal heat source, the heat flux will flow into both directions from the internal heat source to both ambient sides.
- g-value measurement: The total energy transmittance can be measured without knowing the internal and external heat transfer coefficients. As a result, the calculation method of thermally relevant building functions for the architects and building planners could not be achieved with the flexibility of BIPV modules in terms of percentage of PV cell coverage and multi-layered configuration. Moreover, the heat flux plate could not work properly under direct solar irradiation due to its sensitivity to direct solar irradiation. To examine the **g**-value of a PV module, the measurement takes around 1 day for the calorimetric testing equipment to reach its steady state condition. Due to this long testing period, the operation costs of a solar simulator are relatively high.

### **2.3 Mechanical Aspect:**

The mechanical characteristic is one of the most important characteristics to describe the failure modes of BIPV modules in terms of both the electrical and mechanical failures, e.g. glass fracture, weather resistance, cell cracks, etc.

BIPV modules are typically fabricated during the laminating process with 2 glass panes and described as laminated glass [VDE-0126-21]. Laminated glass consists of at least two panes and one interlayer, whereby the panes are bonded to the interlayer in the manufacturing process. The mechanical behaviour of laminated glass depends on the glass material as well as the bonding properties of the interlayer. The following figure shows the different bonding stages of laminated glass.

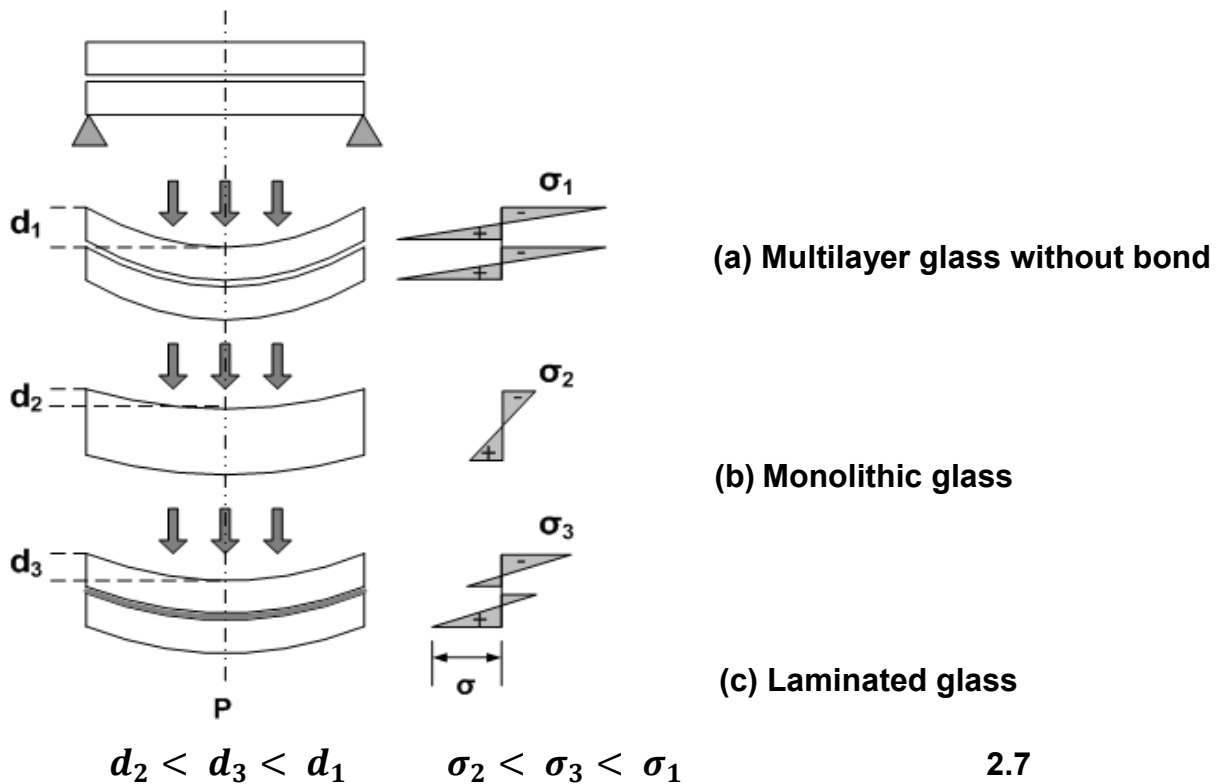


**Figure 2-2 Deflection behavior and stress distribution of (a) multilayer glasses without bond, (b) monolithic glass and (c) laminated glass [Wellershoff-2007].**

- Multilayer glass (without bond) - When two or more panes are laid loosely on top of each other without any interlayer bonded in between the individual panes, the loads are then split in proportion to its bending strength.
- Monolithic glass (Rigidly bonded) - Monolithic glass is a glass panel comprised of a single sheet of float glass. The glass can be tinted, coated, and otherwise processed but it is used as a single sheet.
- Laminated glass (with bond) - In the case of two layers of glass panes bonded with a shear-resistant interlayer, the load can no longer be split in proportion to its bending strengths. It has to be considered as a composite unit.

The mechanical behaviors of laminated glass can be described in terms of bending stress ( $\sigma$ ) and deflection ( $d$ ). The negative and positive sign of the bending stress represent the compressive and tensile stresses on the front and back glasses, respectively.

Figure 2-2 describes the mechanical properties of laminated glass under different bonding states of interlayers. The lower limit is the so-called *layered limit*, where the glass panes react without shear bond (a). The upper limit is the *monolithic limit*, where all glass panes are rigidly connected (b). The mechanical behaviors (bending stress and deflection) of laminated glass are between these upper and lower limits (c), (2.7) [Schittich-2007].

### Limits of Mechanical Aspect

With respect to the higher operating temperature of the BIPV module, the mechanical behavior changes compared to conventional laminated glass. As for the mechanical behaviors of the glass material, the changes are not significant.

However, the bonding properties of the interlayer mainly depend on the operating temperature of the BIPV module. Furthermore, the load duration is also another parameter effecting the bonding properties and corresponding mechanical behaviors of BIPV-module. Therefore, the interlayer material plays a major role in the mechanical behaviors of BIPV-laminated glass.

Polyvinyl Butyral (PVB) is widely used in glass lamination. Thanks to its long existence in the glass industry, PVB is mainly used in safety laminated glass. This is also due to its special properties, like resistance to physical attack and its residual load bearing capacity. For building regulations, a laminated glass with PVB-interlayer is accepted as laminated safety glass in a regulated building product list.

In the PV industry, alternative interlayer materials, such as ethylene-vinyl acetate (EVA) or polyethylene (PE) with improved temperature stability, are used. Other special applications are realized by using thermoplastic polyurethanes (TPU) as an interlayer. These interlayer materials differ in their chemical compositions, which lead to different bonding characteristics.

For the static calculation, the external mechanical load of wind and snow are taken into account, as defined in EN-1991. According to German building regulations, the bonding characteristic of the interlayer is not allowed for the static calculation of the laminated glass and laminated safety glass due to the poor bonding characteristic of

PVB-interlayer at long load duration (high creep rate). Therefore, for the laminated glass configuration, the two glass panes without bonding will be considered, as described in Figure 2-2 a.

The mechanical behaviour of laminated glass are documented solely at room temperature. As for the higher absorption rate of BIPV modules and corresponding higher operating temperature, the mechanical behaviors of laminated glass and its interlayer will change. The operating temperature of BIPV modules are varied based on solar irradiation, ambient temperature, etc., which are facing with different external mechanical loads (wind and snow loads) and load durations on the BIPV modules.

To examine the mechanical behaviour of PV laminated glass with higher operating temperature and long testing period, a climate chamber has been employed. With respect to the variable dimension of PV modules, a large climate chamber is needed. Due to the long testing period of 24 or 48 hours, the operating cost of a climate chamber becomes higher. Consequently, the tests are cost intensive.

Up to now, there have been neither common regulations nor relevant building codes for calculating the mechanical behaviors of laminated glass together with its bonding properties under consideration of operating temperature and load duration along with the corresponding magnitude of external mechanical loads. In addition, each country has its own set of national regulations and standards, making it difficult for the PV-module manufacturers to identify a format that best suits widely accepted building codes.

Instead of a PVB interlayer, alternative interlayer materials have been used in the PV industry. These include EVA, PE, TPU, etc. Even though these interlayers demonstrate better mechanical behaviors (better elasticity at high operating temperature and lower creep rate), these interlayers are not accepted as laminated safety glass in regulated building products due to a lack of experience with their characteristics. These alternative interlayers are quite new for building product industries.

## **2.4 Objective**

With respect to the higher operating temperature of the BIPV module, the investigation of the thermal impact on electrical, thermal and mechanical characteristics is the main objective of this work. Firstly, the temperature model with power balance concept has been developed based on the dynamic and steady state

under the consideration of the different configuration and installation possibilities of the module. With this temperature model, the electrical characteristics can be described together with thermal characteristics of BIPV modules. With respect to the dynamic simulation, the real-time power output and energy yield can be achieved together with a real-time building simulation: surface temperature, energy consumption, etc. For steady state simulation, the relevant building functions of BIPV modules can be obtained during summer and winter periods.

In order to fulfil the requirements of building regulations, the model for mechanical characteristics was developed based on different thermal and mechanically induced load scenarios together with a variation of load duration, mounting system, and encapsulation materials.

To validate the temperature model together with the mechanical model, the different configurations of the test equipment were developed using new test methods. By means of the test equipment, the PV variable mounting system and mechanical testing equipment, different mounting systems, multi-layered configurations, and mechanical loads could be emulated. For the new test method, the back-bias current concept, solar irradiation and certain operating temperatures could be obtained by feeding the current back into the PV modules in order to provide measurements close to the reality of BIPV modules.

With the above-mentioned validated models, electrical, thermal and mechanical behaviour were further evaluated based on other configurations. Finally, these model developments were implemented in the software tools used directly by PV manufacturers.

### 3. Temperature Model

The main difference between BIPV modules and conventional building products is the higher operating temperature due to PV-cell characteristics. The temperature of PV-cells is one of the most important parameters used for the performance of PV-systems: electrical, thermal, and mechanical performances. The cell temperature depends on several parameters, such as the thermal properties of the materials used, type of cells, multi-layered configuration, installation methods, and local climate conditions. With respect to the variation of BIPV applications, multi-layered configurations, installation possibilities, and environmental conditions, simulation modeling is necessary to describe their characteristics. Therefore, the temperature model was the first to be developed. This model had to simulate the operating temperature as well as surface temperature of BIPV modules. With a higher operating temperature and corresponding surface temperatures, the electrical, thermal, and mechanical models will be further developed.

In a nutshell, a study of the literature expressing the operating temperature of a PV cell ( $T_c$ ) as a function of pertinent weather variables and irradiation yield can be explained with a large number of implicit and explicit models, [Skoplaki-2009].

#### 3.1 State of the Art Temperature Models

##### 3.1.1 NOCT-Model

The nominal operating cell temperature ( $T_{NOCT}$ ) is commonly used to estimate the cell temperature ( $T_c$ ) of BIPV modules (3.1). This  $T_{NOCT}$  is defined as the average temperature of PV modules for free-standing outdoor applications under Standard Operating Conditions – SOC (solar radiation - 800 W/m<sup>2</sup>, ambient temperature ( $T_{amb}$ ) - 20°C, tilt angle - 45°, wind speed - 1m/s and open circuit operation) [EN 61215]. Generally, the NOCT value is an inherent property of each individual module, but its value can still vary from one module to another.

$$T_{NOCT} = (T_c - T_{amb})_{SOC} + 20^{\circ}C \quad 3.1$$

Therefore, the simplest correlation model for real-time operating cell temperature ( $T_c$ ) can be calculated with the function of solar irradiation ( $G_T$ ) (3.2) [Nolay-1987].

$$T_c = T_{amb} + (T_{NOCT} - 20^{\circ}C) \cdot \frac{G_T}{800 \text{ W/m}^2} \quad 3.2$$

INOCT (Installed Nominal Operating Cell Temperature) and NOST (Nominal Operating Specific Temperature) are also other possibilities to achieve a better operating temperature in BIPV applications. INOCT is defined as the PV cell temperature of an installed array under the NOCT conditions. It characterizes the thermal properties of the module and its mounting configuration [Fuentes-1987]. NOST is defined as a site and mounting specific module temperature at NOCT conditions [Kenny-2003].

Cell temperature and back-surface module temperature ( $T_M$ ) can be distinctly different. Knaup tried to estimate the precise operating cell temperature using backside surface temperature and the amount of solar irradiation for glass-glass and glass-backsheet modules (3.3), while Kings added up the temperature difference between the back-surface module temperature and ambient temperature [Knaup-1997, King-1997a]. The temperature difference is typically 2 to 3 °C for flat-plate modules in open rack-mounted PV systems for glass-glass and glass-backsheet, respectively. This difference is nearly zero for a thermally isolated back surface.

$$T_c = T_M + \frac{G_T}{1000} \cdot (T_M - T_{amb}) \quad 3.3$$

From the mathematical point of view, the correlations for the PV operating temperature can be explained either through explicit or implicit models. In implicit models, the operating temperature can be directly calculated from some parameters related to historic measured data, while it can be calculated by involving variables related to physical characteristics of PV-module itself, environmental conditions, etc.

### 3.1.2 Explicit Methods

Sauer model: It is the simplest explicit model to explain the operating temperature (3.4). This model considers only the linear correlation between operating temperature and solar irradiation, without any consideration of the influence of wind.

$$T_M = T_{amb} + a + b \cdot G_T \quad 3.4$$

The parameters  $a$  and  $b$  can be achieved by measurement from individual location. They are dependent on mounting system and regional wind characteristics. Table 3-1 shows the parameter  $b$  based on location Germany [Sauer-1994].

Mounting type	$b (^{\circ}\text{C} \cdot \text{m}^2/\text{W})$
Facade-integrated, poor ventilation	0.055
Limited ventilation, large surface	0.035
Roof-integrated, large surface	0.025
Freestanding	0.015

**Table 3-1 Parameter  $b$  in Sauer model based on Germany locations**

Simulation program: It explains the operating temperature quite similar to the Sauer Model. In the simulation software, the parameter  $a$  is neglected. Table 3-2 shows the parameter  $k$  from the simulation program PV-SOL and SolEm, respectively (3.5) [PV-SOL -2000, Fischer-2007].

$$T_M = T_{amb} + k \cdot \frac{G_T}{1000 \text{ W/m}^2} \quad 3.5$$

Mounting types	$k (^{\circ}\text{C})$	Mounting types	$k (^{\circ}\text{C})$
Free standing	20	Free standing	20
On-roof with ventilation	30	On-roof, high ventilation gap	27
Roof- or Facade-integrated, no ventilation	45	On-roof, low ventilation gap	36
		Roof -integrated, no ventilation	53

(a) (b)

**Table 3-2 Parameter  $k$  for PV-SOL Software (a) and SolEm (b)**

Sandia-SNL-model: It was developed in the 1980s and is the simplest explicit equation to describe the operating temperature as a function of ambient temperature, solar irradiation together with parameter  $k$  (3.6). This parameter was collected from historic measurement data in the Sandia National Laboratory (SNL) in USA (Table 3-3) [Ross RG-1976, Nordmann-2003].

$$T_M = T_{amb} + k \cdot G_T \quad 3.6$$

This model has proven to be applicable to the well ventilated PV-System with the accuracy of  $\pm 5^{\circ}\text{C}$ . For BIPV, the temperature differences can reach up to  $20^{\circ}\text{C}$ . Moreover, it is not easily adaptable to site dependent influences. Therefore, a new empirically-based thermal model was developed by utilizing further measurements over several different days under near linear equilibrium conditions (nominally clear sky conditions without temperature transients due to intermittent cloud cover). This model was successfully applied on a free-standing and roof-integrated system with an accuracy of  $\pm 5^{\circ}\text{C}$  or  $\pm 3\%$  of power output, respectively. This model



incorporates parameters affecting the PV module's temperature, such as wind speeds and configuration of the installations (3.7). However, the incorporating effect of wind direction is believed to be unnecessarily complex.

PV array type	$k$ ( $^{\circ}\text{C}\cdot\text{m}^2/\text{W}$ )
Well cooled	0.0200
Free standing	0.0208
Flat roof	0.0260
Not so well cooled	0.0342
Transparent PV	0.0455
Facade-integrated	0.0538
On sloped roof	0.0563

**Table 3-3 Parameter k for Sandia-SNL-Model**

$$T_{M,b} = G_T \cdot \{e^{a+b \cdot v}\} + T_{amb} \quad 3.7$$

Where  $T_{M,b}$  is backside surface temperature ( $^{\circ}\text{C}$ ),  $G_T$  is the solar irradiance on surface ( $\text{W}/\text{m}^2$ ) and  $v$  is wind speed measured at standard 10-m height ( $\text{m}/\text{s}$ ).

Module Type	Mounting	a	b	$\Delta T$
glass/cell/glass	open rack	-3.47	-.0594	3
glass/cell/glass	roof mount	-2.98	-.0471	1
glass/cell/glass	Isolated	TBD	TBD	
glass/cell/Tedlar	open rack	-3.56	-.0750	3
glass/cell/Tedlar	roof mount	TBD	TBD	
glass/cell/Tedlar	Isolated	-2.81	-.0455	1
PV-concentrator	tracker	-3.23	-.130	13

**Table 3-4 Parameters a and b for empirically-based thermal SNL Model and temperature difference between cell and backside surface temperature ( $\Delta T$ )**

Table 3-4 provides the empirically determined coefficients of different module types and mounting configurations for the empirically-based thermal SNL Model along with temperature differences between cell and backside surface temperature [King-2003].

Trinuluk tried to compare the SNL-Model and NOCT-model. She figured out that the SNL model has more accurate results than the NOCT model. The error of the SNL model is only half of the NOCT-model [Trinuluk-2009]. However, in order to get the

precise operating temperature, the parameters  $a$ ,  $b$  and  $\Delta T$  have to be re-adjusted at certain locations.

EN 61853-2: The operating temperature is assumed to be a function of the ambient temperature ( $T_{amb}$ ), the wind speed ( $v$ ) and the solar irradiance on the inclined solar module ( $G_T$ ). With the plotting ( $T_M - T_{amb}$ ) against  $G_T$  for various wind speeds, the module temperature can be estimated (3.8). Table 3-5 gives a sample of coefficients  $a$ ,  $b$  under variable wind speed for glass-backsheet module with aluminium frame.

$$T_M - T_{amb} = b_i \cdot G_T + a_i \quad 3.8$$

Wind speed	$a_i$	$b_i$
< 1 m/s	-2	0.0310
1 m/s ... < 2 m/s	-2	0.0275
2 m/s ... < 3 m/s	-2	0.0210
3 m/s ... < 5 m/s	-2	0.0175
5 m/s ... < 7 m/s	-2	0.0120
> 7m/s	-2	0.0105

**Table 3-5 Example for variation of parameters  $a_i$  and  $b_i$  versus wind speed**

### 3.1.3 Implicit Methods

The thermal environment which establishes the instantaneous value of the PV module's operating temperature is quite complex. Apart from the electrical power production of PV, the non-converted heat power has to be taken into account in the relevant power balance of the modules together with heat dissipation mechanisms: conduction, convection, and radiation, which leads to the estimation of a different operating temperature ( $T_c$ ).

The simplest power balance model could be described by 3.9 – 3.11, where  $\tau$  the transmission coefficient of front glass (%),  $\alpha$  the absorption coefficient of PV-Cell (%),  $\eta_c$  the cell efficiency (%),  $\alpha_{coeff}$  the temperature coefficient of PV cells (%/K),  $U_{PV}$  the total thermal transmission coefficient of BIPV element (W/m<sup>2</sup>K). The model assumes that both sides of the module have the same ambient temperature and the total thermal dissipation coefficient is constant.

$$(\tau\alpha)G_T = \eta_c \cdot G_T + U_{PV}(T_c - T_{amb}) \quad 3.9$$

$$\eta_c = \eta_{STC} \cdot [1 - \alpha_{PV}(T_c - T_{STC})] \quad 3.10$$

$$T_c = \frac{U_{PV} \cdot T_{amb} + G_T [(\tau\alpha) - \eta_{STC} - (\alpha_{PV} \cdot \eta_{STC} \cdot T_{STC})]}{U_{PV} - (\alpha_{PV} \cdot \eta_{STC} \cdot G_T)} \quad 3.11$$

Mattei et. al have combined the use of temperature dependent PV cell efficiency (3.11) into this power balance. He found that the value of  $U_{PV}$  of 28.8 W/m<sup>2</sup>K is in good agreement with the measurement [Matteil-2006]. However, Misara found out that total  $U_{PV}$  on the front and backside of 31.5 W/m<sup>2</sup>K, 32.7 W/m<sup>2</sup>K and 19.14 W/m<sup>2</sup>K show a good agreement of operating temperature with a glass-backsheet, glass-glass and glass-glass-insulation PV modules, respectively [Misara-2010a].

Duffie tried to combine the simplest power balance model together with the model under NOCT-conditions by replacing the  $\eta_{STC}$  with zero (open circuit) (3.12) [Duffie-2006].

$$T_c = T_{amb} + \left( \frac{G_T}{G_{NOCT}} \right) \cdot \left( \frac{U_{PV,NOCT}}{U_{PV}} \right) \cdot (T_{NOCT} - T_{amb,NOCT}) \cdot \left[ 1 - \left( \frac{\eta}{\tau\alpha} \right) \right] \quad 3.12$$

There is still much research trying to precisely describe the module temperature with explicit and implicit methods [Skoplaki-2009].

### 3.2 Deficits on BIPV application

In the NOCT model, the operating cell temperature ( $T_c$ ) is linearly proportional to solar irradiation (3.2). However, Stultz detected that the operating cell temperature ( $T_c$ ) is linearly proportional to the solar irradiation above 400 W/m<sup>2</sup> [Stultz-1978]. In addition, the heat loss coefficient to the surroundings was not considered in this model. Moreover, it was done in free-standing conditions, where both sides of the module face the same environmental conditions; whereas in BIPV applications, they face different environmental conditions, such as different wind speed, ambient temperature, and multi-layered configurations.

With regard to the different multi-layered configuration, material used, tilt angle, dimension, etc., they lead to variable heat conduction and corresponding surface temperature. This different surface temperature leads to different power dissipation in terms of convection and radiation heat transfer. The simulated operating temperature

can be predicted as much as 20K by using the NOCT model in BIPV applications [Davis-2001].

Although INOCT and NOST are defined under NOCT conditions when mounting a specific array and at a specific site, these are not appropriate for BIPV applications due to the variable environmental conditions, e.g. wind and ambient temperature, and multi-layered configurations.

As a result of the wide range of ambient temperature, different multi-layered configuration on the front and backside of BIPV module and related inconstant heat transfer coefficient, the explicit and implicit models would not be appropriate for BIPV applications.

Even the error of the SNL-Model is only half compared to the NOCT-Model; however, the different coefficients could be found at different locations for better modelling [Trinuluk-2009]. This explicit model is applicable only at certain locations where the parameters were calculated from a measurement.

For different multi-layered configurations of BIPV modules, such as PV-laminated glass, PV-insulated glass and composite elements with a metal sheet, a flexible interlayer, etc., the coefficient was adapted individually to a certain BIPV multi-layered configuration and its mounting systems. There are no a specific coefficients for a BIPV module with different module multi-layered configurations, mounting systems, and locations.

These explicit methods are quite easy and fast to estimate the operating temperature of PV. However, the accuracy will vary at different locations, module multi-layered configurations, and in mounting systems.

For implicit models, the heat transfer coefficient ( $U_{PV}$ ) is not always constant. It is constantly changing due variable wind speed, surface and ambient temperatures, etc. Moreover, the module size, loading and solar spectrum show other effects on this operating Temperature [Bharti-2009]. Therefore, the real-time  $U_{PV}$  is needed for both the front and backside of BIPV modules.

These implicit methods are appropriate only for standard PV-laminated glass, where the difference between cell and surface temperature is max 2-3 °C. With a high multi-layered configuration of a BIPV module from a laminated glass to a composite element with thermal insulation, the temperature difference is higher than the

standard PV laminated glass. The surface temperature, which directly affects the amount of thermal dissipation, is dependent on the multi-layered configuration or conduction heat transfer of material used, respectively.

Under steady-state conditions for all methods mentioned above, the thermal capacity of the modules has not been taken into account. For the standard PV-laminated glass, the thermal capacity has been assumed to be low and can be neglected. Regarding higher multi-layered configurations and the corresponding higher thermal capacity of the BIPV module, a time-delay between operating temperature and solar irradiation occurs. Jones showed the time-lag between the operating temperature and fluctuated solar irradiance of the standard PV laminated glass module on a cloudy day, which is more than 15 minutes [Jones-2001]. Therefore, a shorter time resolution is needed under consideration of thermal capacity of PV-Modules. By using hourly average values, some dynamic effects could not be observed. This effect is mainly needed for the sizing of system components in real-time for grid- and home-integration applications.

With respect to a non-optimal tilt angle and orientation in BIPV application, the angle of solar incident ( $\theta_{in}$ ) and spectral response (**SR**) have to be taken into account in the model in order to evaluate the spectrum and reflection loss of the PV modules. Up to now, they have been considered separately from the models above. In order to increase the accuracy of the prediction, these approaches have to be taken into account together.

In BIPV applications, the ventilation behind the BIPV module is one of the critical parameters that directly affects the operating temperature and corresponding real-time power output of BIPV modules. Up to now, there has been some research on this topic. However, the holistic approach of all the above-mentioned aspects has yet to be taken into account.

The methods described above can only measure the operating temperature and corresponding electrical characteristics. However, the thermal characteristics are also important for BIPV applications. To identify the relevant thermal characteristics on building functions, the surface temperature is needed - and not the operating temperature. Especially for BIPV module with a high multi-layered configuration, the surface temperature will be completely different to the standard PV module.

### 3.3 Real-Time Power Balance Model

In order to evaluate all relevant aspects in BIPV applications, therefore, the real-time power balance model has been developed using a holistic approach (operating temperature and corresponding electrical power output as well as thermal behaviour of BIPV modules).

This power balance is based on the concept of total power input and power output of the BIPV module (Figure 3-1). The power input is the solar irradiation radiated on the PV cell, whereby most of the energy intensity is under a short wavelength range (200-2500 nm). One part of this power input is transmitted through the module (in the case of the transparent module), while another part is reflected off of the surface and the rest will be absorbed in modules. This short wavelength absorbed inside the module will be converted into electrical power through PV cell and thermal power, where most of the energy intensity is under a long wavelength range. In a dynamic state, the rest long wavelength thermal power can be inferred in 2 parts: thermal dissipation power and thermal absorption power. This thermal dissipation power will be dissipated through heat conduction, - convection and –radiation. The amount of thermal dissipation power is related to surface temperature.

The thermal absorption part is directly related to its multi-layered configuration and corresponding thermal capacity. It leads to a time-lag of operating temperature under fluctuated solar irradiance on a cloudy day. This time-lag could be more than 15 minutes for standard PV modules [Jones-2001]. This is very important for energy management application and building simulation. The thermal absorption power will increase the module temperature until it reaches the steady state. In order to solve the dynamic temperature model, the iteration method (Euler-Method) has been implemented. Nevertheless, this increasing module temperature will react to the amount of electrical, dissipation and absorption power [Misara-2010a]. To evaluate the thermal relevant building functions, the steady state is considered. Under steady state, the operating becomes constant. It can be determined that the rest of the long wavelength thermal power will be completely converted into dissipation power when the thermal absorption power is no longer available.

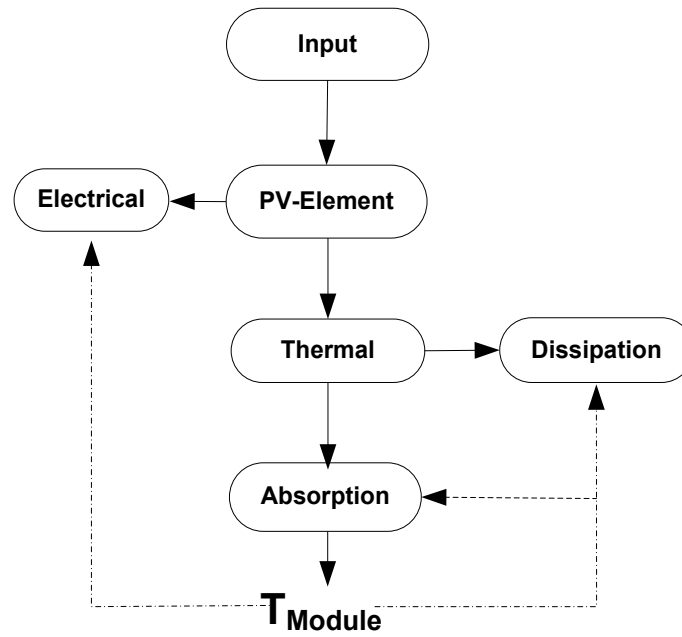


**Figure 3-1 Real-Time Power Balance Model concept**

### 3.3.1 Input Power

Since the solar irradiation was considered as the power input of the PV-system, the global solar irradiation was defined at  $1000 \text{ W/m}^2$  at an operating temperature of  $25^\circ\text{C}$  together with spectrum of corresponding AM1.5 under Standard Test Condition (STC). With respect to non-optimal orientation and higher multi-layered configuration, especially in BIPV applications, these circumstances could seldom be achieved. Regarding solar irradiation, a major proportion of the yearly solar irradiation on BIPV applications is in the weak light range, defined in EN50524 [Burger-2009]. With solar irradiation in a weak light range, the amount of solar irradiation is not the only main parameter for the power input of PV system. In order to evaluate the power input on PV cells under a weak light range, other relevant parameters have to be taken into account, e.g. the angle of incident ( $\theta_{in}$ ), Air Mass ( $AM$ ), etc.

#### 3.3.1.1 Angle of Incident ( $\theta_{in}$ ) and Air Mass ( $AM$ )

The optical properties, especially regarding reflection and spectrum losses, are also one of the critical parameters for evaluating the power input on a solar cell. These optical properties mainly depend on the angle of incident ( $\theta_{in}$ ) and zenith angle ( $\theta_z$ ), which affects the reflection loss and spectrum distribution of the solar irradiation, respectively. Figure 3-2 exhibits the correlation of each angle on the PV module, where  $n$  is the normal vector from the PV panel.

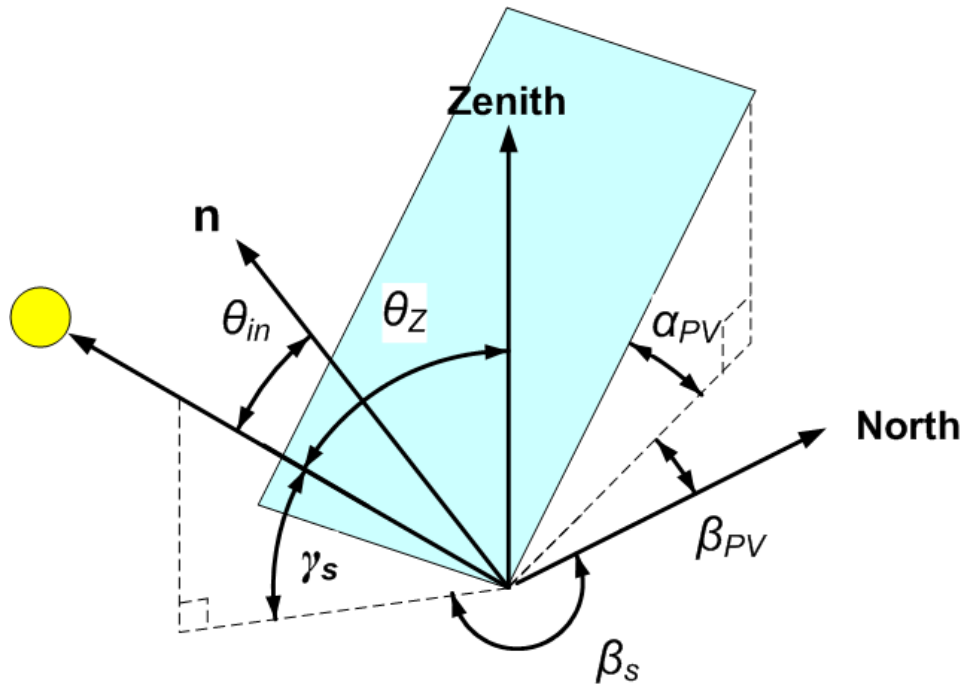


**Figure 3-2 Correlation of zenith angle ( $\theta_z$ ), angle of incident ( $\theta_{in}$ ), PV module tilt angle ( $\alpha_{PV}$ ) and PV module azimuth angle ( $\beta_{PV}$ ).**

In order to evaluate the real-time angle of incident ( $\theta_{in}$ ) and zenith angle ( $\theta_z$ ), the other relevant angles, i.e. solar altitude angle ( $\gamma_s$ ), solar azimuth angle ( $\beta_s$ ), PV tilted angle ( $\alpha_{PV}$ ), PV azimuth angle ( $\beta_{PV}$ ), declination angle ( $\delta$ ), hour angles ( $\omega$ ), time in hour ( $T$ ), and location latitude, ( $\phi$ ) have to be considered (Table 3-6).

In the BIPV application, the angles of incident change at different orientations, while the zenith angles are always constant for all orientations for a certain period of time.



Zenith Angle ( $\theta_z$ ) and Air Mass ( $AM$ )
$\delta = 23.45 \cdot \sin \left[ \frac{2\pi(284 + n)}{365} \right]$ $n = [30.3 \cdot (\text{month} - 1)] + \text{day}$ <p>(n = day of the year with Jan,1 as day 1 )</p> $\omega = \left[ \frac{12 - T}{24} \right] \cdot 360^\circ$ $\gamma_s = \sin^{-1}(\cos \omega \cdot \cos \Phi \cdot \cos \delta + \sin \Phi \cdot \sin \delta)$ $\theta_z = 90^\circ - \gamma_s$ $AM(x) = \frac{1}{\cos \theta_z}$
Angle of Incident ( $\theta_{in}$ )
$\theta_{in} = \cos^{-1}[-\cos \gamma_s \cdot \sin \alpha_{PV} \cdot \cos(\beta_s - \beta_{PV}) + \sin \gamma_s \cdot \cos \alpha_{PV}]$

**Table 3-6 Calculation of zenith angles ( $\theta_z$ ), Air Mass ( $AM$ ) and angle of incident ( $\theta_{in}$ ) [Duffie-2006].**

### 3.3.1.2 Spectrum Distribution

The spectrum distribution of direct solar irradiation is strongly influenced by Air Mass ( $AM$ ) values [Faine-2009] (Figure 3-3). The visible wavelength is in the range from 370nm – 750nm. At low  $AM$  during the day, the spectral irradiance in visible wavelength is higher compared to that in invisible wavelength, where the color of the sky becomes bluish. At high  $AM$  during sunrise and sunset, the spectral irradiance becomes lower in visible wavelength range compared to that in invisible wavelength, where the color of the sky becomes reddish. This deviation of direct spectrum distribution at a certain wavelength is influenced by the absorption and Rayleigh scattering of molecules in the atmosphere together with Mie scattering dust and pollutants in the air [DGS-2008].

In terms of diffuse irradiation, Figure 3-4 shows the spectral distribution of direct irradiation ( $G_{b,i}$ ) and diffuse irradiation ( $G_{d,i}$ ) on different Air Mass values [King-

1997b]. King concluded that the spectral distribution of  $G_{b,i}$  changes significantly, whereas the spectral distribution of  $G_{d,i}$  likely remains the same over different AMs. Blackburn described the correlation of a  $G_{b,i}$  during a clear sky day and a cloudy day together with a  $G_{d,i}$  during a clear sky day over different zenith angles or corresponding AM values. It can be concluded that the responsivities of  $G_{b,i}$  for clear and cloudy period GHIs are quite similar, while responsivities of  $G_{d,i}$  for a clear day DHI are quite low with a slight increase at higher zenith angles due to the Rayleigh scattering in the atmosphere, which causes shorter wavelengths to dominate the diffuse component [Blackburn-2012].

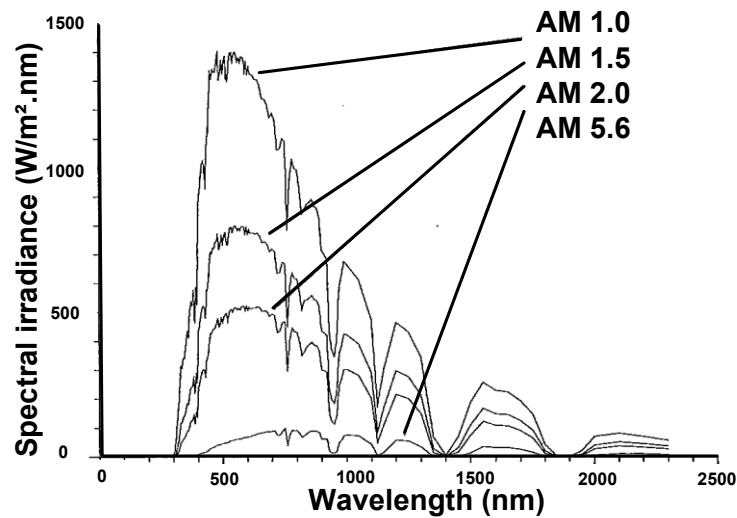


**Figure 3-3 Direct spectrum distribution at different AMs [Faine-2009]**

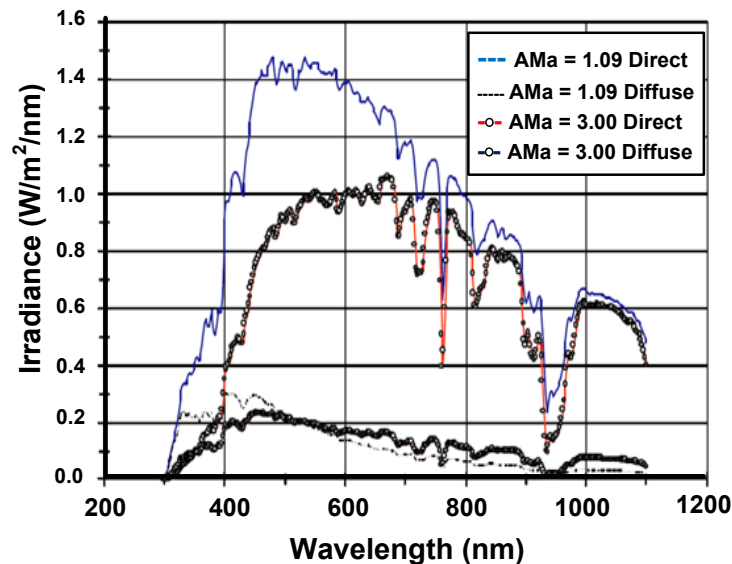


**Figure 3-4 Direct and diffuse solar spectral irradiance at different air mass [King-1997b]**

The influences of a different spectrum distribution at different AMs on PV technologies will be described in chapter 3.3.2.

### 3.3.1.3 Reflection Loss

In the case of reflection loss, the direct and diffuse irradiances need to be considered separately. The reflection loss of direct irradiation is affected directly by angle of incident ( $\theta_{in}$ ) and refraction indices ( $n$ ) of material used, while the reflection loss of diffuse irradiation is affected by the state of polarization [Krauter-1996, Yamada-2001]. Krauter worked explicitly on the reflection loss on different angles of incident and different refraction indices of 3-layer material of standard PV modules (glass, EVA and TiO) under consideration of a one day evaluation period over a year. The total reflection losses of each day are 15.5% of the incoming global radiation for an adequate module elevation angle. At high PV tilted angles ( $50^\circ - 90^\circ$ ), the reflection losses increase up to 42.5% for direct radiation [Krauter-1996]. The polarization of diffuse irradiation has an effect of 0.5-5% on total irradiation.

Moreover, the spectrum distribution is one of the other parameters affected by reflection loss. The characteristics of reflection loss are also influenced by each wavelength of solar irradiation. In the case of dispersion of spectrum distribution, the irradiation at a wavelength of 800 nm could represent all other wavelengths [Koomen-1996]. However, the transmittance is hardly influenced by the dispersion of spectrum distribution (around 1%). For a PV module with anti-reflection coating, however, the reflection loss can be reduced to 10%.

In EN 61853-2, the measuring procedures are described for the angle of incident (AOI); the module temperature versus wind speed and spectrum respond together with relative light transmission [EN 61853-2].

For the solar irradiation measurement, the reflection and spectrum losses have already been included in the solar cell irradiation sensor measurement but not in the pyranometer measurement.

### 3.3.1.4 Solar Irradiation on an Inclined Surface

For many solar energy applications, it is necessary to know the incident solar irradiance on an inclined surface. Usually, there are no measurements available for the surface of interest. Therefore, the irradiance on the inclined surface must be calculated from the horizontal global and diffuse irradiance measurements, which are readily available from many weather stations around the world. The calculation of the beam irradiance on an inclined surface is quite straightforward, given the position of the sun and the orientation of the surface.

The solar irradiation on an inclined surface  $G_i$ , is the sum of the direct  $G_{b,i}$  diffuse  $G_{d,i}$  and reflected irradiation  $G_{r,i}$  on the inclined surface (3.13). Most procedures used for measuring the performance of the photovoltaic modules are not concerned with the distinction between direct beam, ground reflected and diffuse components.

$$G_i = G_{b,i} + G_{d,i} + G_{r,i} \quad 3.13$$

Direct irradiation - the direct irradiance on an inclined surface  $G_{b,i}$  can be calculated (3.14), where  $G_b$  is the horizontal beam irradiance and  $R_b$  is the geometric factor ( $R_b > 0$ ).

$$G_{b,i} = G_b \cdot (\cos \theta_{in} / \sin \alpha_{PV}) = G_b \cdot R_b \quad 3.14$$

Diffuse irradiation - the diffused part of the irradiance on an inclined  $G_{d,i}$  is calculated with one of the following irradiance models (Table 3-7), where  $G_0$  is the extraterrestrial irradiance ( $G_0 = 1367 \text{ W/m}^2$ ). The differences among models will be evaluated in chapter 6.1.1.

<b>Jordan Model</b> $G_{d,i} = 0.5 \cdot G_d \cdot (1 + \cos \alpha_{PV})$
<b>Klucher Model</b> $G_{d,i} = 0.5 \cdot G_d \cdot [1 + F \cdot \cos^2 \theta_{in} \cdot \cos^3 \alpha_{PV}] \cdot [(1 + F \cdot \sin^3(\alpha_{PV}/2)) \cdot (1 + \cos \alpha_{PV})]$ $F = 1 - (G_b/G)^2$
<b>Hay Model</b> $G_{d,i} = G_d \cdot [0.5 \cdot (1 - A_1) \cdot (1 + \cos \alpha_{PV}) + (A_1 R_b)]$ $A_1 = G_b/G_0$
<b>Reindl Model</b> $G_{d,i} = G_d \cdot [0.5 \cdot (1 - A_1) \cdot (1 + f \cdot \sin^3(\alpha_{PV}/2)) \cdot (1 + \cos \alpha_{PV}) + (A_1 R_b)]$ $f = G_b/G$

**Table 3-7 Diffuse irradiation models on inclined surface; Jordan, Klucher, Hay and Reindl Models [Jordan-1963], [Klucher-1979], [Hay-1979], [Reindl-1990]**

Ground reflected irradiation - the ground reflected irradiance on an inclined surface  $G_{r,i}$  can be calculated (3.15), where  $G$  is the global irradiation and  $\rho_g$  is the average reflectance of the ground, so called Albedo. These Albedo values are varied based on different surface of material [Dietze-1957, TÜV-1984]. For unknown surfaces the reflectance can be assumed with  $\rho_g = 0.2$  [Perez-1986].

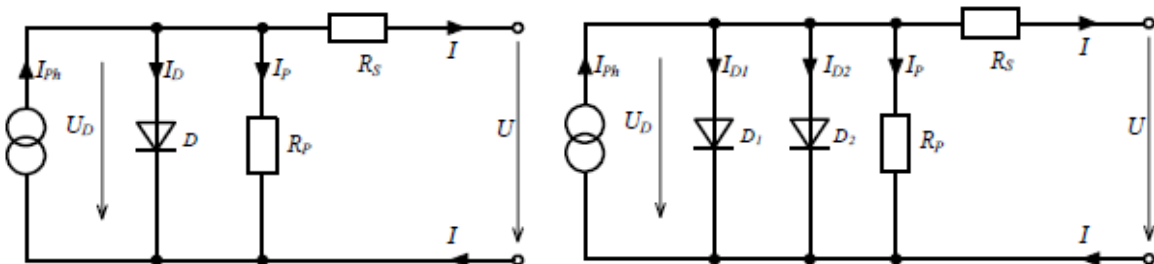
$$G_{r,i} = 0.5 \cdot \rho_g \cdot G \cdot (1 - \cos \alpha_{PV})$$

3.15

The summation of direct, diffuse and ground reflected irradiation above is the amount of total power input faced on a PV-module surface. In order to evaluate the amount of real power input on the PV-cell, however, the reflection loss and dispersion loss of spectrum distribution need to be taken into account.

### 3.3.2 Electrical Power

In the literature, various equivalent circuits are used to describe the electrical behaviour and predict the power output of solar cells, 1-, 2-diode models. Figure 3-5 shows the equivalent circuit diagrams of 1- and 2-diode models together with their equations. However, the constant parameters need to be identified in these equivalent circuits. All parameters of the equations above are assumed at a constant temperature of 25 ° C. These parameters are also influenced by the operating temperature. In the real application, these constant parameters are not always identical from cell to cell or module to module. Moreover, these models are not applicable for thin-film modules, especially amorphous, micro-amorphous or tandem silicon solar cells.



$$0 = I_{ph} - I_S \cdot \left[ \exp\left(\frac{U + IR_S}{mU_T}\right) - 1 \right] - \frac{U + IR_S}{R_p} - I$$

$$0 = I_{ph} - I_{S1} \cdot \left[ \exp\left(\frac{U + IR_S}{m_1 U_T}\right) - 1 \right] - I_{S2} \cdot \left[ \exp\left(\frac{U + IR_S}{m_2 U_T}\right) - 1 \right] - \frac{U + IR_S}{R_p} - I$$

**Figure 3-5** Equivalent circuit of 1- and 2-diode models together with their IV-curve equations.

Glottzbach tried to describe the electrical characteristics of a PV-module without knowing any physical characteristics of solar cells. This was done by implementing an artificial neural network. The errors are lower than 1%, which is low compared to the diode models above [Glottzbach-2011]. Using the diode models and ANN models,

the IV-curve of a PV module can be achieved. This IV-curve will be useful for the system design together with the MPP tracker of inverters. However, the computational calculation for this IV-curve is quite complex.

Module efficiency is another method to predict the electrical power output of a PV module. The most widely known model to predict the real-time efficiency of a PV-cell ( $n_c$ ) is given (3.16), where  $T_{STC} = 25^\circ\text{C}$ ,  $\gamma = 0.12$  [Mattei-2006, Cucumo-2006]:

$$n_c = n_{STC} \cdot \left[ 1 - \beta \cdot (T_c - T_{STC}) + \gamma \cdot \log \left( \frac{G_T}{1000} \right) \right] \quad 3.16$$

With  $\gamma = 0$ , the linear dependency of  $n_c$  on operating temperature could be achieved as the most simplified models for electrical power prediction (3.17) [Kohle-2003].

$$n_c = n_{STC} \cdot [1 - \beta \cdot (T_c - T_{STC})] \quad 3.17$$

Durisch has developed a semi-empirical PV-cell efficiency model, where  $G_0 = 1000 \text{ W/m}^2$ ,  $AM_0 = AM1.5$  [Durisch-2007]. The parameters a, b, c, d, e, f and g are regression coefficients with values of 1.249, -0.241, 0.193, 0.244, -0.179, 0.037 and 0.073, respectively, and R2 of 0.99 which were determined using measured data from the Dublin site (3.18).

$$n_c = n_{STC} \cdot a \left[ b \cdot \frac{G_T}{G_0} + \left( \frac{G_T}{G_0} \right)^c \right] \cdot \left[ d + e \frac{T_c}{T_{STC}} + f \frac{AM}{AM_0} + \left( \frac{AM}{AM_0} \right)^g \right] \quad 3.18$$

The module performance is influenced by operating temperature as well as degradation, the spectral response of each PV cell technology and module efficiency under low solar irradiation. The long-term degradation can be assumed at around 0.5-1.0% annually due to the degradation of encapsulation in PV modules. This degradation also depends on the different PV-technologies.

With respect to the variation of Air Mass and the corresponding spectrum distribution of solar irradiation, as described in the power input part above, the amount of electrical power output of each PV technology will be different based on its own spectrum response (Figure 3-6a) [Glotzbach-2008]. In order to cover this spectrum loss, certain technologies of solar cell irradiation sensors have to be considered. Figure 3-6b describes the influence of AM on the short circuit current of different PV technologies, relative to the AM 1.5. This influence is relatively small in low AM. King assumed that the spectrum loss on the annual energy yield is smaller than 3% for

typical PV applications, where over 90% of solar energy available over a year happens at an AM of less than 3 [King-2004].

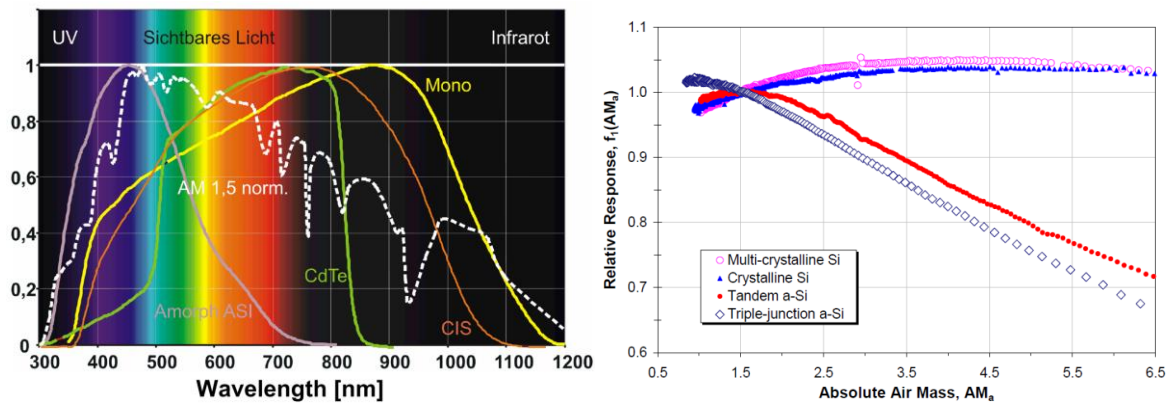


**Figure 3-6** spectrum response of each PV technology (a) and influence of solar spectral variation for different PV technologies, relative to the AM 1.5.

In addition, with respect to the varying shunt resistance in a PV cell, the module efficiency is also influenced under weak-light solar irradiation. The lower the shunt resistance of the PV cell, the lower the module efficiency under weak-light irradiation. These differences in shunt resistance can lead to 10% differences in annual energy yields of photovoltaic systems [Grunow-2004].

In order to cover the influences of module efficiency under varying solar irradiation, especially under weak-light irradiation, together with operating temperature, EN 61853-1 has been introduced to describe the correlation between varying solar irradiation and operating temperature under certain Air Mass values (Table 3-8) [EN 61853-1].

Irradiation (W/m <sup>2</sup> )	Spectrum	Operating temperature			
		15°C	25°C	50°C	75°C
1100	AM1.5	NA			
1000	AM1.5				
800	AM1.5				
600	AM1.5				
400	AM1.5				NA
200	AM1.5				NA
100	AM1.5			NA	NA

**Table 3-8** Short circuit current, power output, open circuit voltage and maximum voltage versus solar irradiation and temperature

### 3.3.3 Dissipation Power

This thermal dissipation power will be dissipated in both front and backside directions through 3 components of heat transport: conduction (**cond**), convection (**conv**) and radiation (**rad**). These heat transport components can be described with heat transfer resistances (**R**) or heat transfer coefficient (**h**), reverse proportional to heat transfer resistance (**1/R**). These are the units to resist the heat flow across material: solid for heat conduction, fluid for heat convection, without a medium for heat radiation. These different types of heat transfer can occur alone or in combination.

#### 3.3.1.1 Conduction Heat Transfer

Conduction heat transfer is the process of heat flow through the solid. It is the proportion of each material thickness ( $d$  in m) to each material's heat conductivity ( $\lambda$  in W/mK). It is reversely proportional to the conduction heat transfer coefficient ( $1/R$ ) (3.19)

$$R = \sum_1^N \left( \frac{d_i}{\lambda_i} \right) \quad 3.19$$

The different heat conduction of material used leads to different surface temperatures and corresponds to the amount of heat dissipation. The higher the heat conduction of material employed, the lower the surface temperature of BIPV module and lower heat dissipation obtained. For most standard PV-modules, the temperature difference between cell and surface is assumed to be neglected. With respect to the multi-layered configuration of a BIPV module, however, this conduction heat transfer coefficient is one of the most important parameters for identifying the surface temperature, which leads to different thermal dissipation. Therefore, it cannot be neglected.

Heat conductivity is usually a temperature-dependent material value. With respect to temperature range in BIPV applications, however, it can also be assumed to be constant and independent from temperature. Table 3-9 describes the material parameters of material used in a BIPV module.



Material used	Density $\rho_m$ (kg/m <sup>3</sup> )	Conductivity $\lambda$ (W/mK)	heat capacity $C_m$ (J/kgK)	Thickness $d_m$ (mm.)
<b>Frontside</b>				
Front glass	2500	0.76 - 1.00	500	3.000
TiO <sub>2</sub>	2400	7.1	691	0.075
EVA-Foil	960	0.35	2090	0.380
<b>PV Cell</b>	2330	148	677	0.200
<b>Backside</b>				
EVA-Foil	960	0.35	2090	0.380
Backsheet	1200	0.20	1250	0.760
Gypsum	2400	0.21	1.09	10.000
Isofloc	40-60	0.045	2150	75.000
Styrodur	33	0.033	1500	50.000
Air	1.184	0.02587	1.006	16.000
Argon	1.784	0.01172	0.5203	16.000

**Table 3-9 Material parameters of BIPV-Modules [Quaschnig-1996, Jones-2001, Armstrong-2010]**

### 3.3.1.2 Radiation Heat Transfer

The radiation heat transfer coefficient depends on surface temperature, surrounding temperature, and the emission value of the surface. However, it is independent from the matter transported. It could be evaluated using 2 components: surface-surrounding radiation heat transfer and 2 parallel plates radiation heat transfer. Table 3-10 describes the calculation of radiation heat transfer coefficients from surface to the surroundings and between 2 parallel glass panes.

2 parallel plates radiation heat transfer coefficient ( $h_{cav,rad}$ ) – heat exchange between 2 parallel plates with different surface temperature; similar to the heat exchange inside the cavity of double glazing, or inside the ventilation behind the PV module in and on-roof applications [Schmid-2000, EN 673]. At the same time, in 2 parallel plates, radiation heat transfer,  $T_{back,mod}$  and  $\epsilon_{back,mod}$ , represents the temperature and emissivity of the module backside, while  $T_{back,cav}$  and  $\epsilon_{back,cav}$  are the temperature and emissivity of the insulated glass pane in the double glazing or in the roof structure in in and on-roof applications. The emission of the insulated glass pane in double glazing can be coated with low-e coating,  $\epsilon = 0.04$ , to reduce the infrared part of solar irradiation and corresponding g-values.

Surface-to-surrounding radiation heat transfer coefficient ( $h_{surf,rad}$ ) – heat exchange between surface front- and backside of BIPV to the surrounding temperature, which could be the sky, earth and internal temperatures [Quaschnig-1996]. Since the module surface in relation to the Earth and sky area is relatively small ( $A_{back,cav} \gg A_{back,mod}$ ), the simplified model could be obtained for surface-surrounding radiation heat transfer, where the  $\alpha_{PV}$  is the tilted angle from horizontal,  $\epsilon_{glass}$  is mostly 0.94,  $\epsilon_{earth}$  is 0.95,  $\epsilon_{sky}$  is 1.00 and  $\sigma$  is Stefan-Boltzmann constant ( $5.67 \times 10^{-8} \text{ W.m}^{-2}.\text{K}^{-4}$ ). The Earth temperature could be assumed as an ambient temperature, while the sky temperature could be assumed as a function of ambient temperature [Swinbank-1963].

<b>2 parallel plates radiation heat transfer coefficient (<math>h_{cav,rad}</math>)</b>
$q = C_{12} \cdot (T_{back,mod}^4 - T_{back,cav}^4)$ $h_{cav,rad} = \frac{q}{(T_{back,mod} - T_{back,cav})}$ $C_{12} = \frac{\sigma}{\frac{1}{\epsilon_{back,mod}} + \frac{1}{\epsilon_{back,cav}} - 1}$
<b>Surface-to-Surrounding radiation heat transfer coefficient (<math>h_{surf,rad}</math>)</b>
$h_{i,surf,rad} =$ $\sum_i^{front,back} \left\{ \left[ \epsilon_{i,mod} \cdot \sigma \cdot \epsilon_{earth} \cdot \frac{(1 + \cos \alpha_{PV})}{2} \cdot (T_{i,mod}^2 + T_{earth}^2) \cdot (T_{i,mod} + T_{earth}) \right] \right. \\ \left. + \left[ \epsilon_{i,mod} \cdot \sigma \cdot \epsilon_{sky} \cdot \frac{(1 - \cos \alpha_{PV})}{2} \cdot (T_{i,mod}^2 + T_{sky}^2) \cdot (T_{i,mod} + T_{sky}) \right] \right\}$ <p>where <math>T_{sky} = 0.0552 \cdot T_{amb}^{1.5}</math></p>

**Table 3-10 Radiation heat transfer coefficients; 2 parallel plates and surface-to surrounding**

### 3.3.1.3 Convection Heat Transfer Coefficient

In addition to the heat conduction in fluid materials, convection heat transfer could occur due to continued movement of the fluid, as described by Nusselt-Nr (**Nu**) and Prandtl-Nr (**Pr**). The Nusselt-Nr is the ratio of convective to conductive heat transfer across the boundary, while the Prandtl-Nr is the characteristics of fluid materials. The convection heat transfer is composed of forced and natural convection.

The forced convection is related to the length of the module (**l**), wind speed (**w**) and heat conductivity (**λ**) of air. It does not depend on the surface temperature and tilt angle (**α<sub>PV</sub>**). In natural convection, the fluid motion is not generated by any external source of wind speed (**w**); but only by differences in density (**Δρ**) and the corresponding pressure drop in the fluid occurring due to temperature gradients, described by buoyancy force [Brinkworth-2000]. It further depends on the tilt angle (**α<sub>PV</sub>**) on the front or backside and individual surface temperature.

Figure 3-7 – Figure 3-10 describe the flow chart of a natural and free ventilation surface, natural convection in a channel and forced convection [VDI-2008]. The green lines in the following flow charts represent most cases happening within the natural flow.

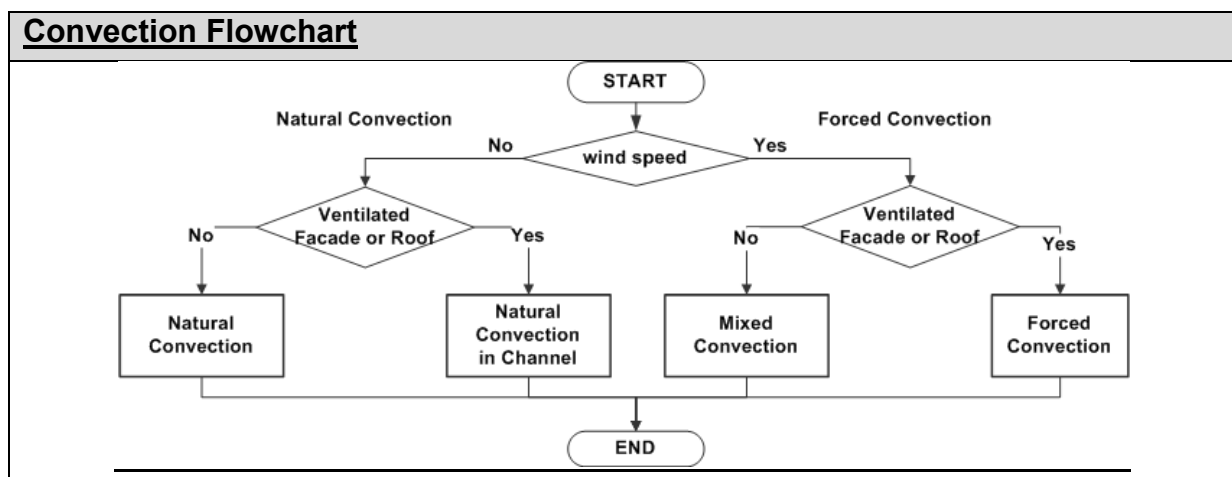


**Figure 3-7 Holistic approach of convection heat transfer coefficients**

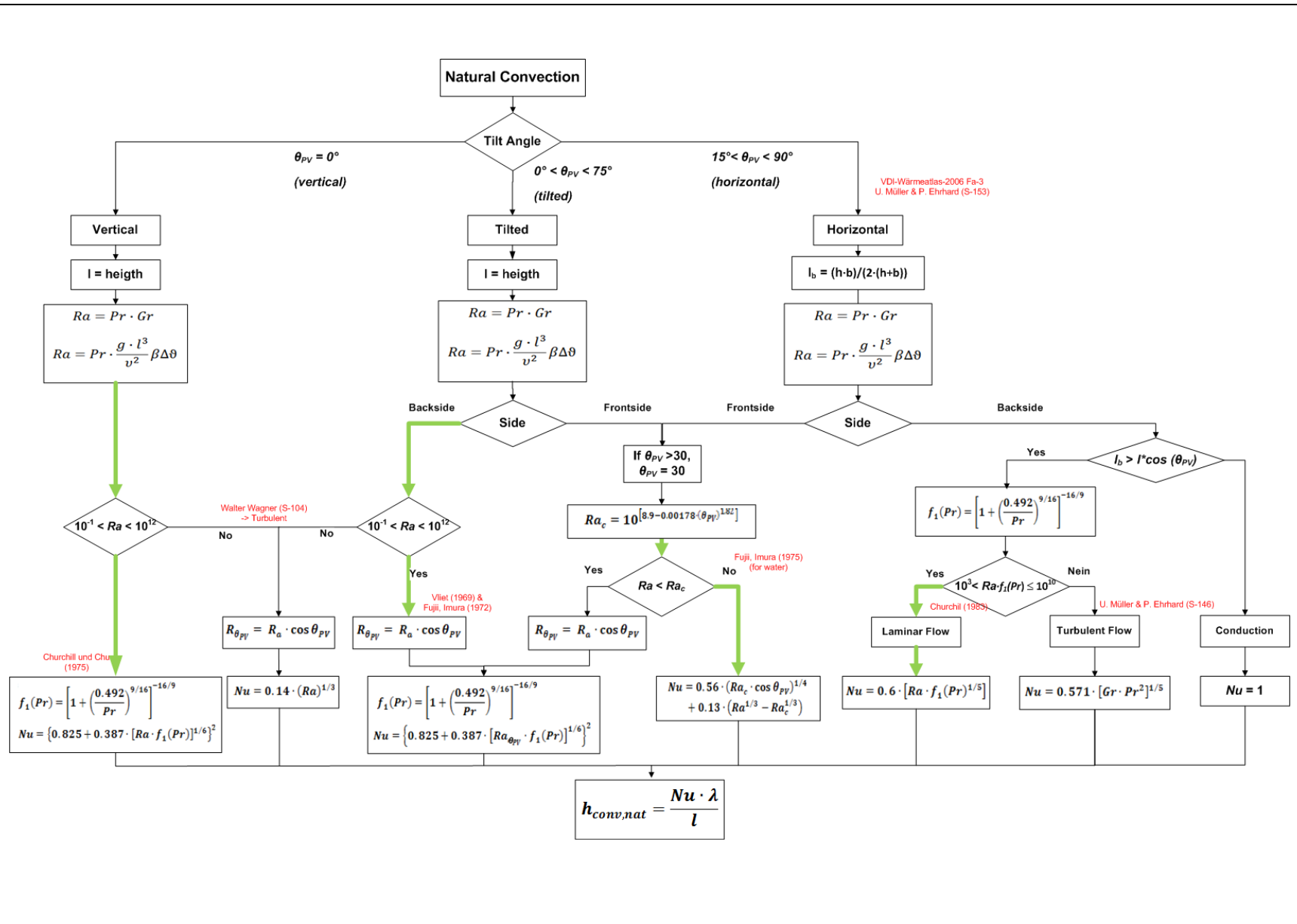


Figure 3-8 Flow chart of natural convection with free ventilation at different tilted angles

For the natural convection, the buoyancy force is the main driving force in the natural flow system. This difference in pressure results in a net force that tends to accelerate an object only upwards. The magnitude of that force is proportional to the difference in the pressure between the top and bottom of the column. This is the function of design and operating parameters, such as incident solar radiation, geometry, orientation and ambient temperature, etc.

The natural convection with free ventilation is classified with module tilt angles ( $\alpha_{PV}$ ). In building application, these tilted angles have been considered inverted when compared to PV application ( $\theta_{PV}$ ): vertical ( $0^\circ$ ), tilted ( $0^\circ$ - $75^\circ$ ) and horizontal ( $75^\circ$ - $90^\circ$ ). To evaluate the convection heat transfer coefficient, the Rayleigh number ( $Ra$ ) is the critical parameter obtained by Prandtl-number ( $Pr$ ) and Grashof-number ( $Gr$ ), while  $Gr$  can be calculated with gravity ( $g$ ), module length ( $l$ ), viscosity of fluids ( $\nu$ ), temperature differences ( $\Delta\theta$ ) and average temperature ( $\beta = T_{avg}^{-1}$ ) between surface and surrounding temperatures. Afterwards, the Nusselt-number ( $Nu$ ) can be calculated. Together with the module length ( $l$ ) and the heat conduction ( $\lambda$ ) of fluid, the natural convection heat transfer coefficient ( $h_{conv,nat}$ ) can finally be obtained (Figure 3.8).

In the case of vertical flow, the surface and surrounding temperatures are the main parameters for the natural convection heat transfer coefficient ( $h_{conv,nat}$ ), while other parameters are identical on the front and backside of the BIPV module. In case  $Ra$  rises over  $10^{12}$ , the turbulent flow dominates this convection.

Regarding tilted and horizontal installations, the front-and backside have to be considered separately due to the different buoyancy force. The front side is influenced by the critical Rayleigh-number ( $Ra_c$ ). The  $Ra_c$  represents the boundary layer from laminar flow to turbulent flow. In the case of  $Ra > Ra_c$ , the turbulent flow will dominate, which can occur with a lower tilted angle. At the front side, the variable buoyancy force occurs until the tilted angle of  $30^\circ$ . At a tilted angle higher than  $30^\circ$ , the amount of heat transfer will no longer be influenced by tilted angles. It will only be influenced by temperature differences between the surface and surrounding temperature. On the backside of a tilted installation, the heat transfer coefficient is influenced by the cosine of the tilted angle ( $\cos \theta_{PV}$ ). On the backside of a horizontal installation, however, the characterized length ( $l_b$ ) was introduced due to the self-limitation of the PV module, wherein the buoyancy force cannot flow upwards. The buoyancy force could not take place in case of  $l_b < l \cdot \cos(\theta_{PV})$ . Therefore, the conduction heat transfer will be occupied ( $Nu = 1$ ). The green-line represents the convection path in which the fluid considered is air.

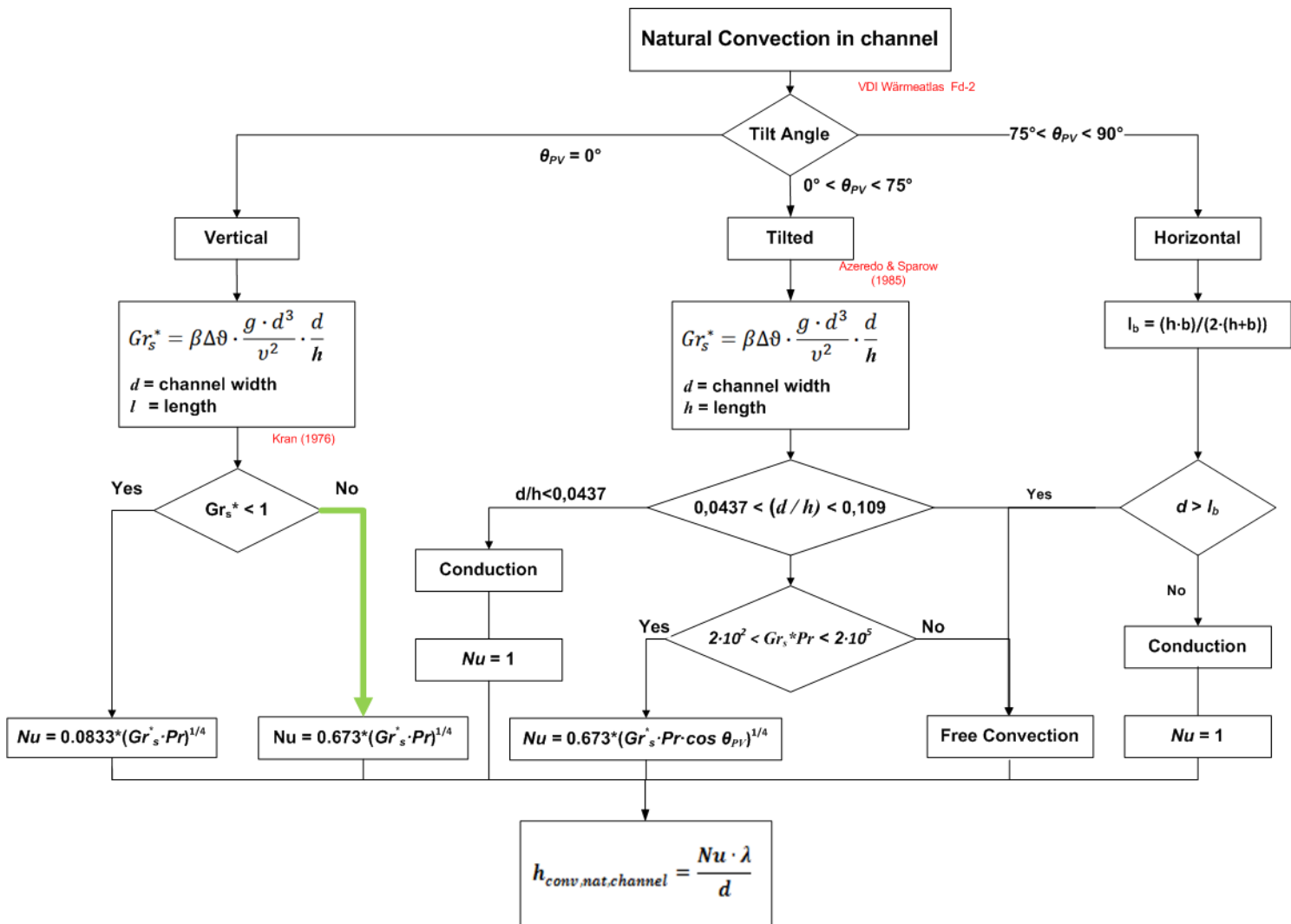


Figure 3-9 Flow chart of natural convection in channel at different tilted angles

For the natural convection in the channel, only the inside surface is considered. In order to calculate the Nusselt-number and the corresponding convection heat transfer coefficients, the correction of Grashof-number ( $Gr_s^*$ ) is needed together with the channel's distance ( $d$ ). For a vertical and tilted module, the parameters of the channel distance ( $d$ ) and module length ( $l$ ) are important to classify the type of heat transfer coefficient. As of  $d / l < 0.0437$ , the conduction heat transfer coefficient will be occupied ( $Nu=1$ ), while  $d/l > 0.109$ , the natural convection with free ventilation, will be occupied. Moreover, the  $Gr_s^* \times Pr$  is another parameter to classify the type of convection between laminar or turbulent flows. For a horizontal module, the characterized length ( $l_b$ ) is the critical parameter. In the case of  $d > l_b$ , the natural convection without a channel will be occupied. In the case  $d < l_b$ , however, the conduction heat transfer coefficient will be occupied ( $Nu=1$ ) (Figure 3-9).

In forced convection, the Renolds-number ( $Re$ ) is a critical parameter to classify the type of forced convection. It depends only on wind speed, module length and fluid conductivity, not on temperature, gravity or viscosity, like natural convection above (Figure 3-10). In order to evaluate the total convection heat transfer coefficients, the combination of natural and forced convection has to be taken into account (3.20).

$$h_{conv} = (h_{nat}^3 + h_{for}^3)^{(1/3)} \quad 3.20$$

To differentiate the natural flow to forced flow on a free ventilation surface, Tonui confirmed that the natural air flow rate corresponds to 0.0 – 0.1 m/s [Tonui-2008]. He did this with the measurement of a PV/T air collector, which is a hybrid collector with the combination of a PV and solar thermal system based on an air medium. Meanwhile, using the experimental and mathematical model on a c-Si PV-module in a log-log diagram, Breteque explained that the natural convection can be assumed with a wind speed lower than 0.25 m/s [Breteque-2009]. At the same time, Krauter explained that heat transfer by natural convection could be more than by forced convection for air velocity lower than 1m/s [Krauter-1999]

Regarding convection heat transfer in channels, Ciampi also concluded that energy saving increases as the air channel width  $d$  rises; and such a rise turns out to be particularly marked by  $d < 0.15$  m. The use of carefully designed ventilated facades will allow energy saving that even exceeds 40% in the summer cooling of buildings [M.Ciampi-2003].

## Forced convection

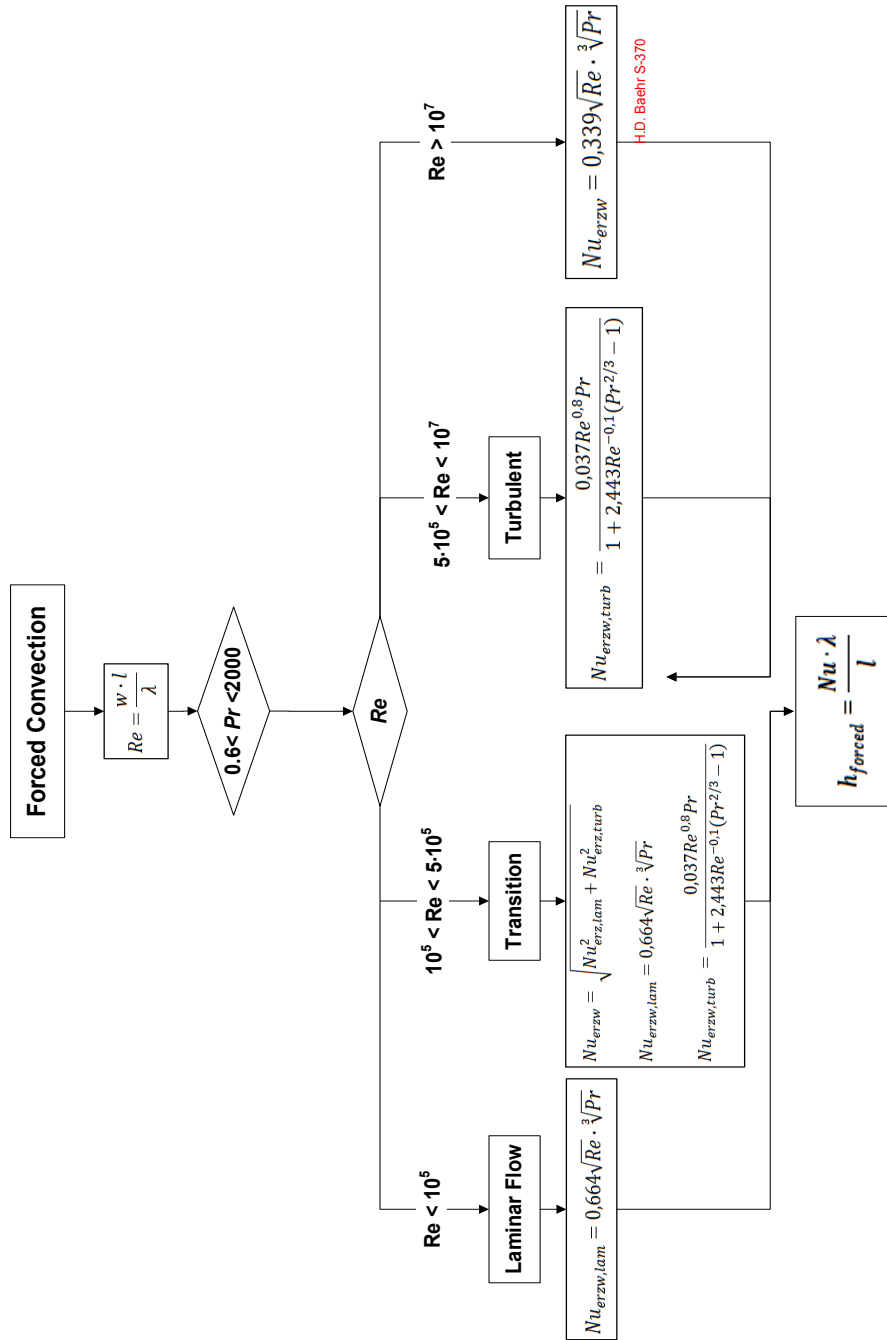


Figure 3-10 Flow chart of forced convection

By means of building simulation or building codes, the total internal and external heat transfer coefficients ( $h_i$  and  $h_e$ ) are considered. They are the summation of convection and radiation heat transfer coefficients ( $h_{conv}$  and  $h_{rad}$ ) on the front and backside (3.21).

$$h_{i,e} = h_{rad-i,e} + h_{conv-i,e}$$

3.21



### 3.3.1.4 Correlation of three heat transport components: conduction, convection and radiation

In terms of thermal dissipation, there is a great deal of research related to convection and radiation heat transfers. They assume that the surface temperature is equal to cell temperature. With respect to the multi-layer BIPV module and corresponding higher heat conduction resistance on the backside, the surface temperature is not equal to cell temperature. Therefore, heat conduction, convection and radiation need to be considered together [Figure 3 11].

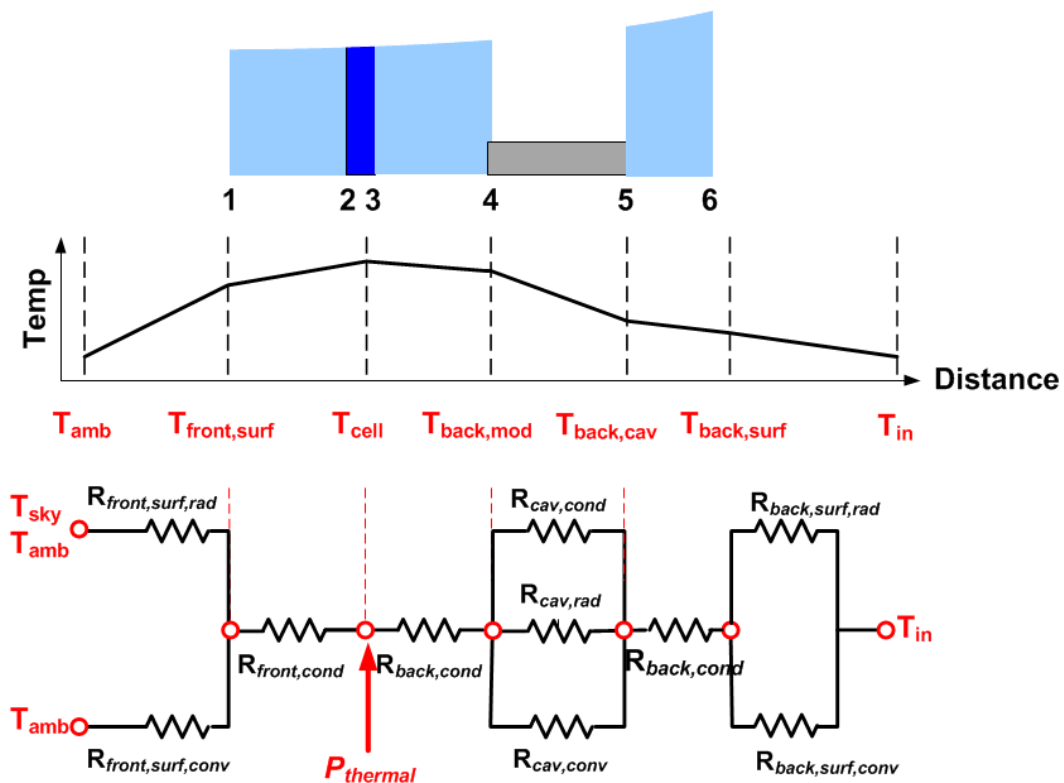


**Figure 3-11 Equivalent electrical circuit flow of heat transfer resistances together with temperature gradient from PV cell to ambient temperature**

Figure 3-11 describes the correlation of three heat transport components and the temperature gradient in both directions based on heat transfer resistances ( $R$ ) in the equivalent electrical circuit diagram. The amount of dissipation thermal power in PV cells ( $P_{thermal}$ ) acts as a heat source, which influences the temperature differences between the solar cell and surrounding ( $T_c - T_{amb}$ ) and total heat transfer resistances on the front and backside ( $\Sigma R_{f,b}$ ). Table 3-11 describes the relationship among dissipation thermal power, temperature differences and heat transfer resistances. The external and internal heat transfer coefficients are the combination of the convection and radiation heat transfer coefficients ( $h_{surf,rad} + h_{surf,conv}$ ) on each

side. In the case of insulated glass, the heat transport in the cavity is the combination of conduction ( $h_{cav,cond}$ ), natural convection ( $h_{cav,conv}$ ) and radiation ( $h_{cav,rad}$ ) heat transfer coefficients between two parallel surfaces. For most insulated glass filled with inert gas, the Nusselt-number of the inert gas becomes lower than one. Therefore, the conduction heat transfer coefficient is playing a major roll compared to the natural convection heat transfer coefficient.

Total power dissipation
$P_{thermal} = \sum \frac{1}{R_{front}} \cdot (T_c - T_{amb,sky}) + \sum \frac{1}{R_{back}} \cdot (T_c - T_{in})$
Power dissipation at front side
$P_{thermal,front} = \sum \left[ \frac{1}{R_{f,cond}} + \frac{1}{R_{f,surf,rad}    R_{f,surf,conv}} \right] \cdot (T_c - T_{amb,sky})$
$P_{thermal,front} = \sum \left[ \frac{1}{R_{f,cond}} + (h_{f,surf,rad} + h_{f,surf,conv}) \right] \cdot (T_c - T_{amb,sky})$
Power dissipation back front side
$P_{thermal,back} = \sum \left[ \frac{1}{R_{b,cond}} + \left( \frac{1}{R_{cav,rad}    R_{cav,conv}} \right) + \frac{1}{R_{b,cond}} + \left( \frac{1}{R_{b,surf,rad}    R_{b,surf,conv}} \right) \right] \cdot (T_c - T_{in})$
$P_{thermal,back} = \sum \left[ \frac{1}{R_{b,cond}} + (h_{cav,rad} + h_{cav,conv}) + \frac{1}{R_{b,cond}} + (h_{b,surf,rad} + h_{b,surf,conv}) \right] \cdot (T_c - T_{in})$

**Table 3-11 Calculation of thermal power dissipation on both front- and backside**

In this temperature model, the most important parameter is the surface temperature on both the front and backside. They are directly related to the amount of power dissipation, internal and external heat transfer coefficient for identification of relevant building functions, and energy consumption as well as thermal comfort in building simulation. The surface temperature is proportional to the total heat transfer resistance of material used in PV modules ( $R_{mat-f,b}$ ) (3.22) to the total heat transfer resistance ( $R_{total-f,b}$ ) (3.23), including the radiation and convection heat transfer coefficients (3.24).

$$R_{mat-f,b} = \left[ \sum_i^{f,b} \frac{d_i}{\lambda_i} + \frac{1}{h_s} \right] \quad 3.22$$

$$R_{total-f,b} = \left[ \sum_i^{f,b} \frac{d_i}{\lambda_i} + \frac{1}{h_s} \right] + \left[ \frac{1}{h_{rad-f,b}} + \frac{1}{h_{conv-f,b}} \right] \quad 3.23$$

$$T_{surface-f,b} = \frac{R_{mat-f,b}}{R_{total-f,b}} (T_C - T_{out,in}) \quad 3.24$$

### 3.3.4 Absorption Power

For a standard PV module, the absorption of material and corresponding thermal capacity of standard PV module is too small and can be neglected. In steady state condition, the power input will be converted into electrical power and thermal power, which the thermal power will be completely dissipated to surrounding. Therefore, this power balance model can be explained by thermal resistance models for energy transfer analysis without any capacity in the model, as described in Table 3-11.

With respect to multi-layered configuration of BIPV modules, however, the thermal absorption part and its corresponding thermal capacity become critical. It leads to a time-delay in the operating temperature under fluctuated solar irradiance on a cloudy day. This time-delay could be more than 15 minutes for standard PV modules [Jones-2001]..Therefore, the steady state models could not be used for short time resolution application; e.g., real-time power output for self-consumption, grid integration applications or real-time building simulation.

Figure 3-12 describes the time-delay operating temperature of 2 different multi-layered configurations under rapid change of solar irradiation (module\_1 for PV laminated glass, module\_2 for PV laminated glass with 5 cm thermal insulation). The measurement was done with a time resolution of 15sec. It can be seen that the solar irradiation changes from 600 W/m<sup>2</sup> to 100 W/m<sup>2</sup> in 30 sec, while the operating temperature decreases from 27°C to 12°C (ΔT = 15K) and 19°C to 9°C (ΔT = 10K) in 35 minutes for module\_2 and module\_1, respectively. In order to define the heat capacity of the module, the time constant has to be defined as the time taken for the module temperature to reach a 63% reduction from a step change in solar irradiation, which was 22 and 17 minutes for module\_2 and module\_1, respectively. Hence, it can be concluded that the variation of module temperatures reduction represents the variation of the BIPV module's heat capacity.

This time-delay operating temperature leads to a variation in the electrical power output. Moreover, it leads to a different surface temperature and corresponding thermal relevant building functions via thermal power dissipation through convection and radiation. In order to solve this real-time (dynamic) behaviour, the absorption part caused by the heat capacity of material used has to be taken into account in the temperature model.

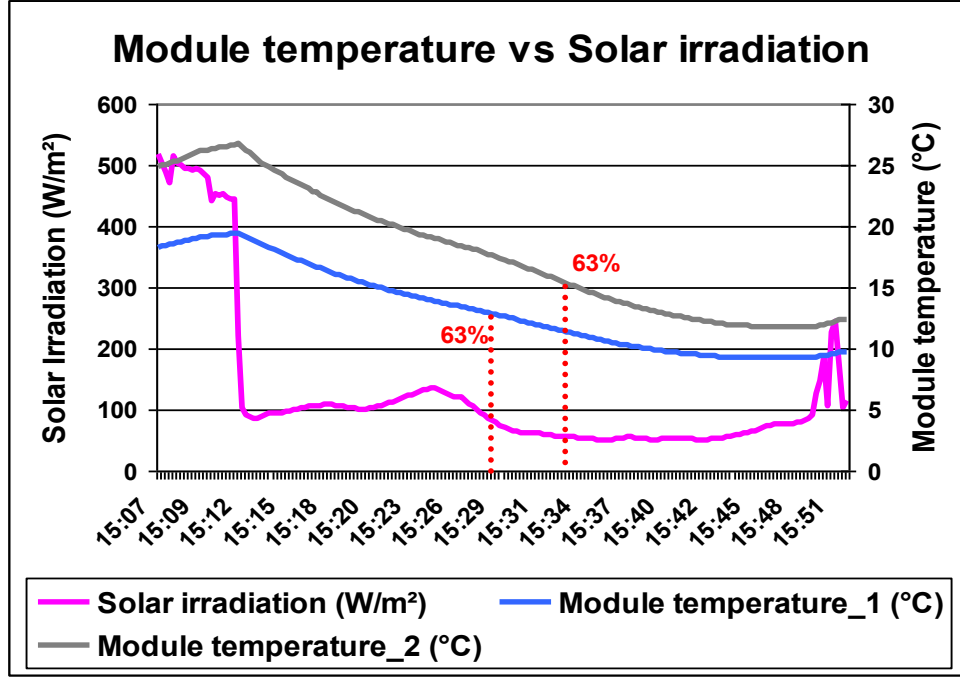


Figure 3-12 Time-delay operating temperatures to fluctuated solar irradiation

$$P_{input} = P_{electrical} + P_{dissipation} + P_{absorption} \quad 3.25$$

$$C_M \cdot \frac{dT_M}{dt} = P_{absorption} = (P_{input} - P_{electrical} - P_{thermal}) \quad 3.26$$

In a real-time (dynamic) model, the power input will be converted into electrical power and thermal power. However, the thermal power will be classified into 2 components: dissipation to surrounding ( $P_{dissipation}$ ) and absorption ( $P_{absorption}$ ) in module (3.25). These are fundamental formulas in the power balance model [Jones-2001]. This absorption component will increase the module temperature and corresponding surface temperature until reaching the steady state, where the thermal power can be completely dissipated into the surrounding (3.26). In order to solve the real-time (dynamic) model, the iteration method has been implemented (3.27).

$$\Delta T_M = (T_{M,i+1} - T_{M,i}) = \frac{\Delta t}{C_M} \cdot (P_{input} - P_{electrical} - P_{thermal}) \quad 3.27$$

With respect to the multi-layers of BIPV module, the total thermal capacity of the BIPV module is the summation heat capacity of each layer (3.28). The density ( $\rho_i$ ), module area ( $A$ ) specific heat capacity ( $C_i$ ) and usual thickness ( $d_i$ ) of each material used ( $n$ ) in the BIPV module can be found in Table 3-9

$$C_M = \sum_i^n A \cdot d_i \cdot \rho_i \cdot C_i \quad 3.28$$

## 4. Mechanical Models

The mechanical behaviour are the key parameters to define the mechanical load resistance and risk of failure modes, e.g. glass breakage, weatherproof defects, cell breakage, etc. As mentioned in Chapter 2, most of the BIPV modules are manufactured based on laminated glass configurations, wherein the mechanical behaviour lies between two limits: the layered limit, which is the lower limit of 2 single glass panes, and the monolithic layer, which is the upper limit of monolithic glass.

To study the behaviour of the BIPV modules, it is important to know the physical properties of glass layers, and especially commonly used interlayer materials. In this chapter, the basic principles of the load resistance of BIPV modules, defined as laminated glass, are described together with their mechanical behaviour in terms of stress ( $\sigma$ ) and deflection ( $d$ ).

### 4.1 Physical parameters

#### Stress

An external force ( $F$ ) applied to an object is reacted by internal forces set up within the material. If, therefore, an object is subjected to a uniform force, which is uniformly or equally applied across the cross-section area ( $A$ ) of the material, then the object generates a force inside called **stress**. It is expressed as a unit of  $N/m^2$ .

Since stress can be separated into compression/tension stress ( $\sigma$ ) and shear stress ( $\tau$ ) (4.1), the compress/tension stress ( $\sigma$ ) occurs when a normal force ( $F_n$ ) is applied across the area ( $A$ ), while the shear stress ( $\tau$ ) occurs when a shear force ( $F_s$ ) is applied across the surface (Figure 4-1).

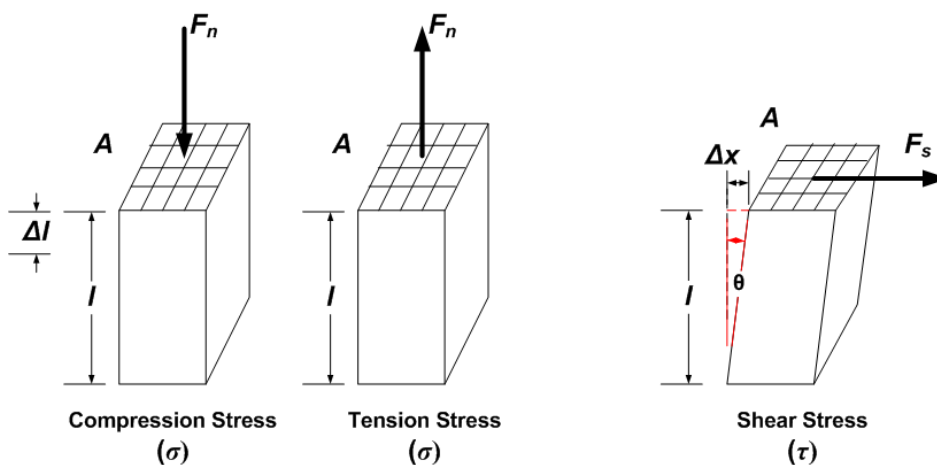


**Figure 4-1** Compression/Tensile stress ( $\sigma$ ) and shear stress ( $\tau$ )

$$\sigma = \frac{F_n}{A} \qquad \tau = \frac{F_s}{A} \qquad 4.1$$

### Strain

Compared to a reference object without an external load, displacement occurs when the object is subjected to a load. If the object has an original length ( $L$ ) and changes in length by an amount ( $\Delta L$ ), the ratio of the elongation or contraction ( $\Delta L$ ) to the original length ( $L$ ) is called strain. Strain could also be considered in compression/tension strain ( $\epsilon$ ) or shear strain ( $\gamma$ ) (4.2)

$$\epsilon = \frac{\Delta L}{L} \qquad \gamma = \frac{\Delta x}{l} \qquad 4.2$$

Strain is an absolute number having no unit. Usually, the ratio is an extremely small value, and is expressed by suffixing “ $\times 10^{-6}$ ” or “ $\mu\text{m/m}$ ”.

### Deflection

In case the object is loaded with a weight, the deflection ( $d$ ) that occurs depends on Young's modulus of materials (Figure 4-2).

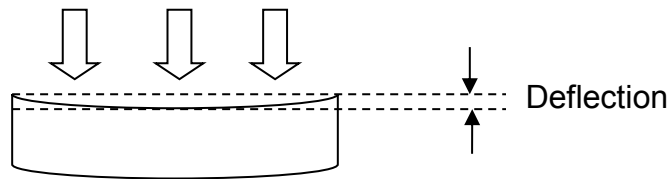


**Figure 4-2 Deflection of object under load**

### Young's modulus and shear modulus

Young's modulus ( $E$ ), also known as the elasticity, compressed or tensile modulus and shear modulus, ( $G$ ) are the characteristics of a material which describe the stiffness of a material against normal and shear forces respectively. Young's modulus or shear modulus is a relation between strain and stress of an elastic material (4.3). It has already been obtained experimentally. The region where stress and strain have a linear relation is called the proportional limit which satisfies the Hooke's law.

$$E = \frac{\sigma}{\epsilon} = \frac{F_n/A}{\Delta l/l} \qquad G = \frac{\tau}{\gamma} = \frac{\tau}{\tan \theta} = \frac{F_s/A}{\Delta x/l} \qquad 4.3$$

The transition between Young's modulus and shear modulus could be achieved via Poisson's ration ( $\nu$ ) (4.4).

$$G = \frac{E}{2 \cdot (1 + \nu)}$$

4.4

## 4.2 Interlayer Properties

The rapid growth of PV applications has acted as a catalyst for the development of new materials and components in photovoltaic (PV) modules. The Ethylene-co-Vinyl Acetate (EVA) interlayer has historically been used to encapsulate the PV cell, whereas the Polyvinyl butyral (PVB) interlayer has been used in conventional building products, such as laminated safety glass. However, new polymeric materials in PV modules have also been developed. Poly ethylene-co-methacrylic acid metal salt (ionomer), polyvinyl butyral (PVB), thermoplastic urethane (TPU), poly- $\alpha$ -olefin (PO), and poly dimethylsiloxane (PDMS) have been proposed for the same application. EVA, PO, and PDMS are thermosets (characterized by cross-linked networks). Ionomer, PVB, and TPU are thermoplastics (increasingly susceptible to viscoelastic flow as the temperature is increased above their glass and melt-transition temperatures -  $T_G$ ,  $T_M$ ) [Miller-2010].

In order to compare the mechanical behaviour of laminated glass, the shear modulus of PVB and EVA interlayers, which represents the material used as laminated glass in building products and PV-module applications, respectively, will be investigated explicitly.

### 4.2.1 Shear Strength of the Polymeric Interlayer

Shear strength is one of the several quantities used to measure the stiffness of polymeric interlayers. It describes the material's response to shearing strains. This shear strength is the operating temperature and load duration time dependent. This shear strength is one of the main factors that influence the mechanical behaviour of laminated glass. The higher the shear strength of the interlayer, the higher the stiffness of laminated glass achieved. It can be described with shear storage modulus ( $G'$ ) and shear loss modulus ( $G''$ ), which measure the stored energy, representing the elastic portion, and dissipated energy as heat, representing viscous portion. In the study of shear strength of the polymeric interlayer, it is important to understand the mechanical behaviour of polymers, which are time and temperature dependent.



#### 4.2.1.1 Temperature Dependency

Figure 4-3 represents the temperature dependency of the shear storage modulus for the polymeric interlayer, where the glass transition temperature ( $T_G$ ) is the temperature at which the polymer starts to move from a solid and relatively brittle state into a molten or rubber-like state. This behaviour depends on the thermodynamic properties of thermoplastics. Thermoplastic materials are mainly useful in the glassy region when they are solid. As the temperature of a polymeric material drops below  $T_G$ , it behaves in an increasingly brittle manner. As the temperature rises above the  $T_G$ , the polymeric materials become rubbery [Schuler-2003]. In the glass state, the chain molecules cannot move. In this state they behave as an energy-elastic behaviour of thermoplastics, for example, the strains after unloading are completely reversible. At temperatures above the glass transition temperature, the chain molecules can now move and behave as entropic-elastic behaviour [Bucak-2006]. This means that the deformations are reversible but delayed in time, known as viscous properties. The phase transition from solid to liquid is completely reversible. That means it can be repeated several times without changing the properties of the materials [Schuler-2003]. As long as it reaches melting temperature ( $T_M$ ), the phase transition from solid to fluid is not reversible. The solid state of the polymer could be reversed. Above the point of the destruction temperature ( $T_Z$ ), the chain molecules are destroyed [Figure 4-3]. This phase transition behaviour is called thermo-mechanic behaviour.

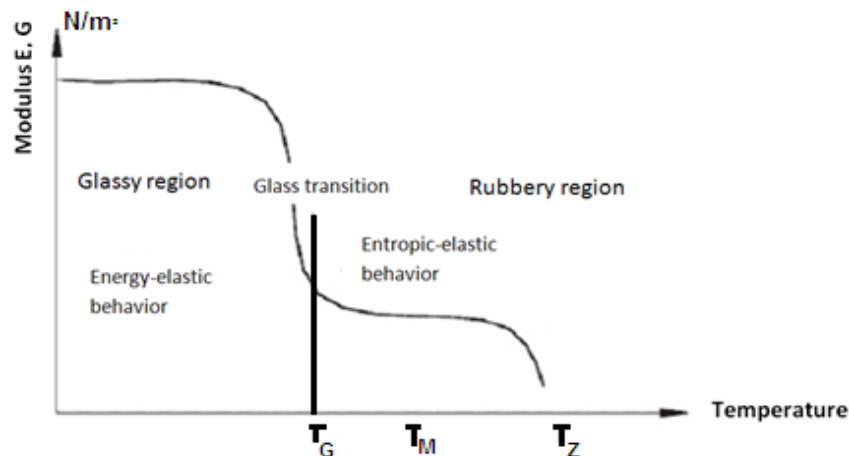


**Figure 4-3 Schematic dependency of the shear storage modulus of thermoplastics on temperature [Schuler-2003]**

Each type of interlayer has its own thermo-mechanic behaviour. Figure 4-4 describes the thermo-mechanic behaviour of different interlayers. It can be seen that the shear storage module of different interlayers decreases with a higher operating

temperature. The storage modulus when the standard PVB film is at a low temperature (below 25°C) is higher than EVA and other interlayers, even over a wide temperature range. However, at temperatures above 50°C, the operating temperature in BIPV applications, the rather gradual EVA and other interlayers' curves verify better applicability as a building product compared to the sharp decline of the PVB curves [Weller-2009].

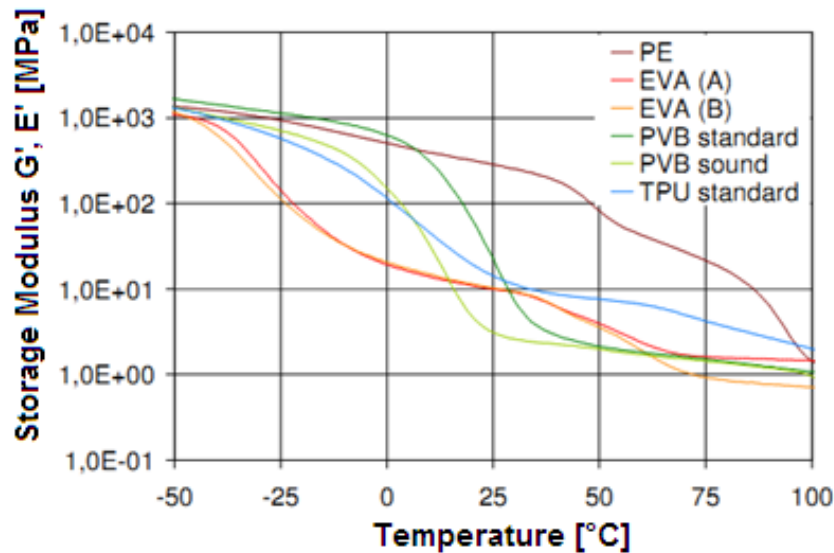


**Figure 4-4 Thermo-mechanic behaviour of various polymeric interlayer materials used in glass and PV industry [Weller-2009].**

#### 4.2.1.2 Load Duration Dependency

The mechanical behaviour of a thermoplastic interlayer can be described by viscoelasticity. Viscoelasticity describes the time-delay of shear storage modulus ( $G'$ ) of interlayers, so-called creep rate of interlayer. It is a completely reversible behaviour of material under external mechanical loads. This behaviour is explained by the process of creep and relaxation.

**Creep** - If the interlayer is subjected to a constant stress or load in its elastic deformation area, then strain or deformation increases with the time in the loading direction (constant stress – time-delay strain). Its deformation does not occur suddenly but takes place very slowly in the direction of “strain relief” (Figure 4-5-A).

**Relaxation** – It describes how viscoelastic materials relieve stress or load as a function of time under constant strain (constant strain – time-delay stress). In stress relaxation, one applies a constant strain, and the response is measured in terms of a decrease in stress as a function of time (Figure 4-5-B).

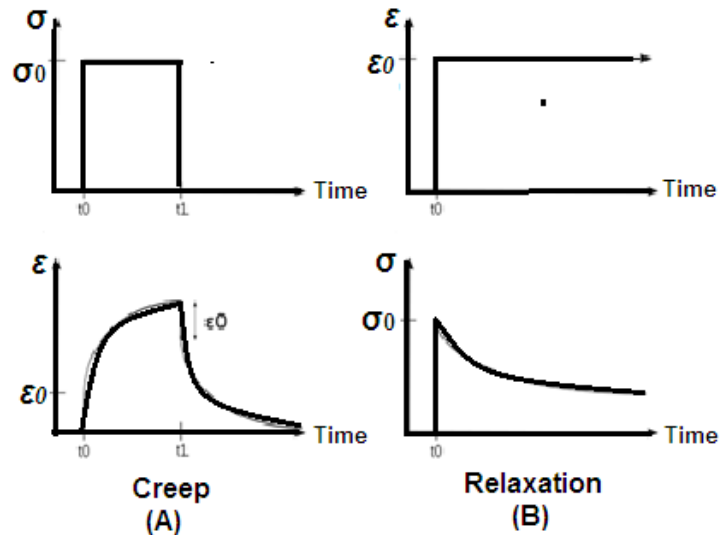


**Figure 4-5 Creep and relaxation characteristics of interlayers.**

Figure 4-6 represents the relaxation characteristics of laminated glass with different interlayers with and without solar cells at room temperature. The EVA-Interlayer exhibits a low creep compared to the PVB and TPSE interlayers.

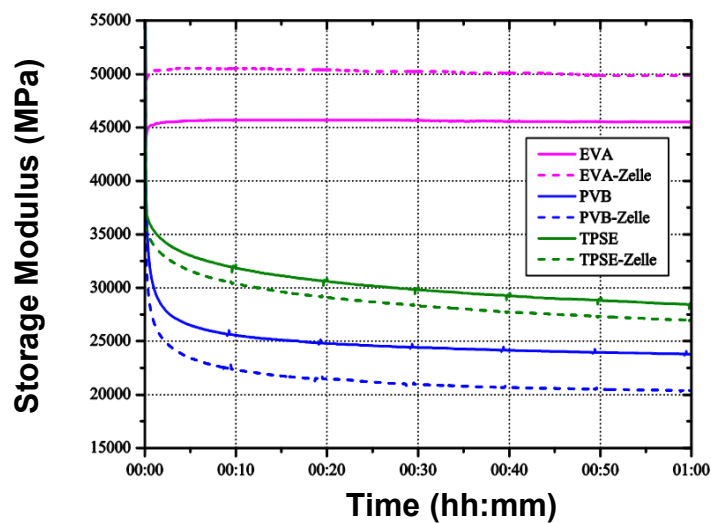


**Figure 4-6 Storage modulus of different interlayers with and without solar cell strings. [Klausing -2009]**

These creep and relaxation behaviour of polymer interlayers are measured in order to provide the characteristics of the shear storage modulus over load duration. Based on this creep and relaxation measurement, the characteristics models of each interlayer can be developed for the static calculation of laminated glass, as described in chapter 4.2.3.

#### 4.2.1.3 Temperature and Load Duration Dependency

In practise, the mechanical behaviour of the BIPV module is subjected to different operating temperatures and load durations at the same time, called thermo-mechanical behaviour. Therefore, both dependencies have to be considered together. Figure 4-7 describes the creep characteristics of the PVB-interlayer with a different operating temperature, while Figure 4-8 describes the relaxation characteristic of the EVA-interlayers [Sobek-2000], [Eitner-2010]. As mentioned in chapter 4.2.2.2, both measurements are used for the development of the characteristic model of each interlayer. It can be evaluated that the creep rate of PVB-interlayer decreases faster than EVA-interlayer [Dietrich-2009]. In Figure 4-8, the creep rate of the EVA-interlayer is nearly zero at a higher operating temperature. Therefore, it can be concluded that the mechanical behaviour of the interlayer mainly depends on the operating temperature and load duration. This shear modulus of interlayer can be measured by a Dynamic Mechanic Analysis (DMA) experiment. A strip of interlayer was used by scanning the operating temperature from -50 °C to 100 °C at frequencies of 0.5 Hz, 1 Hz, 5 Hz and 10 Hz [Weller-2009].

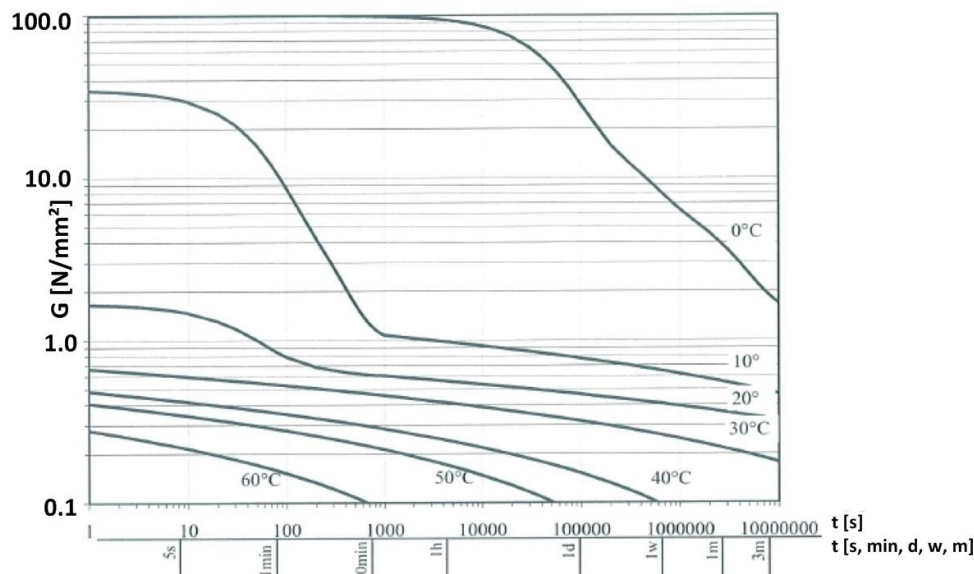


**Figure 4-7 Creep characteristics of PVB based on different operating temperature over time [Sobek-2000]**

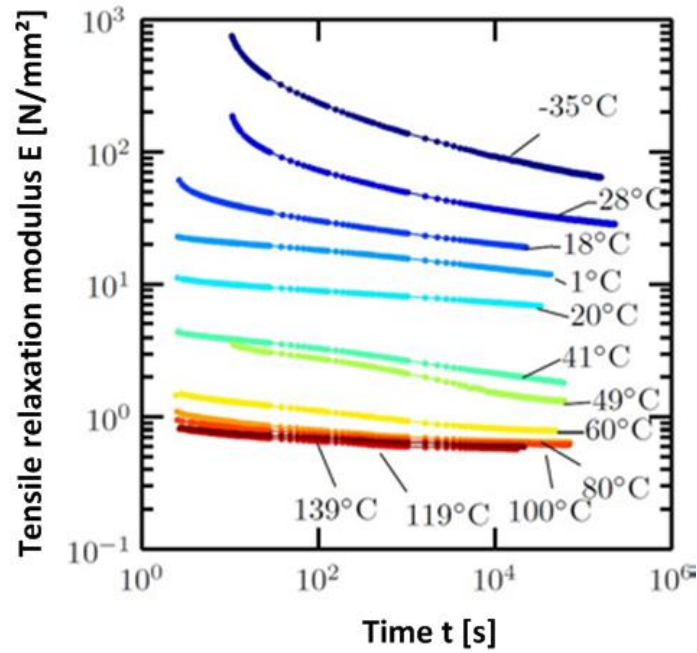


**Figure 4-8 Relaxation characteristic of EVA based different operating temperatures over time [Eitner-2010].**

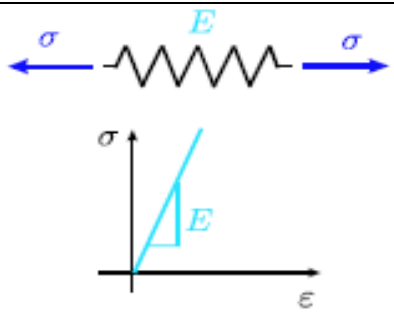
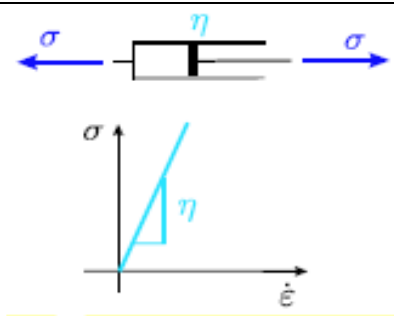
As mentioned in chapter 2, the shear modulus of the interlayer is not allowed in the static calculation by the building regulation due to the high creep behaviour of the PVB interlayer. With respect to the lower creep behaviour of an EVA interlayer compared to the PVB interlayer, it can be assumed that the shear storage modulus can be considered for the static calculation. Therefore, the thickness of the BIPV module and corresponding manufacturing costs can be reduced.

#### 4.2.2 Mechanical Models for the Interlayer

As mentioned above, the polymeric interlayers exhibit the viscoelasticity behaviour, which is the combination of viscosity and elasticity behaviour. It depends mainly on the operating temperature and load duration, respectively. Viscoelastic behaviour may be modelled by using rheological models with a spring element (Hooke's law) and damper element (Newton-element) (Figure 4-9).

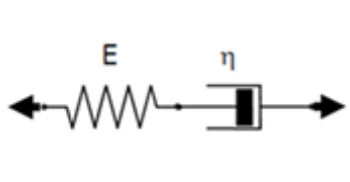
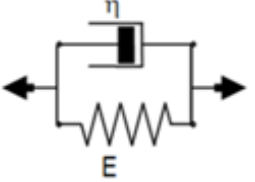
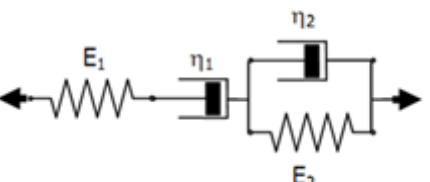
Hooke's law represents the elasticity behaviour characterized by linear proportion between stress ( $\sigma$ ) and strain ( $\epsilon$ ). Stress could also be as compression/tension stress or shear stress, which the ration of both stresses to strains are Young's modulus ( $E$ ) and shear modulus ( $G$ ), respectively. This could be estimated as a basic sample of spring.

Newton's law represents the viscosity behaviour, represented by dashpot of viscosity. It is characterized by internal resistance of fluid, so-called fluid friction ( $\eta$ ), and the deviation of flow or deformation ( $\dot{\epsilon}$ ) by either shear or tensile stress ( $\sigma$ ) (Figure 4-9).

Hook Model (Elastic)	Newton Model (Viscous)
	
$\sigma = E \times \epsilon$ $\epsilon = \sigma / E$	$\sigma = \eta \times \dot{\epsilon}$ $\epsilon = \sigma \times t / \eta$

**Figure 4-9 Rheological behaviour [Hooke element and Newton element]**

To map the rheological behaviour of polymeric interlayer, the basic elements are combined by the following series and parallel circuits. The rheological behaviour can be modelled to determine their stress or strain interactions as well as their temporal dependencies. These models include the Maxwell model, the Kelvin-Voigt model and the Burgers model (Figure 4-10) [Shen-2010].

Maxwell model	Kelvin-Voigt model	Burgers model
		
$\sigma = E \cdot \epsilon_{elas} = \eta \cdot \dot{\epsilon}_{visc}$	$\sigma = E \cdot \epsilon_{elas} + \eta \cdot \dot{\epsilon}_{visc}$	$\sigma = E_1 \cdot \epsilon_{elas,1} = \eta_1 \cdot \dot{\epsilon}_{visc,1}$ $= E_2 \cdot \epsilon_{elas,2} + \eta_2 \cdot \dot{\epsilon}_{visc,2}$

**Figure 4-10 Maxwell model, Kelvin-Voigt model and Burgers model [Wriggers-2008]**

#### Maxwell model

Maxwell model is the series combination of Hooke's law and Newton's law. For a constant applied stress, there will be an instantaneous strain and then strain will increase without bounds. If the system is unloaded, there will be an instantaneous recovery in the spring while a permanent strain remains in the damper.

### Kevin-Voigt model

Kevin-Voigt model is the parallel combination of Hooke's law and Newton's law. The Kelvin-Voigt model is also used to explain the creep behaviour of the plastic interlayer. The Kelvin-Voigt element describes the viscoelastic material with delayed elastic deformation behaviour. In creep, the strain is initially carried by the damper and is, over time, transferred to the spring and the limit on total deformation is set by the spring.

### Burgers model

Burgers model is the combination of Maxwell's and Kevin-Voigt's models. The Burgers model has four elements used to capture minimum amount of behaviour for polymeric interlayer. As shown in Figure 4-10, the individual term of Burger model's equation expresses the relevant deformational properties of the element. The first term expresses the elastic strain which appears instantaneously after loading and vanishes after the removal of the load. The second term represents the irreversible creep strain in the element once it is subjected to a constant stress. The third term expresses the delayed elastic strain which increases under the applied stress, and is recovered once the stress is removed and the element is kept unloaded for an indefinite period of time.

In summary, the Maxwell model is good for predicting stress relaxation, but poor at predicting creep, whereas the Kelvin-Voigt model is good for predicting creep but not accurate with predicting stress relaxation. The Maxwell model will be used for soft solids (materials close to the melting point), whereas the Kevin-Voigt will be used for organic polymers, rubber and wood when the load is not too high. However, both models are not appropriate to explain the behaviour of polymer material. Burgers model is good to predict the essentials of polymeric viscoelastic behaviour. Therefore, it will be used to explain the characteristics of polymers material.

### **4.2.3 Determination of the Shear Modulus of Thermoplastic**

Various attempts have been made to determine the shear modulus of thermoplastics as a function of temperature and time. Bennison, Jagota and Duser have studied the shear strength of polyvinyl-butyral (PVB) using torsion pendulum (4.5) (Figure 4-11). Using an extended eleven-parametric Maxwell model as explained earlier, they describe the time and temperature dependence (relaxation) of the shear modulus in the linear viscoelastic region [Bennison-1999]

$$G(t, T) = G_{\infty} + \sum_{j=1}^n G_j e^{\frac{-t}{\tau_j(T)}} = G_0 - \sum_{j=1}^n G_j + \sum_{j=1}^n G_j e^{\frac{-t}{\tau_j(T)}} \quad 4.5$$

- $G_0$**  Shear modulus at starting point  
 **$G_{\infty}$**  Long-term shear modulus  
 **$G_j$**  Shear modulus of the parameters of the Maxwell model  
 **$\tau_j(T)$**  Relaxation time  
 **$t$**  Duration

Sobek also studied the shear strength under the influence of temperature, strain rate, and loading time on small sized laminated safety glass. The result was a logarithmic time scale describing the time and temperature dependence of the shear modulus (4.6, 4.7) [Sobek-1998, Sobek-2000].  **$G(T, t)$**  represents the shear modulus as a function of temperature in °C ( **$T$** ) and exposure time in second ( **$t$** ). This calculation of shear modulus will be considered in mechanical models for PVB-interlayer for the module evaluation in chapter 7.

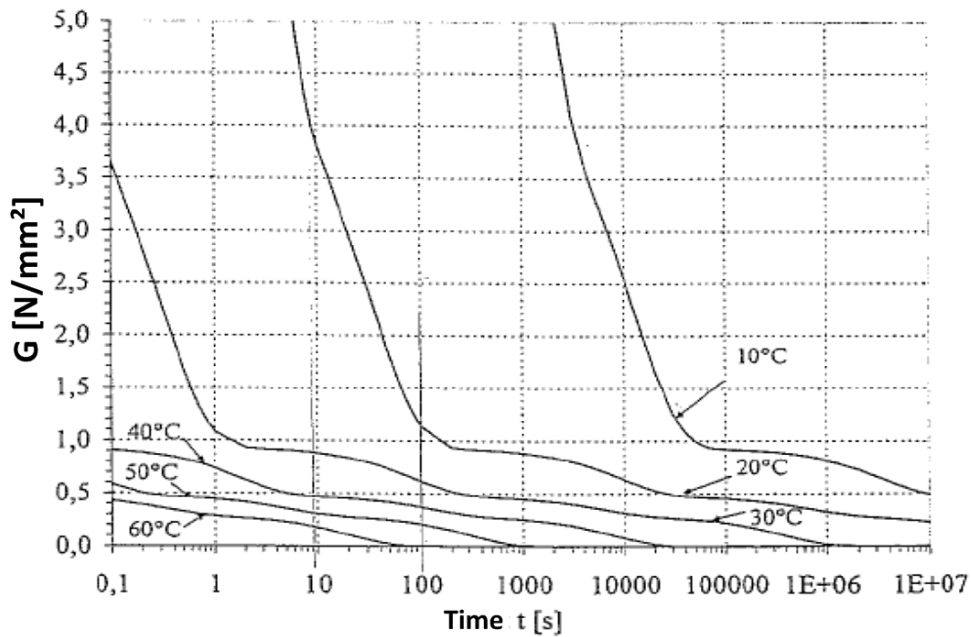


**Figure 4-11 Shear modulus curve** [Bennison, Jagota, Duser].

$$G(T > 20^{\circ}\text{C}) = 0.008 \times (100 - T) - 0.0011 \times (50 + T) \times \log(t) \quad 4.6$$

$$G(T < 10^{\circ}\text{C}) = 2.0 - 0.2 \times \log(t) \quad 4.7$$

In Figure 4-12, the shear modulus has been evaluated based on equation 4.6 and 4.7 together with validation by way of an experiment at various temperatures. It can



be stated that the shear modulus model of PVB interlayer, developed by Sobek, is matched with experimental measurement.

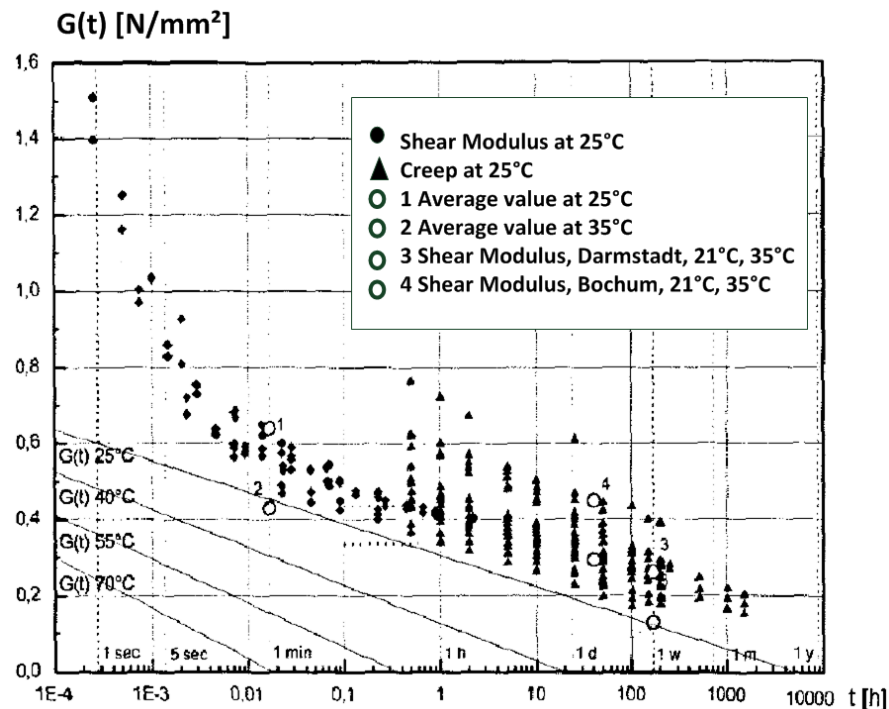


**Figure 4-12 Graph of PVB-shear stiffness modulus against load duration, based on experimental data [Sobek-2000]**

Unfortunately, no proper research on the calculation of the shear modulus based on time and load duration dependency exists for the determination of other interlayers due to numerous developments in new interlayer materials in recent years. In order to get the shear modulus characteristics of interlayers, the Dynamic Mechanical Analysis (DMA) and differential scanning calorimetry (DSC) are needed. DMA provides the thermo mechanical behaviour of the interlayer materials, whereas DSC allows the identification of the crystalline and the thermal history. It is very useful for the study of the viscoelastic behaviour of polymers. For the mechanical model validation in chapter 6 and further evaluation in chapter 7, the shear modulus of EVA in Table 4-1 is used.

Temperature (°C)	$G_{EVA}$ (N/mm <sup>2</sup> )
0	5.386
20	2.572
40	1.291
60	0.4899
80	0.35

**Table 4-1 Shear modulus of EVA [CSP-2011]**

### 4.3 Other influenced parameters

The mechanical behaviour of PV module are not only influenced by interlayer material, affected by operating temperature and load duration, but also by further parameters: load bearing material, multi-layered configurations, glass thickness, mounting system, tilt angles, etc.

Load bearing material: Load bearing material indicates the stiffness or how large the resistance to the bending of the PV modules is. Glass is the most used load bearing material in PV modules. The stiffness depends on the glass thickness, bending strength of plates and of the static system (and of bearing span). The stiffer the system, the greater the shear forces in the composite medium. Therefore, a greater degree of interconnection with a less rigid system is achieved. The more rigid the system, the lower the degree of interconnection of the plate at the same shear strength of the shear connectors.

Module structure: PV modules are mostly manufactured with 2 layers of glass, so-called PV-laminated glass. The PV laminated glass configuration is quite famous for architectural applications, especially for its incorporation into a glazed façade or roof. However, PV modules with glass-backsheet configurations also exist on the BIPV market. The front surface of PV modules is mostly glass, toughened to provide physical strength. The rear of the module can be made from a number of materials. One of the most common is Tedlar although other plastic materials can also be used. With respect to French building regulations, only the use of PV laminated glass is accepted in BIPV applications. A PV-glass-backsheet is not accepted.

Mounting system: There are numerous mounting systems available in building applications, such as the 2-sided linear frame, 4-sided linear frame, 4-fixing point, etc. Figure 4-13 describes the stress directions with regard to different mounting systems. The direction of stress is in the direction of the clamping. Moreover, the clamping depth of the mounting system is one of the most critical parameters. In Building code EN12488 and DIN 18008, the clamping depth has been defined with different requirements regarding module dimension and module thickness. However, the standard PV module cannot meet these requirements.

Inclination: Inclination is also an influencing factor, especially on snow loads. In our experimental test, only the horizontal type was needed to check the capability of the model.

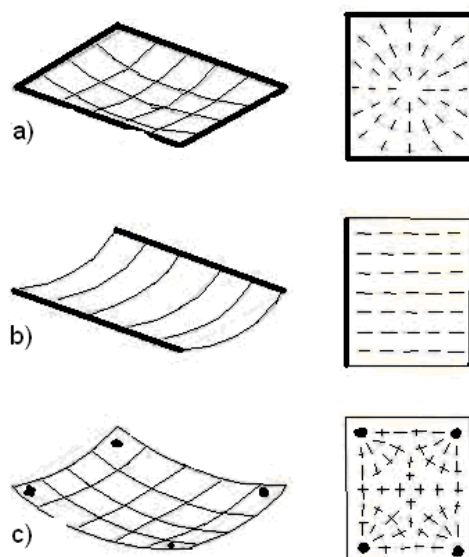


**Figure 4-13 Deformation behaviour and main stress directions of slabs supported on - a) four sides b) two sides c) four fixing points.**

#### 4.4 Legal allowance

In order to use glazing secured by linear or point-supports, no proof of structural characteristics is required if the glazing is in accordance with the technical regulations for the use of glazing with linear supports [TRLV, DIN-18008]. Table 4-2 describe the limits of bending stress and deflection of glazing in different applications of overhead or vertical glazing with corresponding mounting systems, from 2-, 3- and 4-sided clamping and various glass types, including tempered, heat strengthened, etc.

Glass types	Glazing applications	
	Overhead	Vertical
Toughened safety glass from annealed glass	50	50
Toughened safety glass from cast glass (wired, patterned glass, etc.)	37	37
Enamelled toughened safety glass from annealed glass	30	30
Annealed glass	12	18
Heat-strengthened glass	29	29
Cast glass (wired, patterned glass, etc.)	8	10
Laminated safety glass from annealed glass	15 (25*)	22,5

\*Only for back glass pane in laminated safety glass, where the breakage of front glass pane is acceptable.

**Table 4-2 Bending stress limits for various glass types in N/mm<sup>2</sup>**

Mounting	Glazing applications	
	Overhead	Vertical
4-sided	1/100 of the plate width in the direction of the main support	No requirement
3-side, 2-sided	Single glazing: 1/100 of the distinction width in the direction of the main support	1/100 of free edge
	Multi panes glazing: 1/200 of the free edge	1/100 of free edge

**Table 4-3 Deflection limits for various types of glass.**

Some essential conditions that must be followed for the installation of glazing with linear supports to TRLV are:

- The mounting or clamping depth is chosen according to PrEN 12488 and DIN 18516-4 in order to ensure the stability of the glass structure.
- The deflection of the glass pane should not exceed as defined in Table 4-3
- Under the specific load and temperature, there is no direct contact between the glass and any other rigid material (e.g. metal, glass).

## 4.5 Mechanical Modelling

The aim of mathematical modelling is to predict the mechanical behaviour of laminated glass. Critical issues are the mechanical load, operating temperature, load duration, type of multilayer laminated glass and interlayer, and mounting system.

### 4.5.1 Finite Element Modeling

With the help of the Finite Element modelling to determine bending stresses and deformation under mechanical stress, the mathematical investigation of the behaviour of PV elements was carried out using ANSYS software [Diaz-2010]. The numerical investigation of the behaviour of PV elements was carried out with the help of FE modelling (ANSYS ® 11.0 + SOLID 45), to determine bending stresses and deformations under mechanical stress.

No.	Dimension (mm)	Configuration (mm)	Load (kN/m <sup>2</sup> )
A	1200 x 1000	6-1-6	3.00
B	1200 x 1000	6-1-6	6.00
C	1200 x 1000	3-1-3	3.00

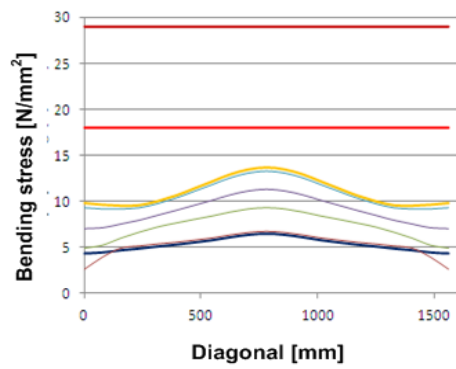
(a)

Temperature (°C)	Load duration	Shear modulus (N/mm <sup>2</sup> )
Rigidly bond	-	∞
0	1 h	94.5
20	10 sec	1.47
40	1 min	0.42
70	1 min	0.04
No bond	-	0

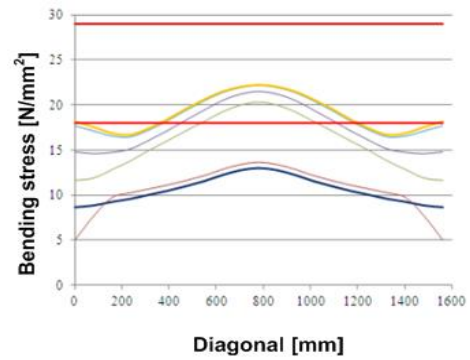
(b)

**Table 4-4 a) different module dimension with different multi-layered configuration and load scenarios**  
**b) shear modulus as a function of temperature and exposure time**

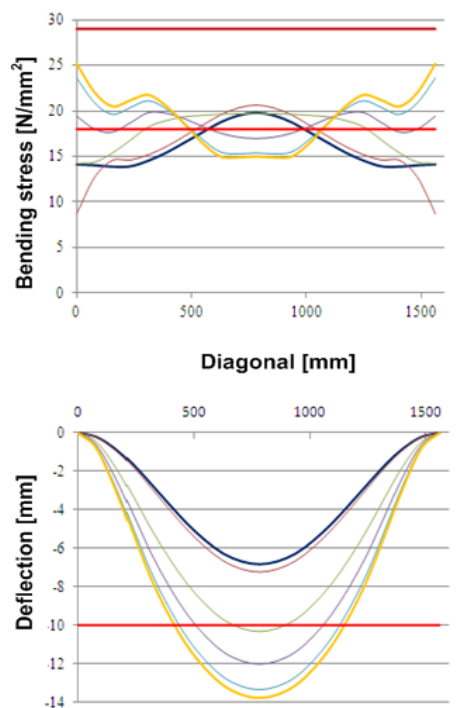
In this FE modelling, the module dimension of 1200 x 1000 mm is used with a 4-sided mounting system with different multi-layered configurations and different loads (Table 4-4a). The multi-layered configuration represents the thickness in millimetre of the front glass pane, the interlayer with a solar cell in the middle and the back glass pane. In order to evaluate the mechanical characteristic of PV laminated glass, the bonding characteristic (shear modulus) of the PVB-interlayer was considered as a function of operating temperature and load duration (Table 4-4b). The load duration under a certain load is normally longer at a lower operating temperature compared to the load duration at a higher operating temperature. In this case, the PV module at 0°C is tested with a certain load for 1 hour, while the PV module at 70°C is confronted with the same load for only 1 minute. The shear modulus in Table 4-4b can be obtained from Figure 4-11. At a higher operating temperature with a long duration, the shear modulus of the interlayer becomes lower, which reveals the weak bonding characteristics. At a low temperature with a short load duration, the shear modulus becomes higher, which reveals the strong bonding characteristics.



Scenario-1  
6-1-6 mm/ 3 kN/m<sup>2</sup>  
(a)



Scenario-2  
6-1-6 mm/ 6 kN/m<sup>2</sup>  
(b)



Scenario-3  
6-1-6 mm/ 3 kN/m<sup>2</sup>  
(c)

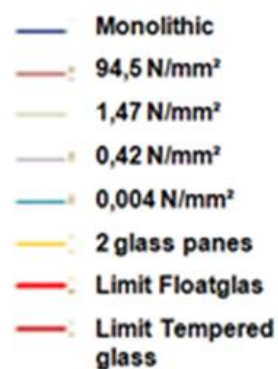


**Figure 4-14 Simulation of bending stress and deflection of the PV modules (1200x1000 mm) for PVB interlayer under different PV multi-layered configuration and load scenarios.**

Figure 4-14 exhibits the bending stress and deflection of PV laminated glass under a different multi-layered configuration and loads with a variable shear modulus. The limits of bending stress and deflection of the PV-module for monolithic glass and two glass panes without bonding have also been taken into account [EN-12488]. Both glass configurations are considered with the same thickness of laminated glass. It can be seen that the bending stress and deflection of 2 glass panes in every scenario are 2 and 4 times higher than those of monolithic glass, respectively. At the same time, the mechanical behaviour of laminated glass is between those two glasses. With a high shear modulus, the bending stress and deflection of laminated glass are quite identical to those of monolithic glass. With a low shear modulus, they are quite similar to those of 2 glass panes. Though all deflection in a different shear modulus of interlayer is still lower than the limit in scenario 2, the bending stress already exceeds the limit. Therefore, according to the building regulations, it is not allowed to build such PV modules in building applications. With a greater deflection than the limit in scenario 3, the laminated glass tries to bear the tensile and bending stress. The maximum stress is no longer in the center of the glass but on the sides, which is the so-called membrane effect (Figure 4-14).

Finite Element analysis is a well-known software with high accuracy for the consideration of an entire module area. The membrane effect can also be seen. However, this membrane effect will happen after the module deflection is higher than its thickness, which is, of course, not allowed by building regulations. Most building authorities require only maximum values of stress and displacement lower than the limitation defined in the building codes mentioned above. Moreover, it takes lots of time to do the simulation with ANSYS for different module sizes, configurations and so on.

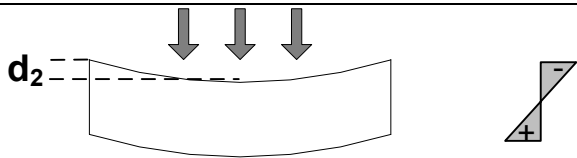
As a result, many manufacturers are now working with simple static calculations (such as glass static). At this point, the membrane effect is not taken into account because the limit has already been exceeded. Moreover, the operating temperature and load duration have not been considered in these simple static calculations. Hence, the mathematic mechanical model has to be taken into account under consideration of operating temperature and load duration.

#### **4.5.2 Mathematic Mechanical Model**

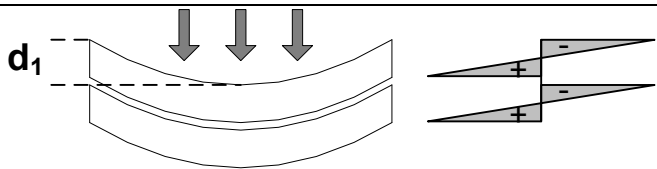
When a glass specimen is subjected to an external force, the glass responds to the applied external force by generating the stress internally. The mechanical behaviour of laminated glass plates is governed by the interlayer shear stiffness and membrane

action. To examine the complex interaction of the shear and membrane action supporting the composite effect in glass panels, a methodology based on linear elastic plate theory for multilayer glass was referred to.

For the static calculation, it is not possible to define a complete mechanical characterization on the whole photovoltaic system due to the multiple possibilities of installations. However, the module has to be dimensioned in the ways they are intended to be mounted. Table 4-5 represents the bending stress and deflection equations of monolithic glass (a), multilayer glass without lamination (b) and laminated glass (c); where  $q$  represents the external mechanical loads from EN 1991 and its own load in N/mm<sup>2</sup> [Kutterer-2005]. The parameter  $l_{min}$  and  $t_G$  are the module width and total thickness of two glass panes without bonding in mm, respectively. The elasticity of glass ( $E$ ) is around 70kN/mm<sup>2</sup>. The parameter  $\lambda$  represents the ratio of module length ( $l_{max}$ ) to module width ( $l_{min}$ ) and  $\kappa$  represents the ratio of front and back glass panes.  $\bar{h}$  represents the ratio of interlayer thickness to total thickness of two glass panes without bonding.

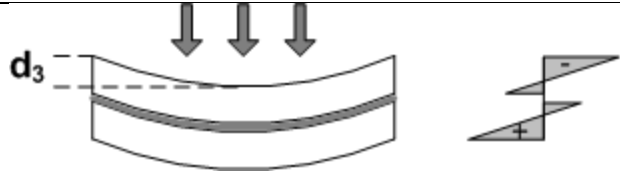
<b>Monolithic Glass</b>	
<b>Stress (N/mm<sup>2</sup>)</b>	$\sigma_{mono} = \frac{k_1 \cdot q \cdot l^2}{t_G^2}$
<b>Deflection (mm)</b>	$f_{mono} = \frac{k_2 \cdot q \cdot l^4}{E \cdot t_G^3}$

(a)

<b>Multilayer glass without bond</b>	
<b>Stress (N/mm<sup>2</sup>)</b>	$\frac{\sigma}{\sigma_{mono}} = 2$
<b>Deflection (mm)</b>	$\frac{f}{f_{mono}} = 4$

(b)



<b>Multilayer glass with bond (Laminated Glass)</b>	
<b>Stress (N/mm<sup>2</sup>)</b>	$\frac{\sigma_{lam}}{\sigma_{mono}} = \frac{4 + 4\bar{h} + \left[ 2 \times \beta_1 \times \left( 1 + \frac{1,35}{\lambda^{1,8}} \right) \times \pi^2 \right]}{\left[ \beta_1 \times \left( 1 + \frac{1,35}{\lambda^{1,8}} \right) \times \pi^2 \right] + 1 + \frac{1}{\alpha}}$
<b>Deflection (mm)</b>	$\frac{f_{lam}}{f_{mono}} = \left[ \frac{3 \cdot \kappa \cdot (1 + 2\bar{h})^2}{(1 + \kappa)^2 + 4\pi^2 \cdot \kappa \cdot \left( 1 + \frac{1,35}{\lambda^{1,8}} \right) \cdot \beta_1} + \frac{1 + \kappa^3}{(1 + \kappa)^3} \right]^{-1}$

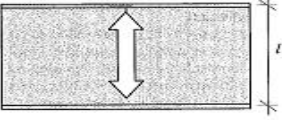
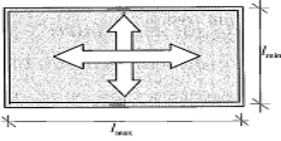
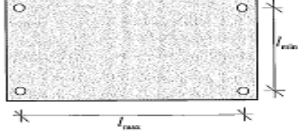
(c)

**Table 4-5 Calculation of stress and deflection for monolithic (a), multilayer glass without bond (b) together with laminated glass (c) [Kutterer-2005].**

For laminated glass, Table 4-6 represents the static calculation under consideration of bonding characteristics of interlayer (shear modulus – **G**) in shear parameter (**β<sub>1</sub>**) together with different glass configuration in stiffness parameter (**α**) [Kutterer-2005]. This bonding characteristic of interlayer (**G**) depends on a different operating temperature and load duration in different scenarios as defined in Figure 4-7 and Figure 4-8. Regarding different mounting systems (4-sided, 2-sided or 4-point), the parameters of **k<sub>1</sub>** and **k<sub>2</sub>** can be received from Table 4-7 [Widjaja-2009].

<b>Shear parameter:</b>	<b>Stiffness parameter:</b>
$\beta_1 = \frac{E}{G} \cdot \frac{\kappa \cdot \bar{h}}{(1 + \kappa)^2 \cdot \bar{l}^2}$	$\alpha = \frac{1 + \kappa^3}{3 \cdot \kappa \cdot (1 + \kappa) \cdot (1 + 2\bar{h})^2}$
where	
$\kappa = t_o/t_u$	<b>t<sub>o</sub></b> = Thickness of front glass (mm)
$\bar{h} = h/t_G$	<b>t<sub>u</sub></b> = Thickness of back glass (mm)
$\lambda = l_{max}/l_{min}$	<b>h</b> = Thickness of interlayer (mm)
$t_G = t_o + t_u$	<b>l</b> = Length of short side (mm)
$\bar{l} = l_{min}/t_G$	<b>E</b> = Elasticity of glass (N/mm <sup>2</sup> )
	<b>G</b> = Shear modulus of interlayer (N/mm <sup>2</sup> )

**Table 4-6 Parameters for shear and stiffness**

$L_{\min} / L_{\max}$	Mounting System					
	2-sided		4-sided		4-points	
						
	$k_1$	$k_2$	$k_1$	$k_2$	$k_1$	$k_2$
0.0	0.750	0.156				
0.1						
0.2			0.748	0.147		
0.3			0.725	0.142		
0.4			0.673	0.131		
0.5			0.603	0.115	0.803	0.177
0.6			0.526	0.099	0.832	0.187
0.7			0.451	0.083	0.861	0.199
0.8			0.383	0.068	0.892	0.227
0.9			0.323	0.056	0.925	0.275
1.0			0.272	0.046	0.964	0.332

**Table 4-7** Parameter  $k_1$  and  $k_2$  for different mounting systems; 2-sided clamped, 4-sided clamped, 4-point fixing [Widjaja-2009].

## **5. Experimental Infrastructures**

In order to evaluate the thermal impacts on the electrical, thermal and mechanical characteristics of BIPV applications, the power balance and mechanical models have to be validated by experimental measurements. For the power balance model, the test infrastructures were designed to probe the electrical power output or energy yields aspects as well as the architecturally relevant thermal building functions. The corresponding measurements were done based on outdoor and indoor test infrastructures. For the evaluation of the mechanical model, the test infrastructures were designed to probe the mechanical behaviour under real operating boundary conditions of BIPV applications. For this purpose, the measurements were carried out based only on indoor test infrastructures.

### **5.1 Outdoor Test Infrastructures**

In order to validate all physical mechanisms defined in chapter 3 in the power balance model, the input power will be investigated along with electrical and thermal powers. For the power input to PV system, the reflection and spectrum losses will be evaluated together with the distribution of solar irradiation based on different tilted and orientation angles. Moreover, the solar irradiation conversion models will be further evaluated from horizontal global solar irradiation to inclined solar irradiation. Meanwhile, the actual electrical power and operating temperature were measured in order to validate the electrical and thermal aspects of power balance models, respectively. The operating temperature is the most important parameter, which affects the electrical dissipation and absorption thermal power. With the good correlation of measured and simulated operating temperatures of BIPV modules in chapter 6, the thermally relevant building functions can be further evaluated in chapter 7.

#### **5.1.1 Solar Irradiation Measurement**

In order to evaluate the PV module under weak-light solar irradiation, the distribution of solar irradiation on different tilted and orientation angles can also be obtained over a year at the location Kassel (51°18'N, 09°26'E). In addition, different inclined solar irradiation conversion models in chapter 3.3.1.4 are used to calculate the solar irradiation on an inclined surface with the horizontal pyranometer measurement. In order to evaluate the reflection and spectrum losses, these conversion models will be further validated with direct measurement from different orientations of solar cell sensors. Figure 5-1 exhibits the ISET *Sensor* Global, which consists of several solar cell sensors on different tilted and orientation angles: 90°West, 90°South-West,

90°South, 90°South-East, 90°East, 30°South and 0°Horizontal. The monocrystalline solar cell type was used due to wide range of spectrum response, which can cover the spectrum response of other PV technologies.



**Figure 5-1 ISETSensor Global at Fraunhofer IWES**

### **5.1.2 Real-time Outdoor PV Module Measurement**

To validate the energy balance model, two micro-amorphous PV modules ( $\mu$ a-Si) have been installed outdoors with different multi-layered configurations: PV-laminated glass and PV-laminated glass with thermal insulation on the backside, a so-called PV-full-integrated element and determined as a BIPV module (Figure 5-2). Extruded rigid polystyrene foam, so-called XPS, has been used for the thermal insulation. The modules are installed on an open rack system with free ventilation on the backside and faced to the south at a 30° tilted angle. The PV modules were operated under MPP conditions. The electrical power was measured by an IV-tracer (ISET-MPP-Meter). At the same time, the module temperature was monitored directly behind the PV-modules. Table 5-1 describes the physical parameters of the materials used in PV- and BIPV modules, while Table 5-2 describes the PV module parameters based on the datasheet [Misara-2000].



**Figure 5-2 PV module types at Fraunhofer IWES (PV-Testlab; front and backside**

Material	Density $\rho$ (kg/m <sup>3</sup> )	Specific heat capacity $c$ (J/kgK)	Heat conductivity $\lambda$ (W/mK)	Thickness $d$ (mm)
Glass	3000	500	0,76	3,00
PV+EVA	2330	677	0,80	~1,00
XPS	33	1500	0,033	50,00

**Table 5-1 Physical parameters of material used in PV-modules.**

	Glass-Glass	Glass-Glass-XPS
Module efficiency ( $\eta_{PV}$ )	8.1%	8.1%
Module's temperature-coefficient (%/K)	0.24	0.24
PV-Transmission/ Reflection/ Absorption ( $\tau_{PV} / \gamma_{PV} / \alpha_{PV}$ )	0.01/0.00/0.99	0.01/0.00/0.99
Glass-Transmission/ Reflection/ Absorption ( $\tau_{glas} / \gamma_{glas} / \alpha_{glas}$ )	0.90/0.08/0.02	0.90/0.08/0.02
Backside-Transmission/ Reflection/ Absorption ( $\tau_{back} / \gamma_{back} / \alpha_{back}$ )	0.90/0.08/0.02	0/0/1
Area ( $A : m^2$ )	1.055	1.055
Thermal capacity ( $C_M : J/K$ )	6030	8640

**Table 5-2 module types with their specification**

For the validation, the data were measured at 15 second intervals in 2009 with Agilent 34970A data acquisition. Filtering or removing outliers or suspect data will be done through common plausibility-tools; periods with snow coverage, global irradiances  $G < 5 \text{ W/m}^2$  and zenith angles  $\theta > 85^\circ$  are not considered.

## 5.2 Indoor Test Infrastructures

In order to emulate a solar irradiation and corresponding operating temperature, the back-bias current concept has been introduced in chapter 5.2.1 instead of using the conventional climate chamber. For power balance model validation, the main propose of this concept is an emulation of solar irradiation to be complied with boundary conditions in the standard [EN-673], [EN-13332-2]. Hence, the operating temperature will vary based on each multi-layered configuration. However, the emulation of certain operating temperatures will be the main aim for the validation of the mechanical model. In this case, the solar irradiation will not be considered. This back-bias current concept will be considered as a basis concept for further test infrastructures to validate the power balance and mechanical models.

The validation of the power balance model can be obtained with the PV variable mounting equipment in chapter 5.2.2. This equipment will offer the possibilities to measure the thermally relevant building parameters: the heat transfer coefficient together with surface operating temperature on the front- and backside. This data can be measured with a heat flux plate and thermistor, respectively. With the back-bias current concept, the variation of solar irradiation can be emulated. At the same time, variable gaps behind the PV panels can be built together with variable tilted angles. This PV variable mounting equipment could provide the further information on the heat dissipation elements – radiation and convection heat transfer – for the mounting system design. For certain instances, an optimal gap behind the PV panel can be obtained.

To validate the mechanical behaviour, the mechanical testing equipment was developed in chapter 5.2.3. This mechanical strength of PV modules is evaluated through bending stress and deflections. The bending stress is directly proportional to the strain measured by the strain gauge, while the deflection could be measured with wireless deflection sensors. This equipment provides the possibilities to evaluate the influence parameters of mechanical load, operating temperature and load duration. Of course, the variable operating temperature could be obtained by using the back-bias current concept.

### 5.2.1 Back-bias Current Concept

The characteristic of PV cells can be described with an equivalent circuit of a single diode model (a current source in parallel with a single-diode) (Figure 5-3a). When exposed to light, a photo current ( $I_{ph}$ ) is generated, which is proportional to solar

radiation. However, if it is connected to an external load, one part of the photo current will flow through the diode, which is the so-called diode dark current ( $I_D$ ) [Rodrigues-2010]. In the dark, the solar cell is not an active device; it acts as a diode and produces neither current nor voltage.

By operating the PV cell as a diode, the back-bias current concept emulates the amount of long wavelength thermal power absorbed in the module from solar irradiation (Figure 5-3b). Using an external power supply to feed the current back into the module, the PV module acts like an electrical load. This back-bias current heats up the module in a dynamic state to increase the operating temperature until it reaches a steady state condition (operating temperature is constant). Therefore, the particular boundary conditions of solar irradiation can be achieved.

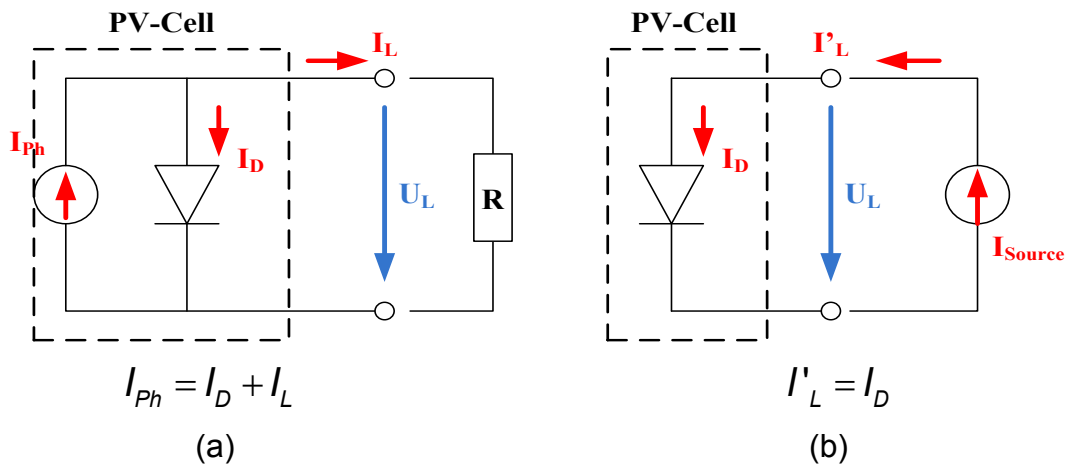


**Figure 5-3 Equivalent circuit of PV Cell characteristic under solar irradiation (a) and without solar irradiation (b).**

With respect to non-applicable conventional test methods for identifying the relevant building functions as mentioned in chapter 2, the internal heat source and the measurement of internal and external heat transfer coefficient can also be achieved with this back-bias current concept and heat flux plate measurement. In order to define the U-value, the internal heat source of the PV-module can be emulated. At the same time, the conventional measurement is not possible, as described in chapter 2.2. For the g-value, the external heat transfer coefficient can also be measured with a heat flux plate, because it has not been faced directly toward the solar irradiation.

As for the cost intensive standard-conform testing of the mechanical behaviour of the BIPV module, the back-bias current concepts can emulate a certain operating temperature, replacing the climate chamber.

### Emulation of solar irradiation

Since there are 3 different solar irradiation values defined in building codes and the PV standard, the solar irradiation of 300, 500 and 800 W/m<sup>2</sup> needs to be emulated with the back-bias current concept. The solar irradiation of 800 W/m<sup>2</sup> can be found under Standard Operating Condition (SOC). In order to emulate the long wavelength thermal power, the amount of back-bias current can be calculated from the power balance model (5.1).

$$G_{irradiation} = P_{thermal} + P_{electrical} + P_{transmission+reflection} \quad 5.1$$

With respect to the specification of the PV module, the amount of feed-in thermal power needs to be calculated along with the PV module's dimensions. In the experiment, a polycrystalline PV module was used in a glass-glass module configuration (Table 5-3). The energetic components in the form of reflection together with transmission and the photovoltaic conversion were calculated using the technical data of the module. In order to compare the behaviour of the PV modules together with conventional glass, the amount of back-bias current was calculated together with the PV module dimension of 0.5 m<sup>2</sup> (Table 5-4). With a high transmission of conventional glazing and module dimension of 0.5 m<sup>2</sup>, the back-bias currents for solar irradiation of 300W/m<sup>2</sup> and 500W/m<sup>2</sup> are 20W and 33W, respectively. For a PV-Cell with high absorption, the back-bias current for a solar irradiation of 300W/m<sup>2</sup>, 500W/m<sup>2</sup> and 800 W/m<sup>2</sup> are 111W, 185W and 395W, respectively.

Description	Conv. Glass	PV Module
Module efficiency ( $\eta$ ) <i>PV</i>	0%	10%
Transmission/Reflection/Absorption	79%, 8%, 13%	8%, 8%, 84%
Module configuration	Glass-Glass	Glass-Glass
Number of PV solar cells	-	40
Cell technology	-	polycrystalline
Dimension	450x1070 mm.	450x1070 mm.

**Table 5-3 PV-Module characteristics**



Scenarios			G		P <sub>electric</sub>		Reflexion + Transmission		P <sub>thermal</sub>	Back-bias current
1	Glass-300		300 W	-	0 W (0%·300 W)	-	261 W ((8%+79%)·300 W)	=	39 W	20 W
2	Glass-500		500 W	-	0 W (0%·500 W)	-	435 W ((8%+79%)·500 W)	=	65 W	33 W
3	PV-300		300 W	-	30 W (10%·300 W)	-	48 W ((8%+8%)·300 W)	=	222 W	111 W
4	PV-500		500 W	-	50 W (10%·500 W)	-	80 W ((8%+8%)·500 W)	=	370 W	185 W
5	PV-800		800 W	-	80 W (10%·800 W)	-	128 W ((8%+8%)·800 W)	=	592 W	395 W

**Table 5-4 Feed-in thermal power with different solar irradiation from conventional glazing and PV Modules**

The corresponding voltage and current of back-bias current concept depend on the individual module parameter of open circuit voltage ( $V_{oc}$ ). The fed-in voltage is slightly over the open circuit voltage ( $V_{oc}$ ), where the fed-in current is variable. For instance: for 111W of back-bias current, the fed-in current and voltage are 3.5 A and 31.7V, respectively. At the same time, for 185W of back-bias current, the fed-in current and voltage are 5,8A and 31,9V, respectively.

### 5.2.2 PV Variable Mounting Equipment

The steady state is considered for identifying the relevant building function. The long wavelength thermal power is balanced with dissipation thermal power, while the thermal absorption power is no longer available, as described in chapter 3.3 on power balance concept. In order to validate the dissipation thermal power in the power balance model, the PV variable mounting equipment was developed due to wide range installations of BIPV applications. Table 5-5 describes the variable possibilities in this equipment.

Variable possibilities	Description
different multi-layered configurations	free ventilation, variable gap behind the PV modules (5cm, 10cm) and full-integrated modules.
different tilted angles	vertical to horizontal

**Table 5-5 Variable possibilities in PV variable mounting equipment; multi-layered configuration and tilted angles**

With this equipment, the standard PV and BIPV applications can be built: free-standing system, roof-top with variable ventilation and PV full-integrated building elements. Moreover, the standard-conform solar irradiation or corresponding operating cell temperature can also be obtained with the back-bias current concept.

All measurements were performed in a darkened room to avoid the PV generated current in the opposite direction due to external light, which leads to non-constant back-bias current for the emulation of solar irradiation. To measure the thermal behaviour of BIPV modules, the heat flux plate and thermistor had to be employed (Figure 5-4a, b). With respect to the high complexity of natural convection compared to forced convection, moreover, all measurements were performed in a closed room. In order to classify the influence of external wind, the wind sensors (FVA645-TH2) had also been installed over the measured surface (Figure 5-4c). All measurements above are monitored with data acquisition ALMEMO 2290-8 with time interval of 30-sec.

#### Heat flux plate

The power dissipation via radiation and convection heat transfer of PV module could be measured with heat flux plate. It measures the heat flux densities [ $\text{W/m}^2$ ]. However, it does not provide an exact heat flux density, but only a direct voltage signal. Together with calibration values, the heat flux density can be measured. Regarding product specific requirements of the heat flux plate, the influences of direct sunlight and moisture have to be avoided.

#### Thermistor

To measure the surface and surrounding temperatures, the thermistor sensor, Pt100, class B was used. The thermistor increases its resistance when the temperature increases. The temperature measured can be looked up in the adjusted resistance table of the thermistor. The temperature can be directly measured via the fed-in voltage drop across the resistance.

#### Wind sensor

The wind sensor acts like a hot-film anemometer, which is operated under feed-in current. If wind flows through the sensors, the feed-in needs to be increased to heat up this thin film anemometer. This amount of feed-in current could be converted into wind speed via data acquisition above.

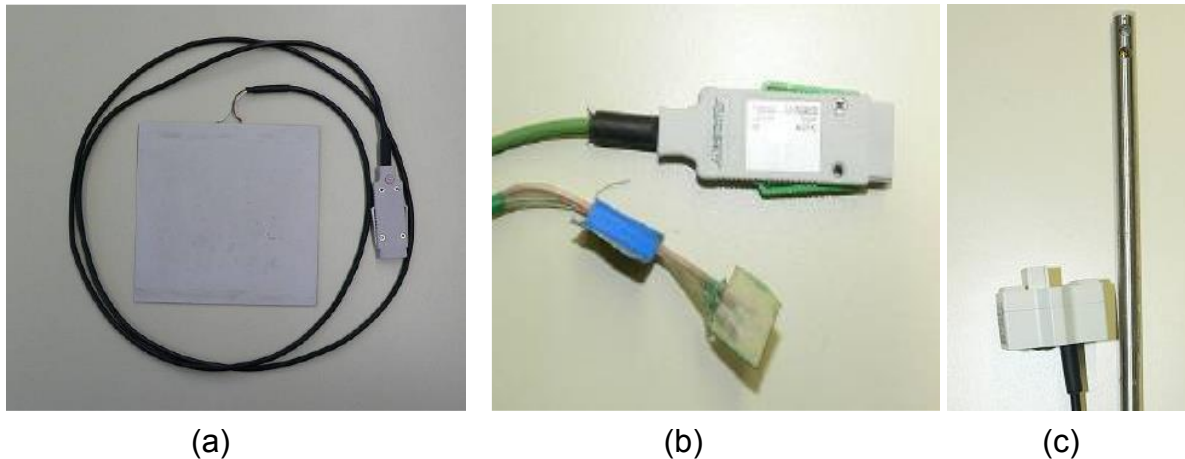


**Figure 5-4 Heat flux plate (a), thermistor (b) and wind sensor (c)**

#### Schematic of measurement

After measuring the heat flux together with the surface and surrounding temperatures, the heat transfer coefficient can be calculated. Figure 5-5 describes the schematic of the measurement above. The measurement is done on the front- and backside in order to evaluate the heat dissipation at different tilted angles.

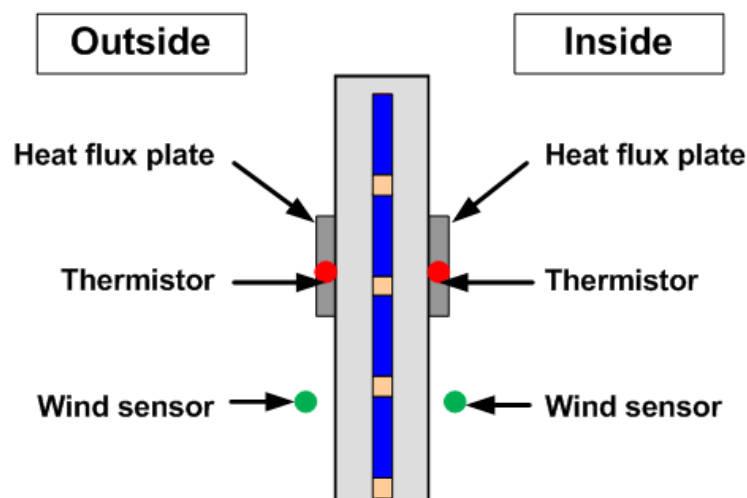


**Figure 5-5 Schematic of heat flux measurement together with surface and surrounding temperature measurement and wind sensor on both outside and inside**

The internal and external heat transfer coefficient ( $h_i$  and  $h_e$ ) are proportional to the measured heat flux from heat flux plates ( $q_i$  und  $q_e$ ) to temperature differences between the operating module temperature ( $T_M$ ) and the ambient temperature ( $T_{amb}$ ) (5.2). Regarding the heat flux plate's specification, the temperature difference between the surface and surrounding temperature needs to be higher than  $5^\circ\text{K}$ . These internal and external heat transfer coefficients represent both convection and radiation heat transfer. Since the test was done under indoor conditions with low

external wind speed behind the PV panel, natural convection was a major component of the convection heat transfer compared to forced convection.

$$\frac{1}{h_{i,e}} = \frac{T_{M-i,e} - T_{amb-i,e}}{q_{i,e}} \quad 5.2$$

### Test bench

For the validation of the dissipation thermal power, the PV-laminated glass was employed with polycrystalline PV technology. The PV module parameters can be found in Table 5-3. Figure 5-6a exhibits the test bench of PV module together with an external power supply for feeding the power back to the PV-module.

Figure 5-7 describes the different testing configurations of ventilation systems: free-standing, variable gaps from 5cm and 10 cm together with full-integrated of PV module. For variable gaps and PV full-integrated configurations, 10 cm of extruded rigid polystyrene foam (XPS) were used for the thermal insulation with a heat conductivity of 0.033 W/m<sup>2</sup>K. For this test bench, variable tilted angles could also be employed from horizontal to vertical tilted angles.

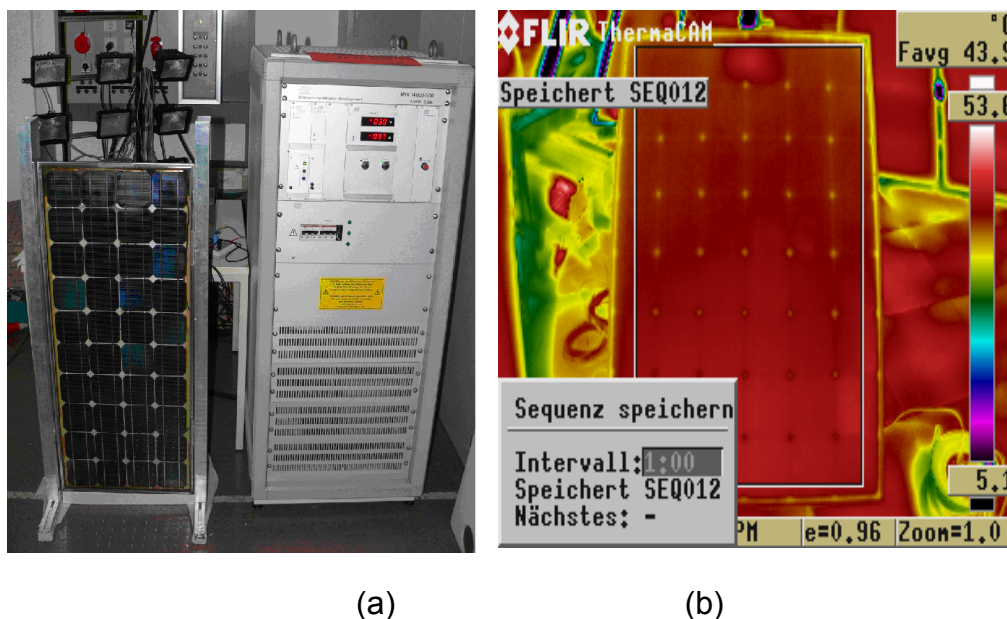


**Figure 5-6 (a) Test infrastructure of feed-in thermal power with polycrystalline PV module and external power supply**  
**(b) Experimental measurement with Infrared (IR) Camera**

### Position of sensors

With respect to experimental measurement with an Infrared (IR) Camera, the module operating temperature is quite similar over the module surface (Figure 5-6b). Therefore, the thermistor sensors and heat flux plates were placed centrally on the front- and backside of the PV module (

Figure 5-7) [Sidelev-2011].

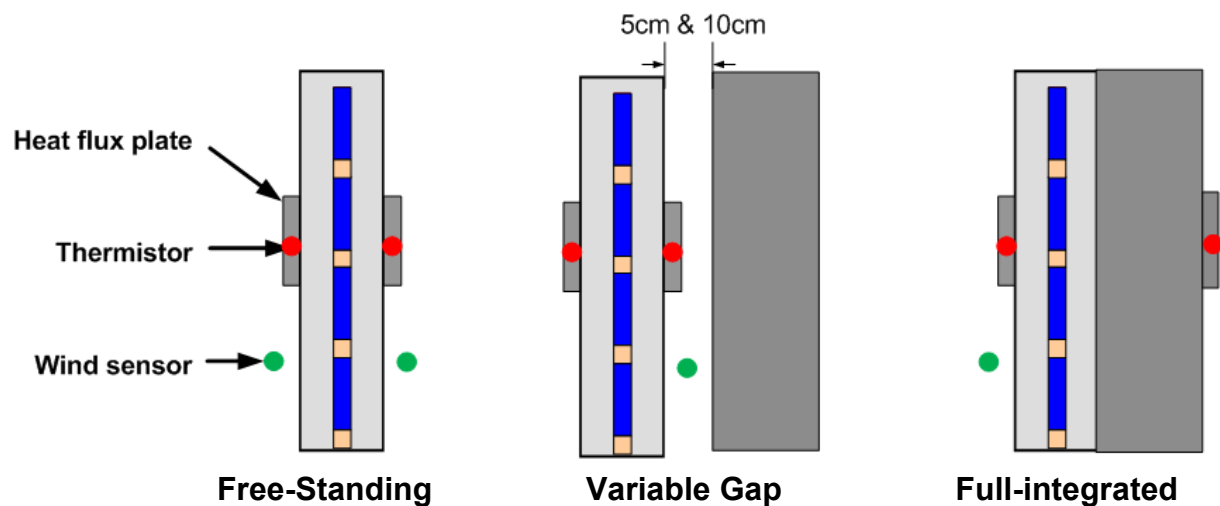


**Figure 5-7** Test bench with different ventilation system configuration; free-standing variable gaps and full-integrated configurations.

### 5.2.3 Mechanical testing equipment

For the validation of the mechanical model, the mechanical testing equipment was developed in order to measure the bending stress and deflection based on different boundary conditions, e.g., mechanical load, operating temperature, load duration, mounting system, multi-layered configuration and etc. These are parameters that influence the mechanical behaviour of BIPV modules. Table 5-6 describes the variable parameters in mechanical testing equipment.

Variable parameters	Description
Operating temperature	20°C, 40°C and 60°C
Load duration	20 minutes and 1 hours
Mounting system	2-sided standard conform and 4-sided manufacture specific
Multi-layered configuration	PV-laminated glass and PV-glass-backsheet

**Table 5-6** Variable parameters in mechanical testing equipment

To measure the mechanical behaviour at different operating temperatures, the back-bias current concept was employed, instead of the cost-intensive climate chamber. The creep characteristics of interlayers used can be measured with a different load duration. In terms of the mounting system, the main difference between a standard-

conform and manufacturer specific mounting system is the clamping depth. The standard-conform clamping depth was defined based on module dimension and – thickness [EN12488], while most of manufacture specific mounting system is much less than the standard-conform clamping depth. In order to validate the mechanical models, the different mounting systems have to be taken into account. With respect to the different multi-layered configurations from glass to backsheet substrates, the surface of each substrate is investigated in order to prove the applicability of the mechanical test equipment and corresponding measurements. As for the outcome of the indoor measurement, the implementation of the measurement in real outdoor measurement is another objective used to measure the mechanical behaviour of BIPV modules under real climatic conditions.

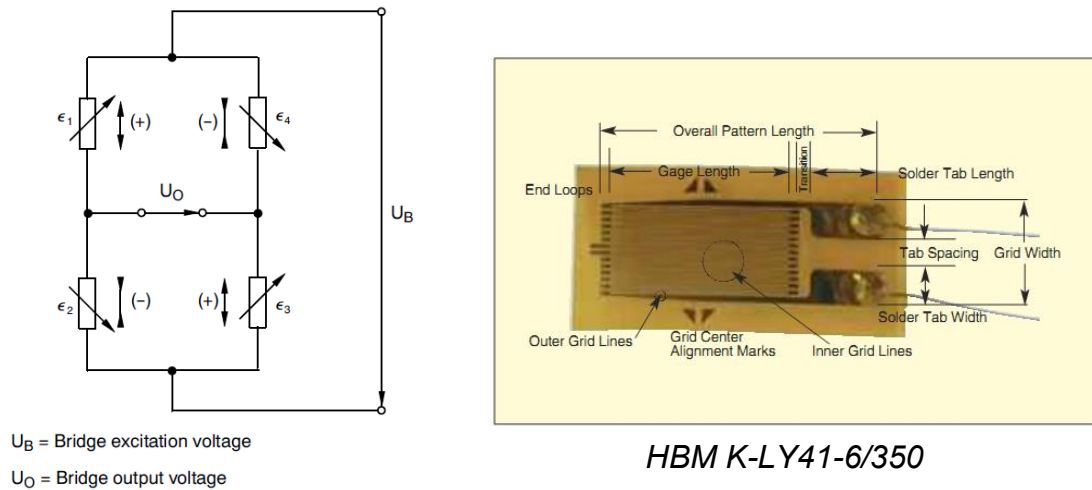
The bending stress and deflection of the BIPV module are the most important parameters for the evaluation of mechanical behaviour of the BIPV module. These parameters have to be within the limits defined in building regulations [DIN18008]. To measure the bending stress and deflection, the strain gauge and displacement sensor are needed.

### Strain gauge

A strain gauge is a device used to measure the strain of an object. The bending stress can be further calculated after multiplying it with elasticity of glass, so-called Young modulus ( $E$ ). It is attached directly to the surface of the object. As the object is deformed, the gauge is deformed and causes the resistance to change. However, this change is quite low, in the  $\mu\Omega$  range. Moreover, the resistance change of the strain gauge is quite sensitive to the object temperature with the corresponding material's elongation, the strain gauge temperature itself, resistance in cable, etc. In order to compensate for all influences mentioned above and increase the measurement signal, a Wheatstone bridge is normally employed together with voltage supply (Figure 5-8a) [HBM-2008]. To obtain the strain, the Wheatstone bridge, full-, half or quarter bridges could be used depending on different compensation as stated above.

In mechanical test equipment, the K-series of the strain gauge is used together with a gauge resistance of  $350\Omega$  with a strain gauge factor (K-factor) of 2.07 (Figure 5-8b). Unfortunately, there is no glass specific gauge type for measuring on a glass surface. Therefore, the steel-specific gauge type is used. Of course, the material compensation from steel to glass has to be considered together with operating temperature compensation. With respect to the short cable length with low cable resistance and available temperature compensation of material and the strain gauge

itself, the strain gauge can be measured directly with high resolution data acquisition, Agilent 34970A. This data acquisition can measure the resistance changes in the  $\mu\Omega$  range. The Wheatstone bridge is, therefore, not necessary.



$$\frac{U_O}{U_B} = \frac{k}{4} \cdot (\epsilon_1 - \epsilon_2 + \epsilon_3 - \epsilon_4)$$

**Figure 5-8 a) Wheatstone bridge connection together with strain calculation  
b) Strain gauge type HBM K-LY41-6/350**

To achieve high accuracy, the strain gauge has to be installed at the position where maximum strain occurs. In addition, the direction of the strain gauge has to be installed in the direction of the bending strain, as defined in Figure 4-13.

### Displacement sensor

In order to measure the deflection of the PV module, the contactless displacement sensor is used based on an ultrasonic concept. The sensor is installed below the PV module at the middle of PV-module, where maximum deflection occurs. This ultrasonic sensor emits short, high-frequency sound pulses at regular intervals. These propagate in the air at the velocity of sound. If they strike an object, then they are reflected back as echo signals to the sensor, which then computes the distance to the target based on the time-span between emitting the signal and receiving the echo [Ultrasonic-2011]. Figure 5-9 describes the specification of the displacement sensor. With respect to the operating input voltage, the measured distance will be directly proportional to the output voltage plus the blind zone of the sensor. For instance; input voltage is 10V. The blind zone of the sensor is 30mm, while the operating range is 250mm. If the output voltage can be measured at 7V, the measured distance will be  $[(7/10) \times (250-30)] + 30 = 184$  mm.

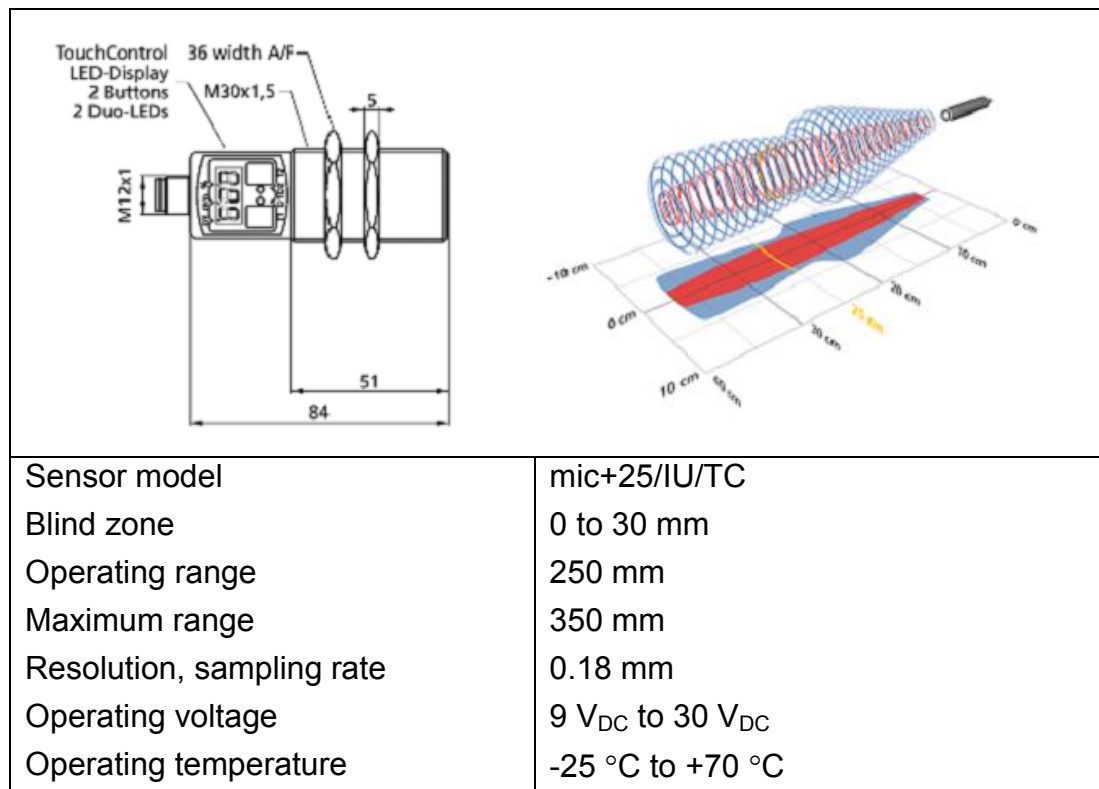


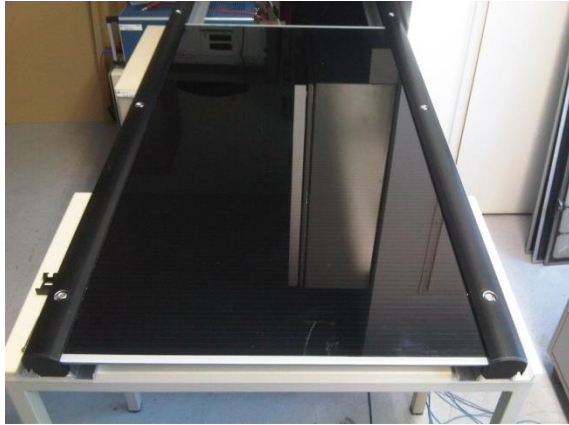
**Figure 5-9 Displacement sensor with product specification**

### Test Bench

The mechanical testing equipment was used indoors for the mechanical model verification together with the approval of the functions of the measuring device and the device connection. Below there are the 3 module types with their corresponding module mounting systems:

- Module 1 thin film module with  $t_G = 7.2$  mm, glass-glass configuration  
dimension 600 x 1200 mm, standard conform clamping depth  
Load  $q = 8.43 \times 10^{-3}$  N/mm<sup>2</sup>
- Module 2 crystalline module with  $t_G = 4.8$  mm, glass-glass configuration  
dimension 450 x 1070 mm, manufacture specific clamping  
 $q = 8.63 \times 10^{-3}$  N/mm<sup>2</sup>
- Module 3 crystalline module with  $t_G = 4.8$  mm, glass-backsheet configuration,  
dimension 460 x 995 mm, manufacture specific clamping dept  
 $q = 3.84 \times 10^{-3}$  N/mm<sup>2</sup>





(a)



(b)

**Figure 5-10 Mechanical testing equipment with implementation of displacement sensor**

The calculation of all providing loads was based on the permitted range of glass together with safety factors in order to avoid any breakage of the PV modules. Figure 5-10 exhibits the test bench with 2-sided standard-conform clamping depth (a) and the displacement sensors below the PV modules (b).

## 6. Validation

In order to investigate the thermal influences on the BIPV applications, the operating temperature is the most important parameter to be investigated due to its direct influences on electrical, thermal and mechanical behaviour. In temperature models, the solar irradiation as power input, electrical power and dissipation power can be validated with solar irradiation measurement (5.1.1), real-time outdoor PV module measurement (5.1.2) and PV variable mounting equipment (5.2.2) with back-bias current concept (5.2.1), respectively. In mechanical model, the bending stress and deflection can be validated with mechanical testing equipment with back-bias current concept.

As power input of the system, the solar irradiation is the main reason the PV module attains a higher operating temperature, thereby leading to further changes in electrical, thermal and mechanical characteristics. The solar irradiation as a power input on the BIPV module will be evaluated with solar irradiation measurements: pyranometer and solar cell sensors. The main focuses of this evaluation will be on solar distribution, particularly on the weak-light range, and reflection as well as spectrum losses together with the inclined solar irradiation conversion models.

Secondly, the dissipation power will be investigated with PV variable mounting equipment together with the back-bias current concept. This will provide the basis for a further evaluation of real-time electrical characteristics together with real-time and steady state thermal characteristics. The real-time thermal characteristics will be useful for building simulation to generate the real-time thermal load profile of the building, while the steady-state thermal characteristics will be useful for the evaluation of relevant building functions of BIPV module in building design applications; for instance: U- and g-values.

With the outcomes of power input and real-time thermal characteristics, the real-time electrical characteristics will be validated using real-time outdoor PV module measurement. The real time electrical characteristics will be useful for grid-integration and self-consumption approaches, as described in 2.1.

Finally, with respect to different operating temperatures and variable installation possibilities and locations, the mechanical characteristics will be validated with mechanical testing equipment. This mechanical strength of BIPV modules will be useful for the PV module manufacturer in the module design phase to fulfil the requirements of building regulations and standards.

## 6.1 Solar irradiation

With solar irradiation measurements on pyranometer and solar cell sensors at different orientations, firstly, the inclined solar irradiation conversion models (3.3.1.4) can be evaluated together with spectrum and reflection losses (3.3.1.2, 3.3.1.3) at PV modules. Moreover, the distribution of solar irradiation is also investigated based on different orientations.

### 6.1.1 Inclined Solar Irradiation Conversion Models

For the PV output, the reflection loss is influenced by the angle of incident ( $\theta_{in}$ ), while the spectrum loss is influenced by the zenith angle ( $\theta_z$ ) and corresponding air mass value, as mentioned in chapter 3. In order to evaluate these losses, the angles mentioned above have to be investigated based on different tilted and azimuth angles. The solar irradiation measurement at different tilted angles is needed to evaluate the reflection and spectrum losses. However, there are no pyranometers available at all different tilted angles. By means of horizontal solar irradiation measurement from the pyranometer, therefore, the inclined solar irradiation can be calculated based on 4 conversion models: Jordan, Klucher, Reindl and Hay (Table 3-7). These conversion models will be further validated with direct measurement of solar cell sensors. In order to evaluate the conversion models, the relative Means Bias Deviation (rel.MBD) and relative Root Means Square Deviation (rel.RMSD) methods will be considered. MBD method gives information on a general offset of the model results over a time, which is useful for yearly energy yields prediction for an economic point of view, while RMSD methods provides additional information on the general scatter of modelled versus measured data. In this work, the polarization and dispersion of spectrum distribution is not taken into account. Figure 6-1 represents the changing ranges of angle of incident ( $\theta_{in}$ ) and zenith angle ( $\theta_z$ ) together with the monthly deviation of different conversion models at different orientations at location Kassel (51°18'N, 09°26'E).

The zenith angles ( $\theta_z$ ) and corresponding air mass values are changing during a day in the same range for all orientations, because the zenith angles represent the distance for sunlight to travel through the atmosphere to the PV module compared to that at a perpendicular angle to the Earth. In the course of one day, the zenith angle varies from 90° to around 30° in summer and from 90° to around 75° in winter. However, the angles of incident ( $\theta_{in}$ ) are changing during a day in different ranges for different orientations. For instance: the variation of the ( $\theta_{in}$ ) during a day in summer is

from 90° to 60° and from for 90° to 0° for the PV modules at 90° and 30° tilt angles facing to the south.

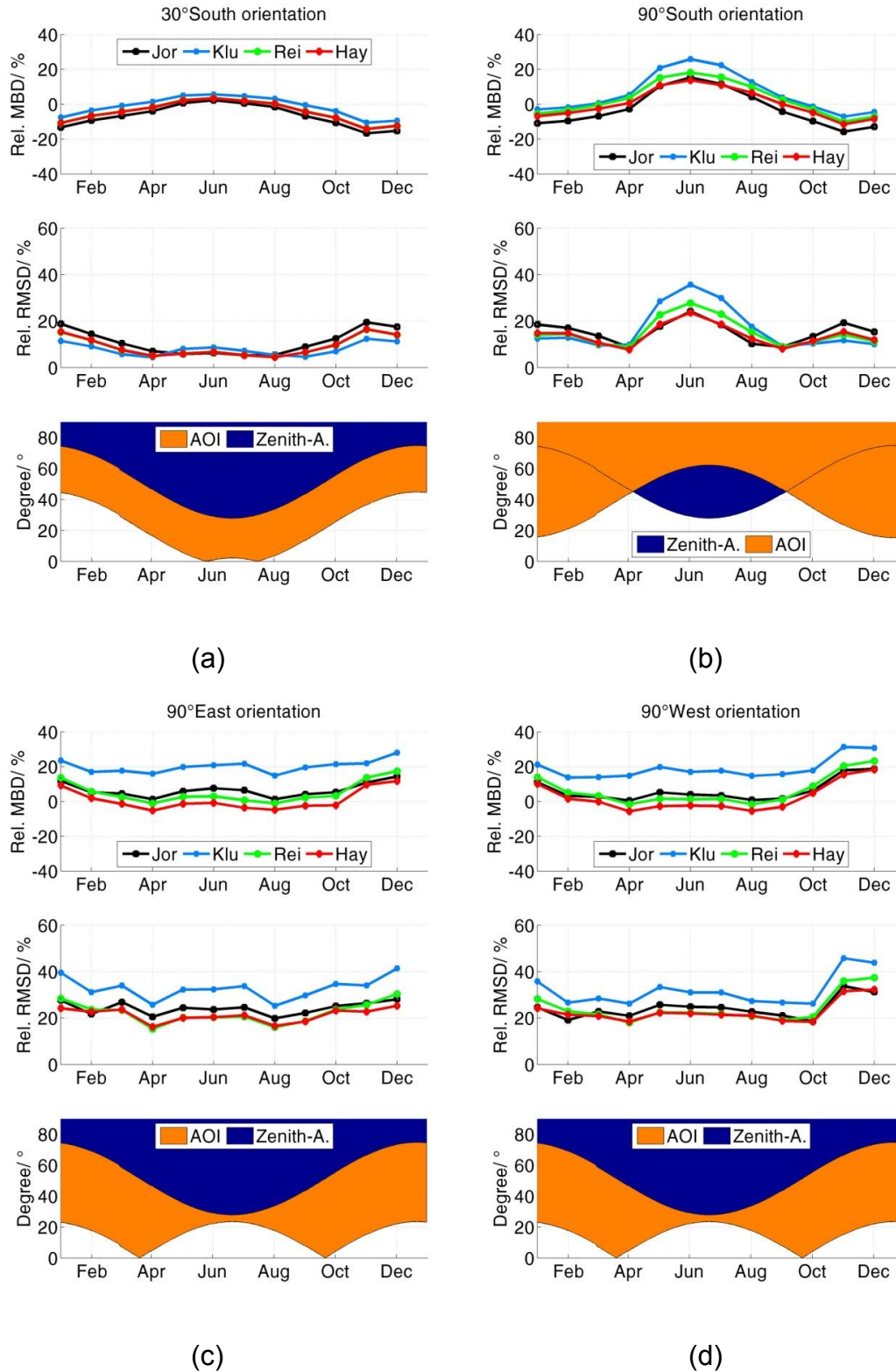


**Figure 6-1** Deviation of solar irradiation between conversion models and measured data in MBD and RMSD methods together with variation of angle of incident ( $\theta_{in}$ ) and zenith angles ( $\theta_z$ ) for 30°-South (a), 90°-South (b), 90°-East (c) and 90°-West (d) orientations.

For the orientation of 30°-South, the deviations between the conversion models to measured data are relatively small during the summer months due to the small values of the angle of incidence and air mass, which means low reflection and spectrum losses. During the winter months, the deviation values as well as both angles increase, which leads to higher reflection and spectrum losses (Figure 6-1a). These losses are complementary to each other. For an orientation of 90°-South, maximum deviations occur in the summer period. At this time, high angle of incidences but low zenith angles and corresponding air mass values are present. Therefore, with a high angle of incident alone, the calculated values are higher than the measured data. However, a slight increase in the deviation is also observed due to the higher air mass values (Figure 6-1b) in winter months. Hence, the angle of incidence seems to be the major factor for the accuracy. For the orientations of 90°-East and 90°-West, the distribution of the angle of incidence is quite small throughout the whole year. Consequently, the deviations are relatively uniform. However, the deviations get slightly larger due to higher zenith angles and air mass values (Figure 6-1c, d) in the winter period.

With respect to the validation presented, it can be stated that the Hay model has proven most appropriate. To evaluate the operating temperature and power output in the following works, the applied models seem to be less accurate under these conditions. Therefore, the direct measurement by solar cell sensors will be used as the power input of the PV modules. As power input to PV module, however, the solar irradiation from a pyranometer and inclined solar irradiation conversion models can still be used in this developed models.

### 6.1.2 Distribution of Solar Irradiation

With respect to the reduction of the PV module efficiency in the weak-light range of solar irradiation due to shunt resistance inside the modules, as defined in Chapter 3.3.2 [Grunow-2004], the distribution of solar irradiation will be evaluated based on weighting factors as defined in the PV-inverters standard [EN 50530]. This distribution will be useful to predict the energy yield of a PV module together with the Energy-Rating standard [EN 61853]. In order to avoid any spectrum and reflection losses, the solar cell sensors will be considered instead of pyranometer. This evaluation will be done based on different orientations.

Figure 6-2 describes the weighting factors of different tilted and azimuth angles together with those of the new- $\eta_{Euro}$  defined in EN50530. It can be observed that for all orientations with a tilt angle of 90°, solar irradiance in the range of  $G=1000 \text{ W/m}^2$ ,

> 875 W/m<sup>2</sup>, is almost insignificant. But irradiances lower than the range of G=500 W/m<sup>2</sup>, from 375 to 625 W/m<sup>2</sup>, are much more frequent. Table 6-1 shows that the solar irradiation distribution especially on weak-light range has been increased from 23% based on European Efficiency (EN50530) to 47% for BIPV application at 90° tilt angle for east and west orientation (Misara-2010b).

With respect to a higher weighting factor of solar irradiation in the weak-light range at other orientations compared to those at a 30°-South orientation, therefore, the reduction of module efficiency in the weak-light range has to be properly taken into account. The Energy Rating standard (EN-61853) could be used to identify the module efficiency under different solar irradiation.

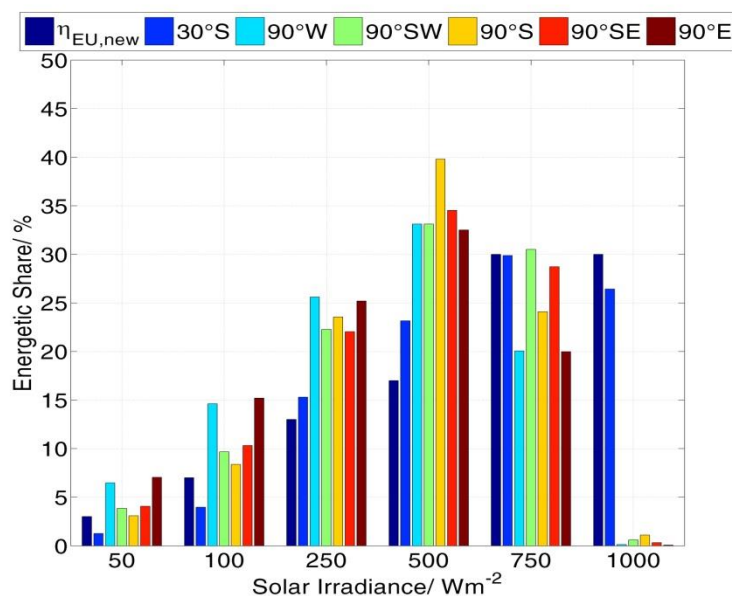


**Figure 6-2 Weighting factors of solar irradiation at different orientations compared to weighting factor at  $\eta_{EU,new}$  obtained by in EN 50530**

Orientation	Weighting factor in weak-light range (%)				
	5%	10%	25%	Total	Normalized
	0 - 75W	75 – 175 W	175 – 375 W	Weak-light	
<b>new-<math>\eta_{Euro}</math></b>	<b>3.00</b>	<b>7.00</b>	<b>13.00</b>	<b>23.00</b>	<b>1.00</b>
0°-Horizontal	1.31	5.18	20.14	26.64	1.16
30°-South	1.26	3.96	15.30	20.52	0.89
90°-West	6.47	14.61	25.62	46.70	2.03
90°South	3.08	8.37	23.55	35.00	1.52
90°-East	7.04	15.20	25.19	47.44	2.06

**Table 6-1 Weighting factors of different orientations and the  $\eta_{EU,new}$  in weak-light range, from 0 – 375 W/m<sup>2</sup>**

## 6.2 Thermal dissipation

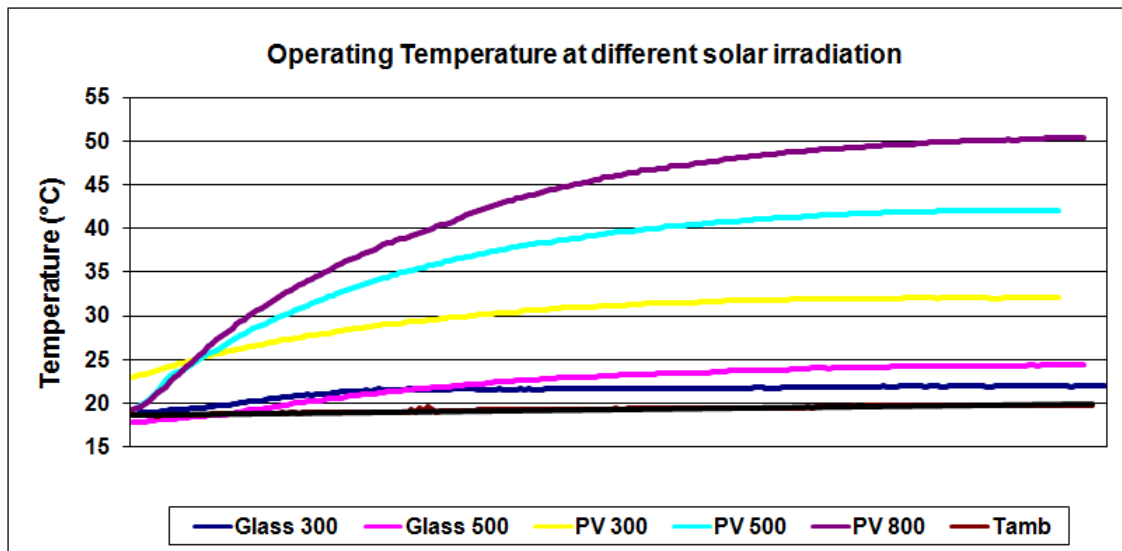
The convection and radiation heat transfer coefficients are the most critical parameters for the thermal power dissipation. With respect to the heat flux measurement in PV variable mounting equipment (5.2.2), however, only the total heat transfer can be measured, and not the individual natural and forced convection together with radiation heat transfers. Therefore, the validation of the heat transfer coefficient will be evaluated on total heat transfer coefficients. With the PV variable mounting equipment, the different operating temperatures, module tilt angles and gaps behind the PV panels were validated. In the experiment, a glass-glass polycrystalline PV module of 0.5 m<sup>2</sup> module area was used.

### 6.2.1 Variable Operating Temperatures

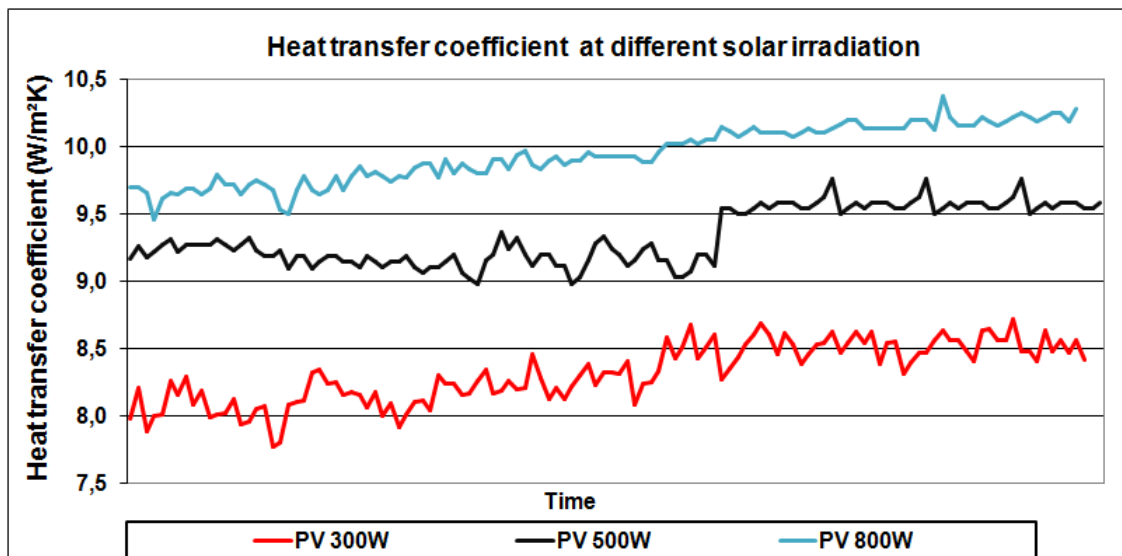
The variable operating temperature could be obtained with the back-bias current concept. In the experiment, the PV module was tested in a vertical installation without a gap behind the PV modules. The amount of back-bias current was calculated based on individual emulation of solar irradiation, as mentioned in Table 5-4 in chapter 5.

Figure 6-3 represents the surface temperature (a) and heat transfer coefficient (b) of the PV module under different scenarios. In the case of conventional glazing, the surface temperatures under solar irradiation of 300 W/m<sup>2</sup> and 500 W/m<sup>2</sup> are 22.0 and 24.5 °C respectively. The differences are only 2-4 °C above ambient temperature. However, the surface temperatures of PV modules are 32°C, 42°C and 50°C under a solar irradiation of 300W/m<sup>2</sup>, 500W/m<sup>2</sup> and 800W/m<sup>2</sup>. These represent the temperature differences between the surface temperature and ambient temperature of 12°C, 22°C and 30°C, respectively.

With respect to a higher operating temperature and corresponding surface temperature, therefore, the heat transfer coefficients will change compared to the standard values. Regarding a heat flux plate's specification, the temperature difference needs to be higher than 5°C. For conventional glazing, therefore, the heat transfer coefficient could not be measured due to lower temperature differences between surface temperature and ambient temperature (2°C and 4°C). As for the PV modules, the heat transfer coefficients of different PV module scenarios are 8.5 W/m<sup>2</sup>K, 9.5 W/m<sup>2</sup>K and 10.25 W/m<sup>2</sup>K under solar irradiation 300 W/m<sup>2</sup>, 500 W/m<sup>2</sup> and 800 W/m<sup>2</sup>, respectively. These values are much higher than standard values.



(a)



(b)

**Figure 6-3 (a) operating temperature of conventional glass and PV Module with different solar irradiation, (b) heat transfer coefficient of PV module with different solar irradianations**

Table 6-2 shows the heat transfer coefficient of different scenarios of conventional glazing and PV modules based on different approaches: EN-410, EN-6946, temperature model and measurement. The normative values of conventional glazing (EN-410), without any consideration of a higher operating surface, are not applicable for PV modules. Although EN-6946 has defined the heat transfer coefficient as a function of operating temperature, these normative values are still not applicable for PV modules.



Scenarios		Module Temperature	Heat Transfer Coefficiency (W/m <sup>2</sup> K)			
			EN410	ISO 6949	Model	Measurement
1	Glass-300	22.0 °C	7.70	7.70	7.30	-*
2	Glass-500	24.5 °C	7.70	7.70	7.75	-*
3	PV-300	32.0 °C	7.70	7.90	8.65	8.55
4	PV-300	42.0 °C	7.70	8.20	9.50	9.60
5	PV-800	50.0 °C	7.70	8.50	10.25	10.20

\* The heat flux could not measure with the temperature differences lower than 5 K.

**Table 6-2 Comparison of heat transfer coefficient from EN 410, ISO 6946, Models and measurement for conventional glazing and PV modules at different solar irradiation at vertical installation**

Therefore, with a good correlation between the temperature model and measurement, it can be concluded that the heat transfer coefficients were correctly considered in this simulation based on vertical installation with free ventilation behind the panels.

## 6.2.2 Variable tilted angle

With respect to variable tilted angles, vertical (0° from vertical), tilted (45° from vertical) and 0° horizontal installation will be considered. The amount of back-bias current was designed based on the emulation of 800W solar irradiation. For this validation, the same PV module was used;

- Free ventilation behind the modules – standard PV laminated glass
- Integrated thermal insulation behind the panels – PV building elements

### 6.2.2.1 PV-Laminated glass

Table 6-3 shows the front- and backside measured operating temperatures ( $T_{front}$ ,  $T_{back}$ ) and total external and internal heat transfer coefficients ( $h_e$ ,  $h_i$ ) together with simulated convection and radiation heat transfer coefficients ( $h_{e,conv}$ ,  $h_{e,rad}$ ,  $h_{i,conv}$  and  $h_{i,rad}$ ) based on different tilted angles. With a good correlation between measured and simulated heat transfer coefficients, it can be concluded that the heat transfer coefficients were correctly considered based on variable tilted angles without a gap behind the panels.

Tilted angles	Measurement						Simulation	
	Temperature (°C)			Heat transfer (W/m²K)			Heat transfer (W/m²K)	
	$T_{front}$	$T_{back}$	$T_{amb}$	$h_e$	$h_i$	$h_{total}$	$h_e$	$h_i$
0° Vertical	49,0	49,0	21,0	10,25	10,25	20,50	10,13	10,13
45° Tilted	49,9	50,3	20,0	10,60	8,90	19,50	10,52	9,09
90° Horizontal	53,6	54,1	21,0	10,40	7,00	17,40	10,36	6,89

**Table 6-3 Measured operating temperatures and heat transfer coefficients together with simulated heat transfer coefficients on both front- and backside of PV modules.**

Compared to a vertical installation, the lower total heat transfer coefficient ( $h_{total}$ ) of the PV module at a horizontal installation leads to a higher operating temperature of PV modules; 49°C for vertical installation and 54°C for horizontal installation. By increasing the tilt angles from vertical to horizontal installation, the internal heat transfer coefficient ( $h_i$ ) is reduced, while the external heat transfer coefficient ( $h_e$ ) is increased.

Table 6-4 represents the individual heat transfer coefficient corresponding to Table 6-3. The total convection heat transfer coefficient ( $h_{cov}$ ) can be calculated from natural and forced convection heat transfer coefficients ( $h_{conv,nat}$  and  $h_{conv,for}$ ) (6.1). The wind speed was measured on the surface of PV modules with an anemometer, as defined in 5.2.2.

$$h_{conv} = \sqrt[3]{(h_{conv,nat}^3 + h_{conv,for}^3)} \quad 6.1$$

Tilted angles	Simulation					
	Heat transfer (W/m²K)					
	External heat transfer ( $h_e$ )			Internal heat transfer ( $h_i$ )		
	$h_{e,conv}$		$h_{e,rad}$	$h_{i,conv}$		$h_{i,rad}$
	<i>natural</i>	<i>forced</i>		<i>forced</i>	<i>natural</i>	
0° Vertical	10,13			10,13		
	4,92		5,22	4,92		5,22
	4,32	3,38		4,32	3,38	
45° Tilted	10,50			9,09		
	5,29		5,23	3,88		5,23
	4,84	3,26		3,56	2,37	
90° Horizontal	10,36			6,89		
	5,02		5,34	1,55		5,34
	4,96	1,64		0,16	1,55	

**Table 6-4 Simulated of total heat transfer coefficients of both front- and backside together with composition of each natural and forced convection and radiation heat transfer coefficients.**

By increasing the tilted angle from vertical to horizontal installation, the external natural convection heat transfer coefficients ( $h_{e,conv,nat}$ ) are increased from 4.32 W/m²K to 4.96 W/m²K, while the internal heat transfer coefficients ( $h_{i,conv,nat}$ ) are reduced from 4.32 W/m²K to 0.16 W/m²K. It is important to note that the reason the  $h_{e,conv,nat}$  at 45° tilted angle is lower than at horizontal installation is the lower temperature difference between surface and ambient temperatures, not the tilted angle. This  $h_{e,conv,nat}$  becomes constant with a tilted angle higher than 30° from the vertical installation. At horizontal installation, the  $h_{i,conv,nat}$  of 0.16 W/m²K can be assumed as conduction heat transfer coefficients with Nusselt-number equals to 1, as described in Figure 3-8.

The forced heat convection is influenced by wind speed, but not at a tilted angle. On the front-side, the wind speeds measured are 0.35m/s, 0.33m/s and 0.11 m/s, while the wind speeds on the backside are 0.35m/s, 0.20m/s and 0.10m/s for vertical, tilted and horizontal installations.

The radiation heat transfer coefficient ( $h_{rad}$ ) is mainly influenced by on operating temperature and emission value of the surface. In this simulation, the emission of the glass surface is 0.837, while the emission of the surroundings is 0.94. For this simulation,  $h_{rad}$  is not influenced by the tilted angle due to the same emission value of the surrounding indoor measurement. For the real application outdoor, the emission of Earth and sky are 0.95 and 1.00, respectively. Moreover, the sky temperature is

not the same as the ambient temperature. Therefore, the radiation heat transfer coefficients on front- and backside ( $h_{e,rad}$  and  $h_{i,rad}$ ) will be different.

Even  $h_{e,conv,nat}$  at a horizontal installation is slightly higher than that of a tilted installation, the total  $h_e$  at a horizontal installation is still lower than  $h_e$  at a tilted angle due to different wind speed on the module's surface from 0.10m/s and 0.32m/s and corresponding  $h_{e,conv,for}$  from 3.26 W/m<sup>2</sup>K and 1.64 W/m<sup>2</sup>K, respectively.

#### 6.2.2.2 PV building elements

In the case of PV-building elements, the internal heat transfer coefficient ( $h_i$ ) cannot be measured on the backside due to the lower surface temperature. The difference between the surface and surrounding temperature becomes lower than 5K. Therefore, it can also be concluded that the thermal power will be dissipated only on the frontside. For this validation, the external heat transfer coefficient ( $h_e$ ) will be considered only on the frontside of PV building elements.

Table 6-5 exhibits the measured operating temperature ( $T_{front}$ ), ambient temperature ( $T_{amb}$ ) and external heat transfer coefficient ( $h_e$ ) together with simulated external heat transfer coefficients. In the simulated external heat transfer coefficients, all compositions of natural and forced convections have been considered together with the radiation heat transfer coefficient. By increasing the tilted angle from a vertical to a horizontal position, the operating temperature is decreased and the corresponding heat transfer coefficient is increased.

Eventhough the temperature difference between surface and ambient temperatures at vertical installation is higher compared to those of tilted and horizontal installations, the  $h_{e,conv,nat}$  is still lower due to the influence of the tilted angle on the natural convection. However,  $h_{e,conv,nat}$  at a horizontal installation is lower compared to that of a 45° tilted angle. This is because of the temperature difference, not tilted angles, as describe above.

Tilt angle	Temperature (°C)		Heat transfer coefficient (W/²K)			
	Measurement			Simulation		
	$T_{front}$	$T_{amb}$	$h_e$	$h_e$		
				$h_{e,conv}$		$h_{rad}$
				<i>natural</i>	<i>forced</i>	
0° Vertical	73,5	22,3	11,70	11,74		
				5,83		5,91
				5,16	3,94	
45° Tilted	71,5	22,8	12,10	12,16		
				6,30		5,86
				5,59	4,23	
90° Horizontal	66,5	22,5	13,00	12,94		
				7,23		5,71
				5,41	6,03	

**Table 6-5 Measured operating temperature and external heat transfer coefficient together with simulated external heat transfer coefficients**

Figure 6-4 describes the total heat transfer coefficients of PV-laminated glass and PV building element configurations on different tilted angles based on results in Table 6-4 and Table 6-5. With a higher tilted angle from vertical to horizontal installation, the operating temperature becomes higher in PV laminated glass due to a higher total heat transfer coefficient in vertical installation compared to a horizontal installation, which corresponds to higher thermal power dissipation. For PV building elements, the thermal power dissipation can be done only on frontside of modules. With the results in Table 6-5, the more tilted the angle from vertical to horizontal installation, the higher the total heat transfer coefficient and the more thermal power dissipation. Therefore, the operating temperature becomes lower with a higher tilted angle from vertical to horizontal installation.

In the practical case, it can be concluded that the  $h_{e,conv,nat}$  starts to be constant with the tilted angle higher than 30° from vertical. However, the  $h_{e,rad}$  keeps increase with the the tilted angle from vertical to horizontal intsalition due to the increment of heat exchange between the module surface and lower sky temperaute, as described in Table 3-11. The  $h_{e,conv,for}$  is influenced directly by wind speed, which is unpredictable.

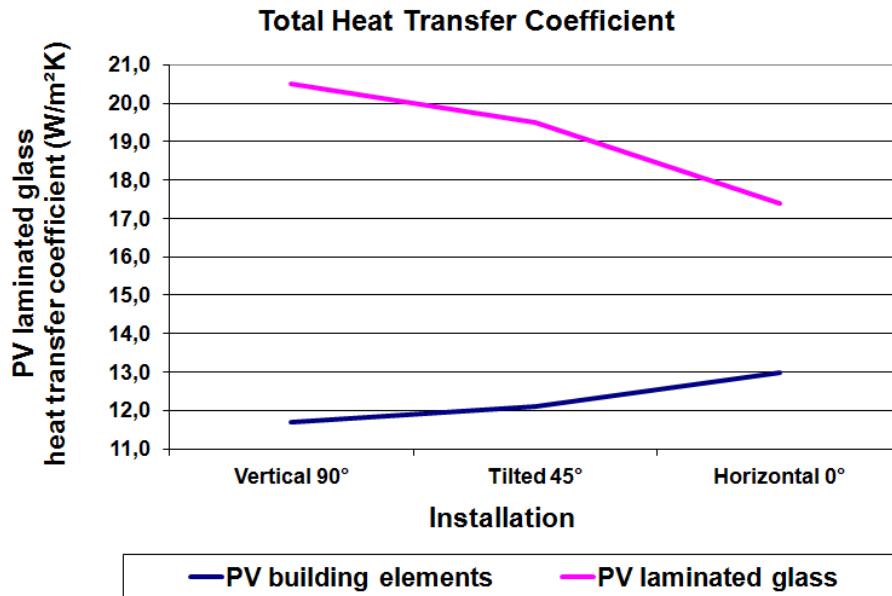


**Figure 6-4 Total heat transfer coefficients of PV-laminated glass and PV building element configurations on different tilted angles**

With a positive correlation between the temperature model and measurement, it can be concluded that the heat transfer coefficients were correctly considered in this simulation, as based on variable tilted angles and different multi-layered configurations.

### 6.2.3 Variable gaps behind the panels

For this experiment, the variable gap of 5 cm and 10 cm was considered together with tilted angles from vertical to horizontal installation (5.2.2). The amount of back-bias current was designed based on the emulation of 800W solar irradiation. In this test, only the backside of PV module was considered with a variable gap behind the PV modules. The front side was not taken into account.

Gap	Tilt angle	Measurement			Simulation (W/m <sup>2</sup> K)			
		Temepature (°C)		$h_{i,gap}$ (W/m <sup>2</sup> K)	$h_{i,gap,total}$	$h_{conv}$		$h_{rad}$
		$T_{m,back}$	$T_{wall}$			natural	forced	
10cm	Vertical	59,0	41,6	12,7	12,59	3,94		8,65
						3,33	2,90	
	Tilted	60,0	43,5	12,6	12,51	3,75		8,76
						2,98	2,97	
	Horizontal	64,0	46	12,0	12,01	2,97		9,04
						0,26	2,97	
5cm	Vertical	60,0	42,5	12,6	12,54	3,82		8,72
						3,3	2,70	
	Tilted	60,6	46,0	12,9	13,12	4,22		8,90
						2,89	3,71	
	Horizontal	65,0	52,1	12,2	12,22	2,90		9,32
						0,53	2,90	

**Table 6-6 Measurement of operating temperature of PV module at backside and wall temperature and total gap heat transfer coefficient ( $h_{i,gap}$ ) together with corresponding simulated heat transfer coefficients.**

Table 6-6 describe the measured operating temperature of the PV module on the backside and the wall temperature, the front side of the extruded rigid polystyrene foam (XPS), together with the total gap heat transfer coefficient ( $h_{i,gap}$ ). At the same time, each of the heat transfer coefficients are simulated. These are the natural, forced and radiation heat transfer coefficients.

Therefore, under a steady state condition, the temperature model, especially the dissipation power sub-model, has been correctly considered on the variable tilted angles, ventilation gap behind the modules and multi-layered configurations.

### 6.3 Electrical power and energy yields

Aside from the module specification, the solar irradiation and operating temperature are the most important parameters. For the solar irradiation parameter, the power input to PV module can be obtained from the solar cell sensor, as described in 3.3.1, in which reflection and spectrum losses have already been excluded. In order to get the operating temperature, the dissipation power has to be taken into account together with the heat capacity of the module. Since the dissipation power model (3.3.3) has already been validated under a steady state condition, it has to be further

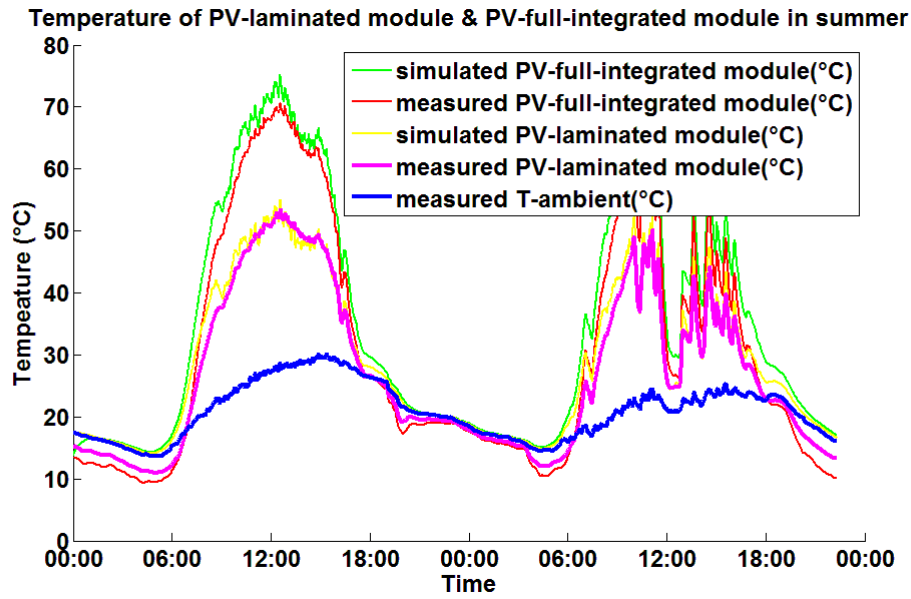
validated together with the heat capacity of the PV module and solar irradiation input under a real-time (dynamic) condition. In this validation, all components in the power balance model have to be taken into account: power input, electrical power, dissipation power and absorption power.

Figure 6-5 represents the simulated and measured operating temperature of 2 different multi-layered configurations - PV-laminated glass and PV full-integrated element, as described in

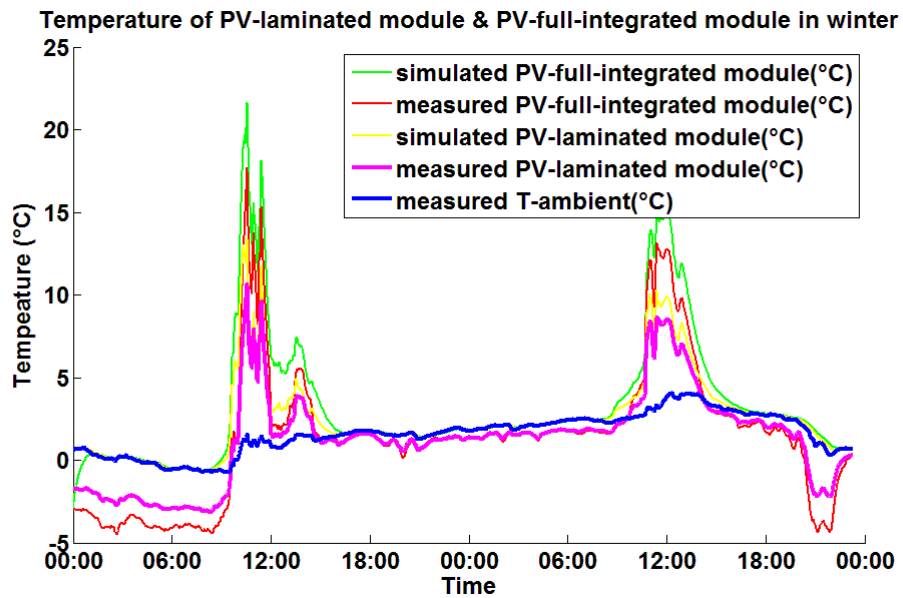
Figure 5-7, with the real-time outdoor PV module measurement. The measurement was done at Fraunhofer IWES with a time resolution of one minute. To validate the temperature under different conditions, figure 6.5-a represents the operating temperature during the summer period, 27.-28.07.2009, while figure 6.5-b represents during the winter period, 27.-28.12.2009. For PV-laminated glass and PV composite element, the temperatures reach  $\sim 55^{\circ}\text{C}$  and  $\sim 70^{\circ}\text{C}$  in summer, while they reach  $\sim 12^{\circ}\text{C}$  and  $\sim 17^{\circ}\text{C}$  in winter.

With a good correlation between simulated and measured operating temperatures, it can be concluded that the temperature model was correctly considered under both steady state and real-time (dynamic) state condition.





(a)



(b)

**Figure 6-5 Simulation and measurement of operating temperature of PV module and PV-composite element in summer (a) and in winter (b).**

In comparison to other temperature models, Figure 6-6 exhibits the differences of temperature models with and without any consideration of the heat capacity, which means the power balance model and other temperature models, respectively. In order to consider the effect of the heat capacity of the PV module exclusively, the real-time heat dissipation together with iteration method were employed for both models in the simulation. The operating temperature of the temperature model, without heat capacity, changes rapidly and does not match the measurement, whereas the power balance model, with the consideration of heat capacity, exhibits

the time-delay of the operating temperature, which matches the measurement. The temperature differences with and without time-delay can reach up to 10°C, which directly affects the real-time power output and surface temperature for the energy consumption simulation.

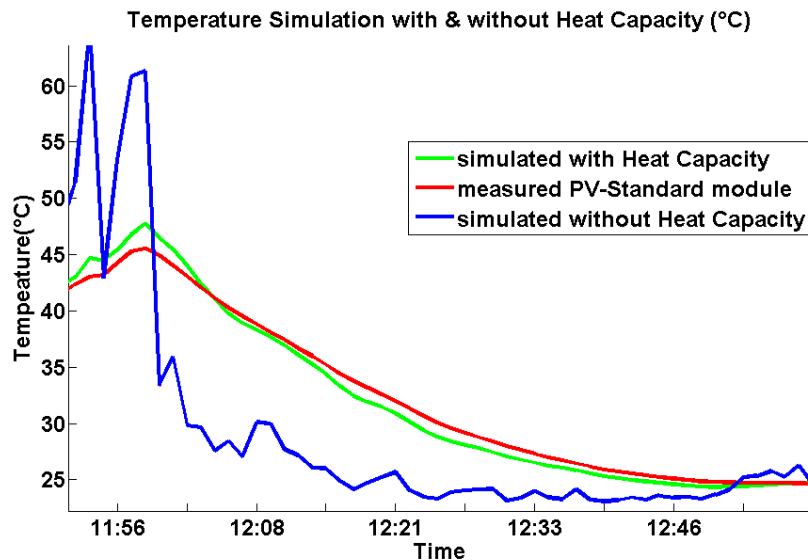


**Figure 6-6 Simulation of operating temperature between with and without consideration of heat capacity of PV module in compared to the measurement of module temperature.**

With the real-time outdoor PV module measurement in Figure 6-5, Figure 6-7 represents the simulated internal and external heat transfer coefficients of PV-laminated and PV full-integrated modules (Figure 5-2, Table 5-2). These simulated coefficients are based on a one-day measurement of the surface and ambient temperatures of the PV modules during the summer and winter periods. It can be seen that the heat transfer coefficient is not constant. The wind speed seems to dominate these heat transfer coefficients. At front- and backside of PV-modules, the internal and external heat transfer coefficients are quite identical (Figure 6-7a, b). With the different surface temperatures of the PV full-integrated modules in summer, Figure 6-7b exhibits the differences between the internal and external heat transfer coefficient even though both surfaces face the same wind speed. The internal heat transfer coefficient is lower than the external heat transfer due to the lower surface temperature of the backside compared to the surface temperature of the front side. In winter, however, the surface temperatures on both sides of PV full-integrated modules are identical, which leads to identical heat transfer coefficients (Figure 6-7d). In the BIPV application, both surfaces are confronted with different surface temperatures and wind speeds, which leads to different heat transfer coefficients. These

coefficients are one of the critical parameters to predict the power output and thermally relevant building functions.

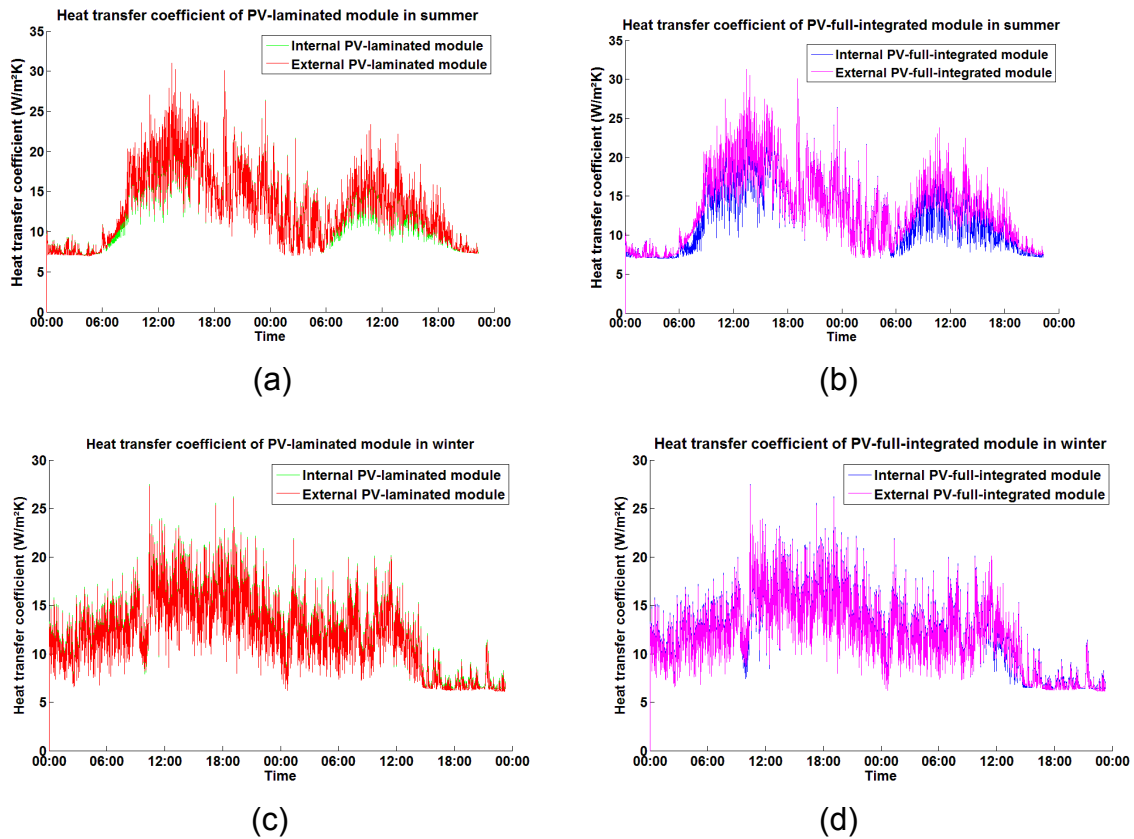


**Figure 6-7 Simulated internal and external heat transfer coefficients; in summer: PV-laminated modules (a), PV-composited modules (b); in winter: PV-laminated modules (c), PV-composited modules (d)**

## 6.4 Mechanical Behaviour

The mechanical behaviour of PV modules is influenced mainly by operating temperature, load duration, mechanical loads and clamping distance, etc. Table 6-7 represents the test scenarios in which operating temperature, mechanical load and load duration are evaluated. Moreover the mechanical model can be further validated with a variable mounting system, standard-conform or manufacturer-specific mounting systems, together with different substrates of the PV multi-layered configurations, glass and backsheet. The test configuration and mechanical load in each of the test configurations are described in the mechanical testing equipment (5.2.3). The different operating temperatures could be achieved by a back-bias current concept (5.2.1).

**Scenario-1 Thermally induced**

A change in the operating temperature of the strain gauge will normally produce a resistance change in the gauge without any consequences on the mechanical load. Therefore, the function test of the strain gauge has to be investigated together with the deflection sensor under the consideration of temperature-depending sensors and materials. This function test could also be applied for future works of real-time outdoor measurement. Moreover, the self weight of the PV modules could also be evaluated by flipping the PV modules.

**Scenario-2 Mechanically induced load**

Since the temperature-induced load was investigated, the mechanical-induced load has to be evaluated separately without any thermal induced load.

**Scenario-3 Mechanically and thermally induced load combination**

With respect to the real situation of the PV module and the validation of the mechanical model, the combination of thermal- and mechanical induced were examined.

**Scenario-4 Load Duration**

In order to evaluate the time-depending creep and relaxation characteristics of interlayer, the long load duration is needed.

Load Scenarios	Description	Temperature	Mechanical Load ( $W_{\max}$ )	
			20 min	1 hour
1	Thermal-induced	40 °C	-	-
		60 °C	-	-
2	Mechanical-induced	20 °C (room)	100%	-
			50%	-
3	Thermal- & Mechanical-induced	40 °C	75%	-
		60 °C	50%	-
4	Load duration	20 °C (room)	-	100%
		40 °C	-	75%
		60 °C	-	50%

**Table 6-7 Mechanical test scenarios for validation of self-weight, operating temperature and load duration.**

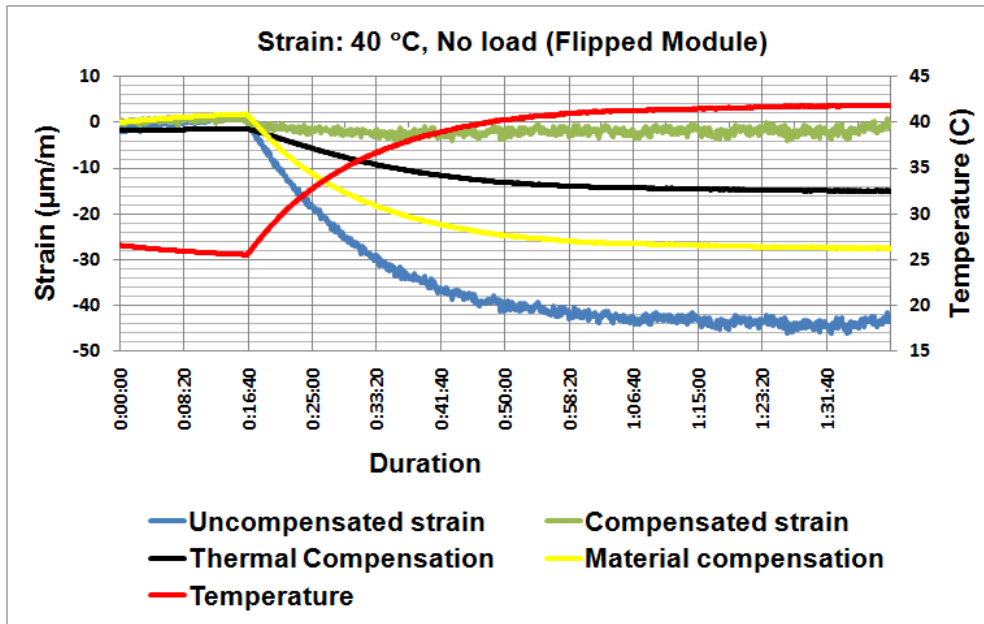
#### **6.4.1 Standard-conform mounting system with PV-laminated glass**

This experiment deals with a 2-sided standard-conform mounting system and standard PV-laminated glass. In this case, the clamping depth of the mounting system conforms to building code EN12488, which is much stricter compared to the manufacturer-conform mounting system.

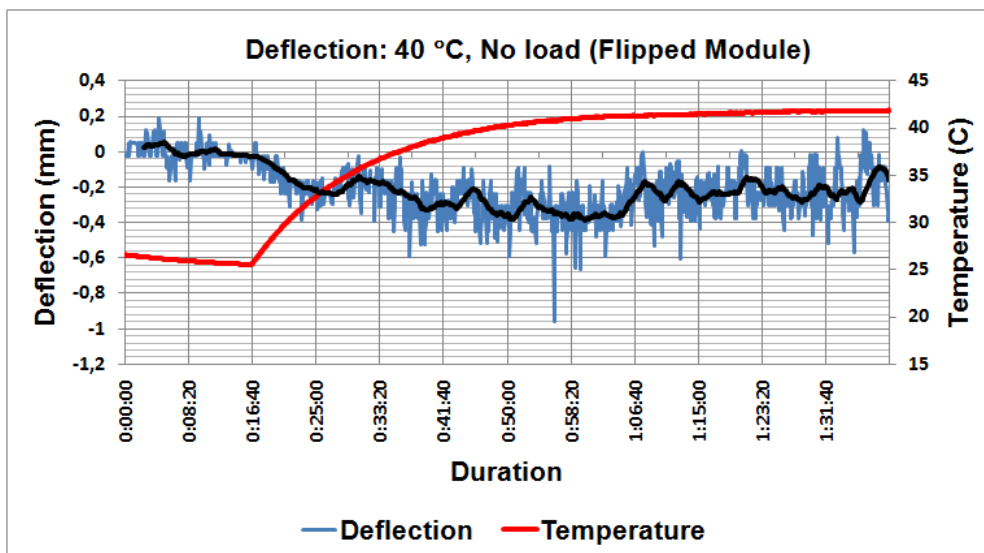
##### Scenario-1 Thermally induced load

With respect to the sensitivity of the strain gauge measurement on operating temperature and material used, described in 5.2.3, Figure 6-8 shows the measurement of the bending strain of an own load scenario in comparison with the uncompensated strain, the thermal compensation output from the strain gauge, the material compensation from thermal expansion of material mismatch and the final compensated strain together with operating temperature. It was done by flipping the module, in which the strain gauge is on the top of the glass surface. Since the compensation of the material and the thermal output were included, there is still some small offset in the compensated strain, because the heat could not be distributed equally over the whole module through a metal contact, glass and the interlayer. However, with regards to the accuracy of the temperature measurement, it is regarded as an acceptable measurement. Therefore, the test results indicate that the theoretical compensation is valid to solely determine the mechanically induced strain. This determination is valid firstly only on glass substrate. It can be seen that there is no apparent self weight effect in the strain measurement when it is flipped upside down (strain gage on the top surface). In this case, we assumed that the self-weight can be neglected for standard PV laminated glass and does not need to be taken into account in our test measurements.

Figure 6-9 indicates the deflection at elevated temperatures without applying mechanical loads. The results show that there are swings in the deflection curve when the temperature increases. At a certain point, the curves swing back to the origin, where the deflection is zero. The swing in the graphs is clearly the effect of the temperature radiated from the PV module. In this case, the displacement sensor has its own internal thermal drift, which compensates for the thermal effect at a certain time period.



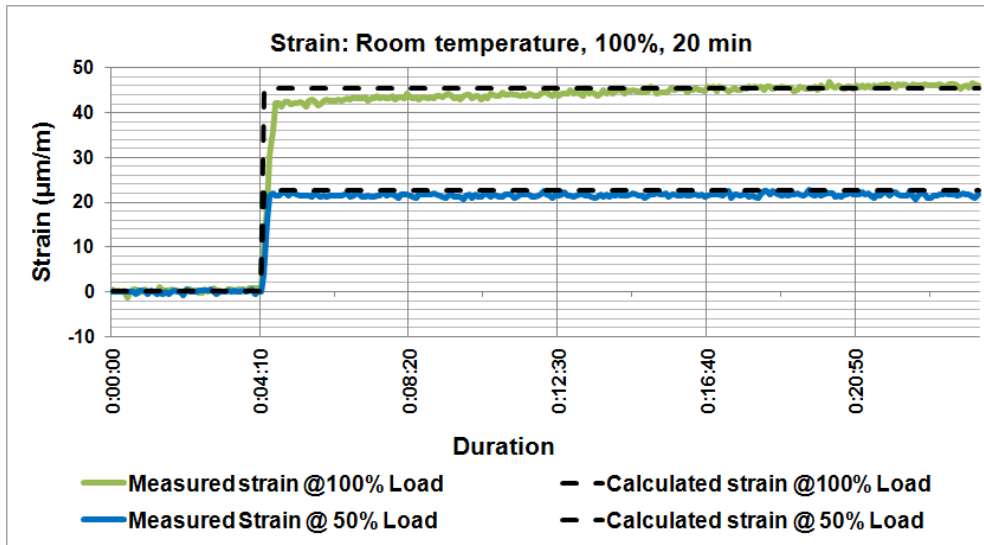
**Figure 6-8 Bending Strain at 40°C with own load, without applied mechanical load**



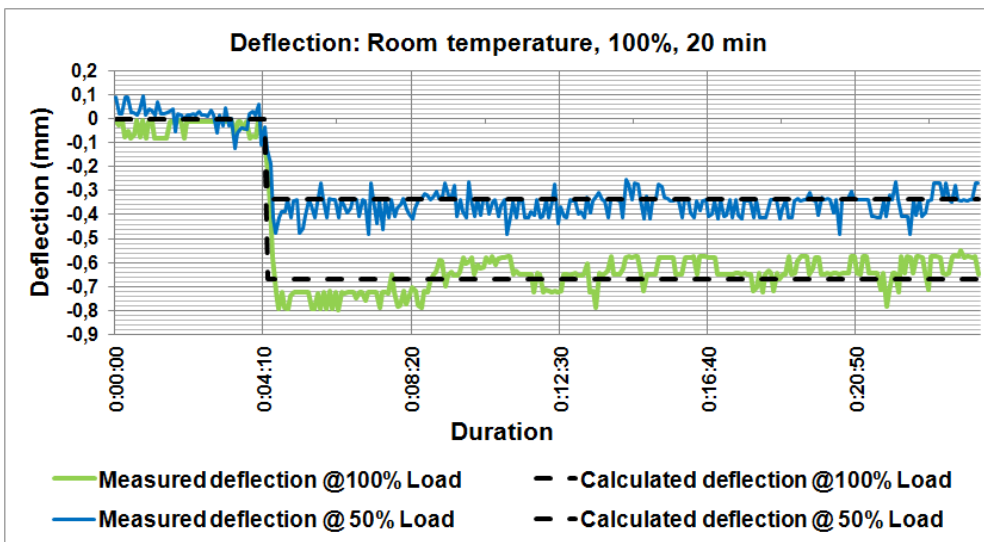
**Figure 6-9 Deflection at 40 °C with own load, without applied mechanical load.**

#### Scenario-2 Mechanically induced load

Figure 6-10 shows the comparison between measured compensated strain and calculated mechanical strain. The calculation method for the mechanical strain is described in 4.5.2. Note that there is a good correlation between the experimental and theoretical data in the room temperature range. The results indicate that mechanically induced stress at room temperature (temperature is stable) is predictable.



**Figure 6-10 Bending strain at 100% and 50% mechanical load for 20 minutes.**



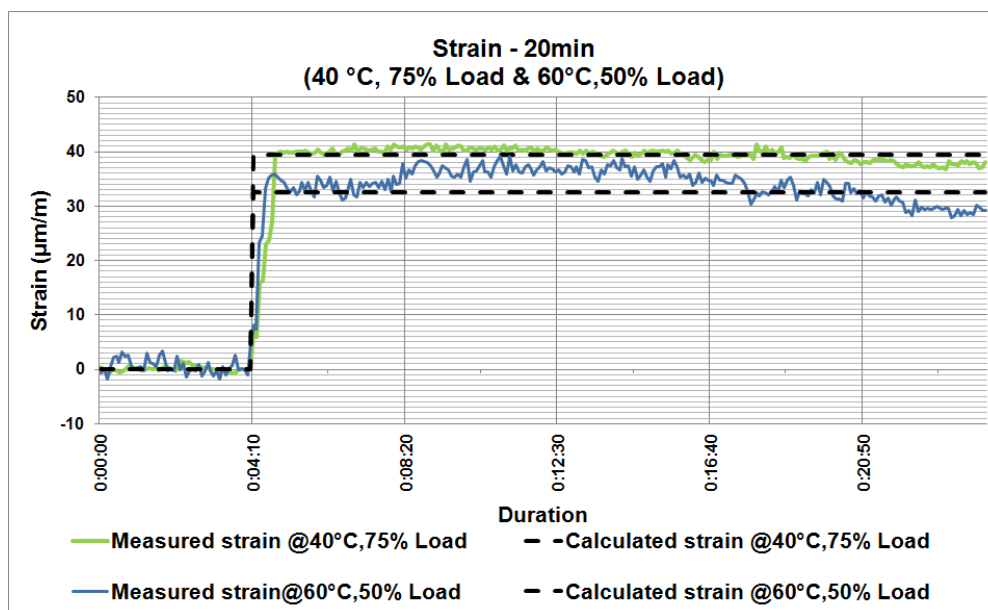
**Figure 6-11 Deflection from 100% of mechanical load applied for 20 minute.**

Figure 6-11 shows the comparison between experimental deflection and theoretical deflection in the PV module. The diagrams indicate a good correlation. There were also noises in our deflection measurement, since the displacement sensor is very sensitive to the change in the distance. The deflection results prove the validity of the model in prediction of deflection in a BIPV module under room temperature conditions.

### Scenario-3 Thermally and mechanically induced Load

Figure 6-12 indicates the strain from the combination of thermally and mechanically induced loads: 40°C with 75%-load and 60°C with 50%-load. After thermal compensation in the strain measurement, the diagrams show good results for the

measured strain compared with the theoretical calculation, as described in 4.5.2. During the short period of testing time, the test results show that the experimental results match with the proposed theoretical model. This ensures the validity of the model in predicting the strain with the effects from the temperature and mechanical loads. Notice that after loading, the strain curves have the tendency to gradually decrease. This is the result of the relaxation behavior of the interlayer, as mentioned in Chapter 3. This will be further validated in scenario-4 long load duration.



**Figure 6-12 Combined bending strain from temperature at 40 °C with 75% of mechanical load and temperature at 60 °C with 50% of mechanical load for 20 minutes duration.**

Figure 6-13 reveals that the experimental data and theoretical data correlate. However, there is noise in the measurement due to its sensitivity to small vibrations and the sampling rate. As a result, the experimental data validates the application of the proposed model to be used for the estimation of the deflection in the BIPV module with different combinations of operating temperature and mechanical load conditions.



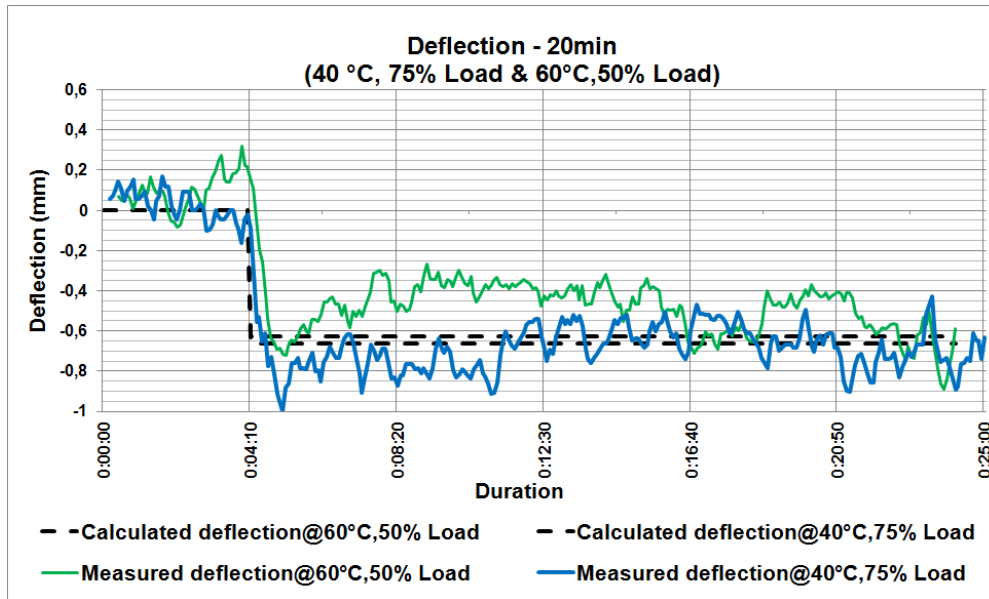
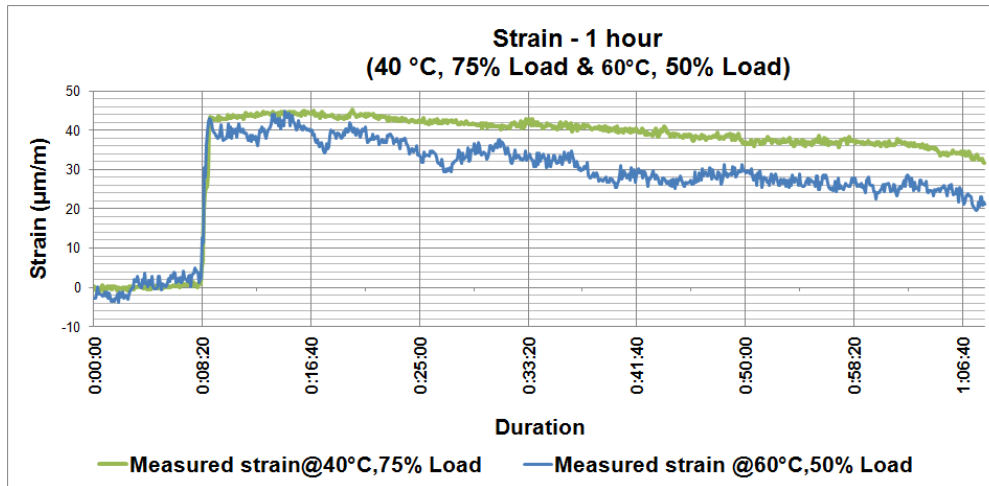


**Figure 6-13 Deflection at temperature at 40 °C with 75% of mechanical load and temperature at 60 °C with 50% of mechanical load for 20 minutes duration.**

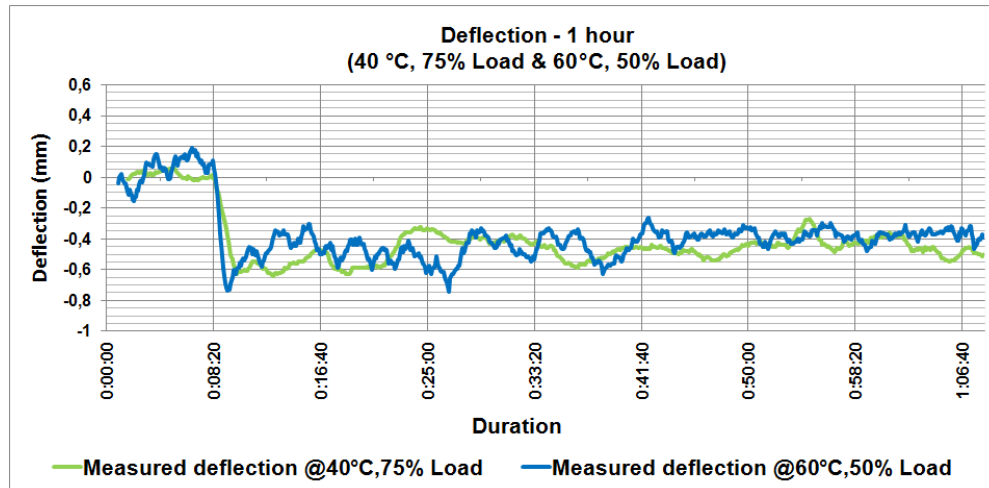
#### Scenario-4 Load duration

Figure 6-14 exhibits that the strains decrease slightly due to long load duration at the elevated temperature. This can be explained by the creep and relaxation behavior mentioned in 4.2.1. At an operating temperature of 60°C, the strain decreases faster compared to that at 40°C. Hence, the creep and relaxation characteristics of the interlayer used is temperature-dependent. In Figure 6-15, the measured deflections are acceptable compared with the theoretical calculation. Error still occurs in the measurement due to the sensitivity of the displacement sensor.

With a correlation between the measured and calculated strain and deflection, the mechanical model is applicable to PV-laminated glass with a standard-conform mounting system. As a result of this experiment, the variable operating temperature can be emulated with the back-bias current concept. Therefore, this new cost-saving test method is also applicable.



**Figure 6-14 Combined bending strain at temperature at 40 °C with 75% of mechanical load and temperature at 60 °C with 50% of mechanical load for 1 hour duration.**



**Figure 6-15 Deflection at temperature at 40 °C with 75% of mechanical load and temperature at 60 °C with 50% of mechanical load for 1 hour duration.**

#### 6.4.2 Manufacturer-conform mounting system with PV-laminated glass

This experiment deals with standard PV-laminated glass and a 4-sided manufacturer-conform mounting system. In this case, the clamping depth of the manufacturer-conformed mounting system is much lower compared to a standard-conform mounting system. Since the thermal and material compensation in 6.4.1 were validated, the experiment with a thermal-induced load in scenario-1 is not needed.

### Scenario-2 Mechanically induced load

Figure 6-16 indicates the mechanical behaviour at room temperature, wherein the thermally-induced load does not occur. The experimental strain exhibits its behavior complying with the theoretical calculation at room temperature, while the deflections obtained from the test measurement show a significant mismatch with the theoretical calculation. In terms of strain, the proposed mechanical model is valid for the prediction of the mechanical behavior of the PV modules, which means that parameter k1 in Table 4-7 is still valid. However, the mechanical model seems to be invalid for the deflection measurement, since the PV module has a clamping depth less than the permitted values defined in building codes. In order to adapt the mechanical model for individual manufacture specific mounting system, the parameter k2 in Table 4-7 has to be developed.

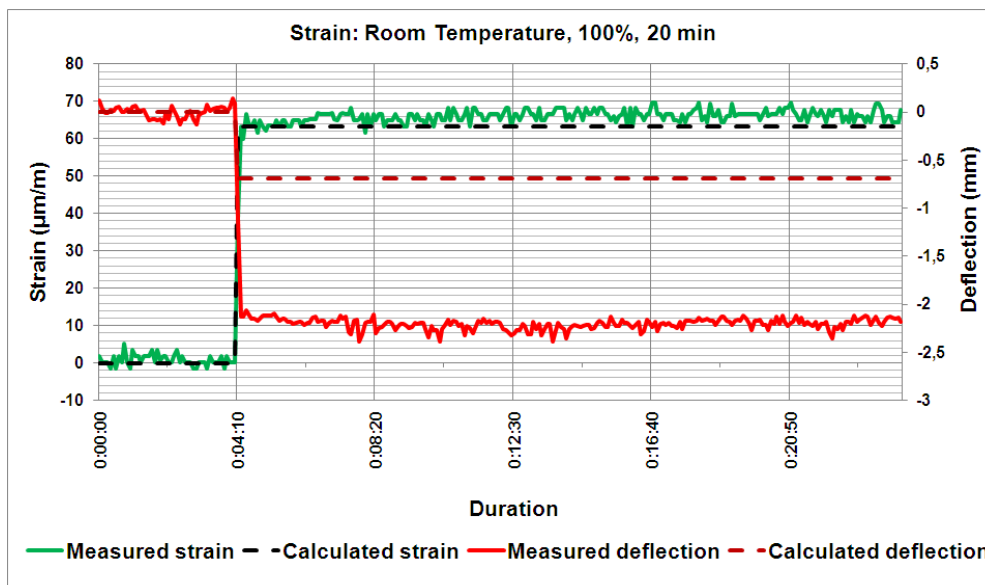


**Figure 6-16 Bending strain at room temperature with 100% of mechanical load for 20 minutes.**

### Scenario-3 Thermally and mechanically induced Load

Figure 6-17 indicate the combined effect of the mechanically and temperature induced strain. The calculated strain is correlated with the measured strain in scenario-2. However, in this graph, the calculated strains are slightly different from the measured strain. With respect to manufacturer and material specific characteristics of the interlayer used, the shear modulus of the interlayer used is slightly different from Table 4-1 at a higher operating temperature. In this case, it can be concluded that the mechanical model is still valid under a thermal and mechanically induced load.

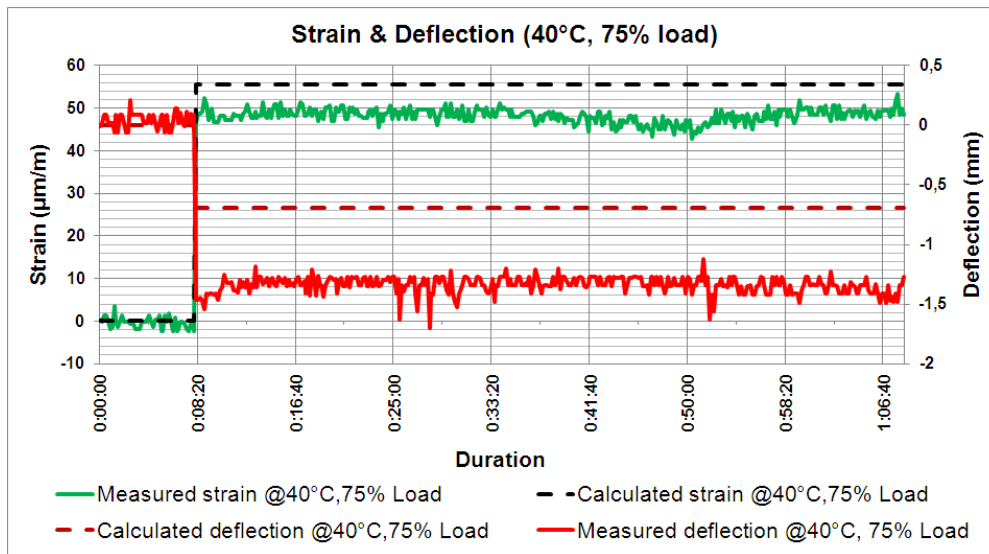


**Figure 6-17 Combined bending strain at temperature at 40° with 75% of mechanical load for 1 hour duration.**

At the same time, the calculated deflection does not match the measured deflection due to the mismatch in parameter  $k_2$ , as mentioned in scenario-2. Therefore, the  $k_2$ -parameter in Table 4-7 has to be developed for the individual manufacture specific mounting systems.

From the measurement above, the strain curves have the tendency to be constant along the test period. It can be concluded that the interlayer used has very small creep and relaxation characteristics. Therefore, the measurement in scenario-4 is not needed.

Regarding the correlation between the measured and calculated strain, the mechanical model is only applicable for the strain calculation for PV-laminated glass with a standard-conform mounting system, while the new parameter  $k_2$  has to be developed for an individual manufacturer specific mounting system. Moreover, the function test of strain and deflection measurement sensors are applicable for PV-laminated glass module configuration under indoor measurement. For future work on real outdoor measurements, these sensors have to be further validated.

With respect to the new developments of the interlayer used in PV industries, however, the shear modulus of each interlayer is needed. It can be obtained by the Dynamic Mechanical Analysis (DMA) and differential scanning calorimetry (DSC), as described in chapter 4.2.3. This will be useful for the module design to fulfil the requirements in building regulations.

### 6.4.3 Manufacturer-conform mounting system with PV-glass-backsheet

Since the measurements on PV-laminated glass were validated in the previous chapter, the PV-glass-backsheet was measured in this experiment in order to prove the applicability of measurement on different substrates. This experiment deals with a 4-sided manufacturer-conform mounting system. In this case, the clamping depth of manufacturer-conform mounting system is much lower compared to the standard-conform mounting system.

#### Scenario-2 Mechanically induced load

Figure 6-18 indicates a significant mismatch on strain and deflection from the data measured compared to the theoretical value. The results can be explained by the variable non-standard-conform mounting system together with the unavailable material characteristics of the backsheet. From this experiment, which was done at room temperature, it can be concluded that the function test of strain and deflection measurement sensors is applicable to the PV-glass-backsheet. However, it is worth investigating the new parameter of  $k_1$  and  $k_2$  in Table 4-7 for an individual manufacturer specific mounting system.

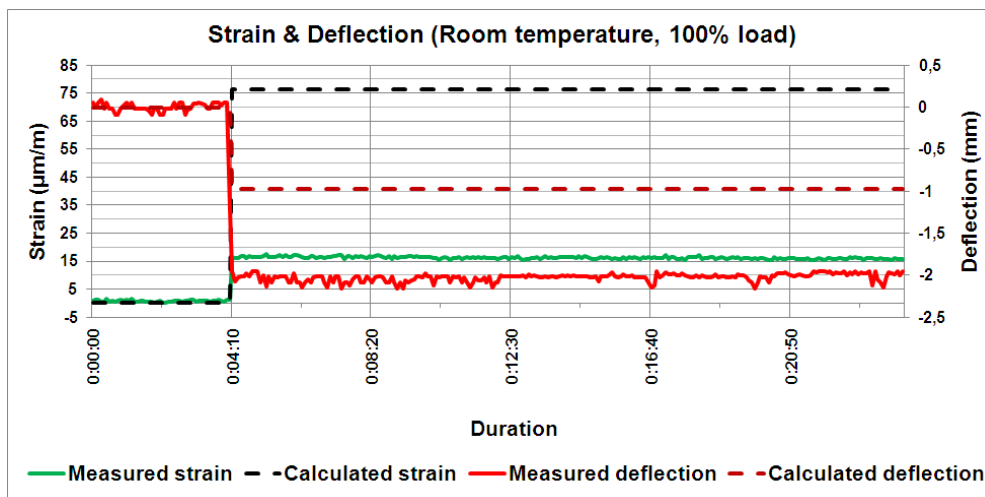


**Figure 6-18 Bending strain at room temperature with 100% mechanical load for 20 min.**

#### Scenario-3 Thermally induced load

With respect to the plastic characteristics of backsheet material, the thermally induced load is worth studying. Since the deflection sensor is a contactless measurement, the strain measurement with strain gauge will, therefore, be properly investigated. Though there is no mechanical load provided, the measured strain,

including all compensations still increases with operating temperature, (Figure 6-19). Therefore, it can be concluded that the strain measurement is not applicable to the backsheet substrate. The material characteristics of the backsheet are worth further study.

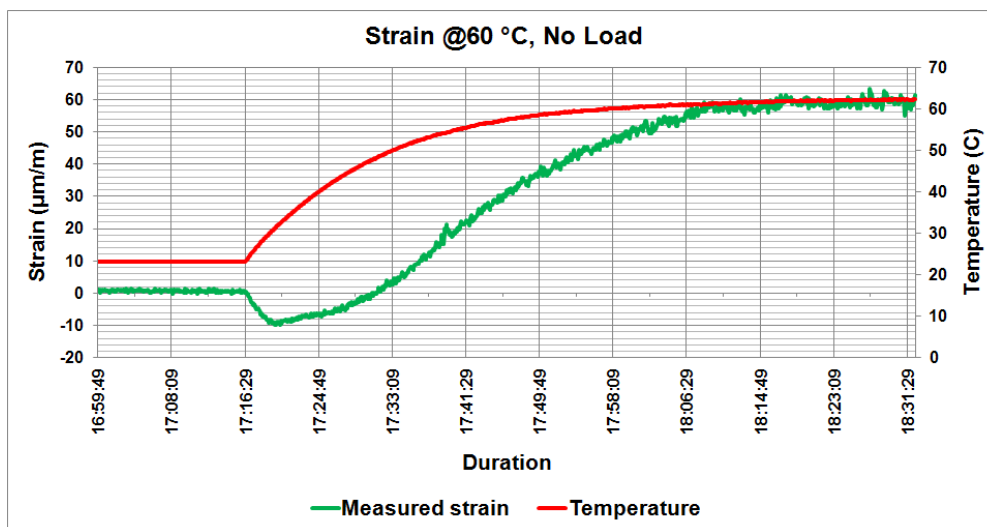


**Figure 6-19 Bending strain at 60 °C, without mechanical load.**

For future work on of real-time outdoor measurement, only deflection sensors will be used due to the non-applicability of the strain gauge to backsheet material.

## 7 Evaluation

The operating and surface temperatures of the PV module are the most significant parameters compared to other relevant electrical, thermal and mechanical characteristics. In BIPV applications, the power dissipation component becomes the most complicated component in the evaluation of the operating and surface temperature. Therefore, the dissipation power components will be exclusively investigated.

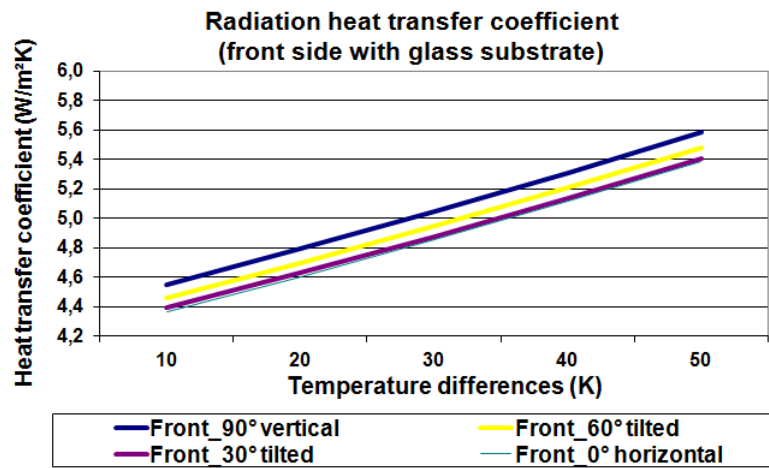
In order to fulfill the requirements of the Construction Product Directive (CPD) and building regulations for BIPV applications, the other building relevant functions have to be taken into account, complementary to electrical characteristics. With respect to the unavailable information on the BIPV module regarding a higher operating temperature compared to conventional building products, the thermal and mechanical characteristics are further investigated in this work.

### 7.1 Power Dissipation components

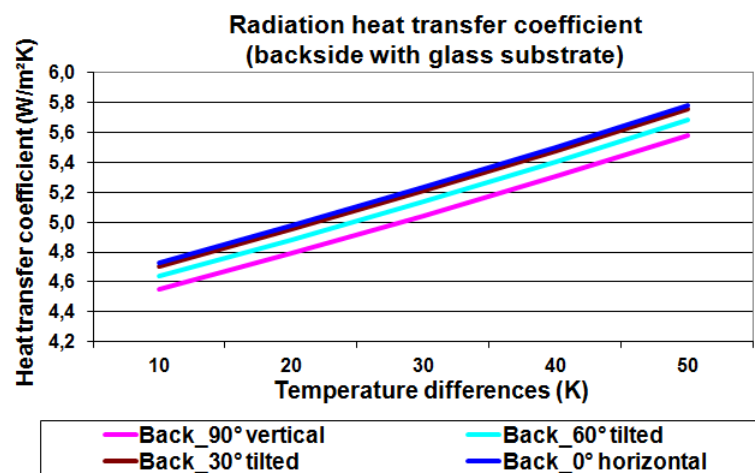
As the conduction heat transfer coefficient of the substrate used is almost constant, independent from the operating temperature, the radiation and convection heat transfer coefficients will be considered exclusively.

#### 7.1.1 Radiation heat transfer coefficient

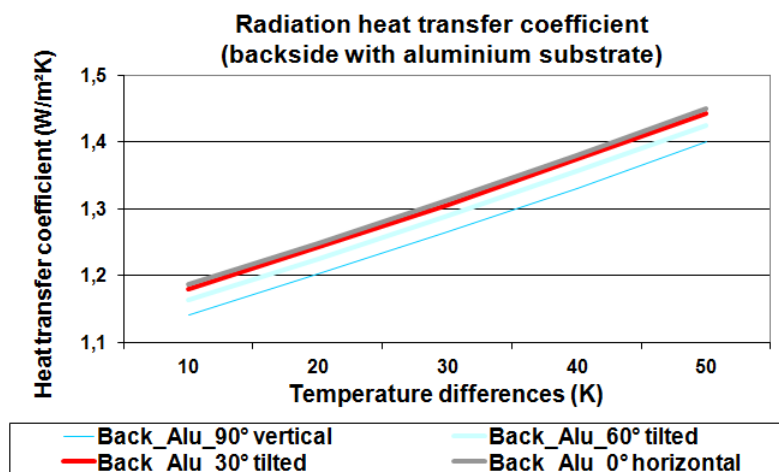
With respect to validated power balance models in the previous chapter, Figure 7-1 represents the simulated radiation heat transfer coefficients ( $h_{rad}$ ) of the PV module on the front and backside of different substrates for different tilt angles and temperature differences between surface and surrounding temperature, which are based on the calculation method in Table 3-10. The PV module configurations are assumed to be PV-laminated glass with glass emissivity of 0.837 and PV-Aluminium sheet with aluminium emissivity of 0.21. This PV-Aluminium sheet is fabricated by gluing the flexible PV module on aluminium sheet building products mostly used in industrial roofing. It reveals that  $h_{rad}$  mainly depends on the emissivity of material used, temperature differences, and slightly on the tilted angles of the front and backside of the PV module.  $h_{rad}$  rises with higher temperature differences.



(a)



(b)



(c)

**Figure 7-1 Radiation heat transfer coefficient on front- and backside of PV module with different backside emissivity at different tilt angles and temperature differences.**



Figure 7-1a represents the reduction of the front side radiation heat transfer coefficient  $h_{rad,front}$  from the vertical to horizontal tilted angle, while Figure 7-1b represents the increment of the backside radiation heat transfer coefficient  $h_{rad,back}$  from vertical to horizontal tilted angle. With respect to the sky, the temperature is lower compared to the Earth temperature and the parameter of  $\cos \alpha_{PV}$  in Table 3-10, the spherical area of radiation heat exchange between the frontside surface and the Earth temperature becomes lower, and that between the frontside surface and sky temperature becomes higher. While the PV module changes its tilted angle from vertical to horizontal, the radiation heat transfer coefficient of the frontside of the PV module ( $h_{rad,front}$ ) becomes lower (Figure 7-1a); and the radiation heat transfer coefficient of the backside of the PV module ( $h_{rad,back}$ ) becomes higher (Figure 7-1b).

Moreover, it can be seen that the lower emissivity of the aluminium substrate exhibits a significantly low radiation heat transfer coefficient compared to glass substrate (Figure 7-1b, c). Therefore, the emissivity of material used on the backside and substructure needs to be properly taken into account for the PV system designs.

### 7.1.2 Convection heat transfer coefficient

The convection heat transfer coefficient can be considered under forced and natural convection. The forced convection heat transfer is influenced mainly by wind speed, while the natural convection heat transfer coefficient is influenced by temperature differences, tilted angles, etc. Therefore, it is worth investigating the role of forced convection in comparison to natural convection.

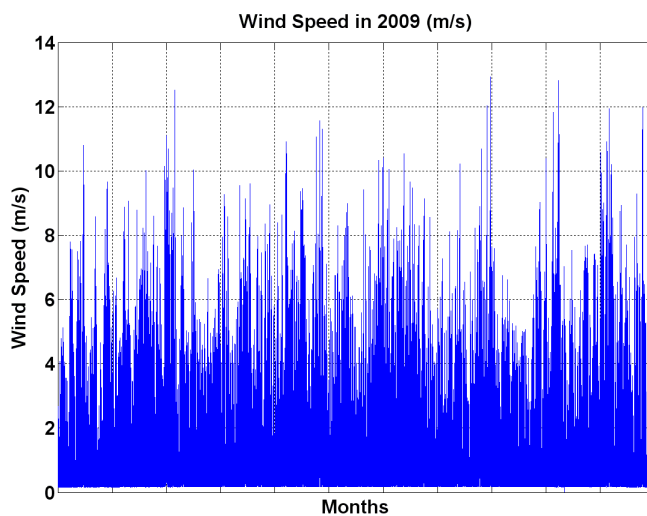
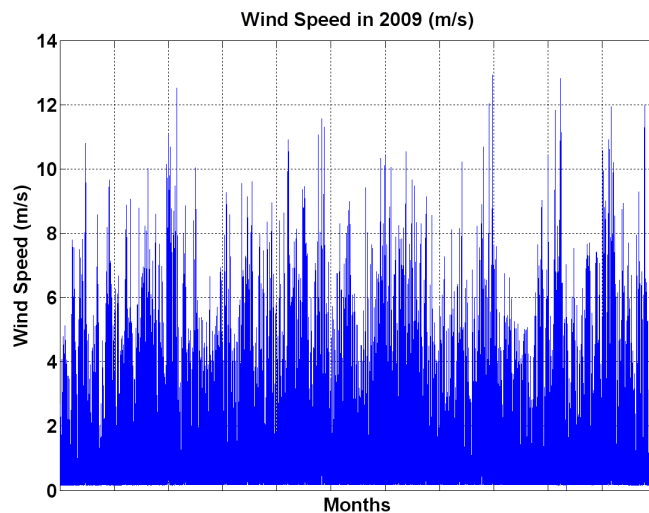


Figure 7-2 exhibits the wind speed at Fraunhofer IWES in Kassel, Germany. It was measured by an anemometer at a 15-sec time interval. Excluding wind speed during

the night and some errors in measurement, it can be concluded that a wind speed lower than 1m/s is around 50% of the total wind speed measurement.

With respect to the wind speed above, Figure 7-3 explains the Nusselt number (***Nu***) and heat transfer coefficient (***h<sub>conv</sub>***) of free convection for both the front and backside of the PV module, 2m height and 1.2m width, with various temperature differences from 10-50 K and vertical to horizontal tilt angles (90° - 0°) together with a forced convection at a wind speed of 0.25 – 1.00 m/s. The calculation of the Nusselt number (***Nu***) and heat transfer coefficient (***h<sub>conv</sub>***) described is based on Figure 3-7 - Figure 3-10.



Wind speed (m/s)	Times
< 0.2	118121
0.2-0.3	72547
0.3-0.4	65085
0.4-0.5	58196
0.5-0.6	53772
0.6-0.7	49330
0.7-0.8	46096
0.8-0.9	42979
0.9-1.0	40385
< 1.0	<b>546511</b>
>= 1.0	<b>544008</b>
Total	1090519

**Figure 7-2 Wind speed at Fraunhofer IWES over 1 year with 15-sec time Interval**

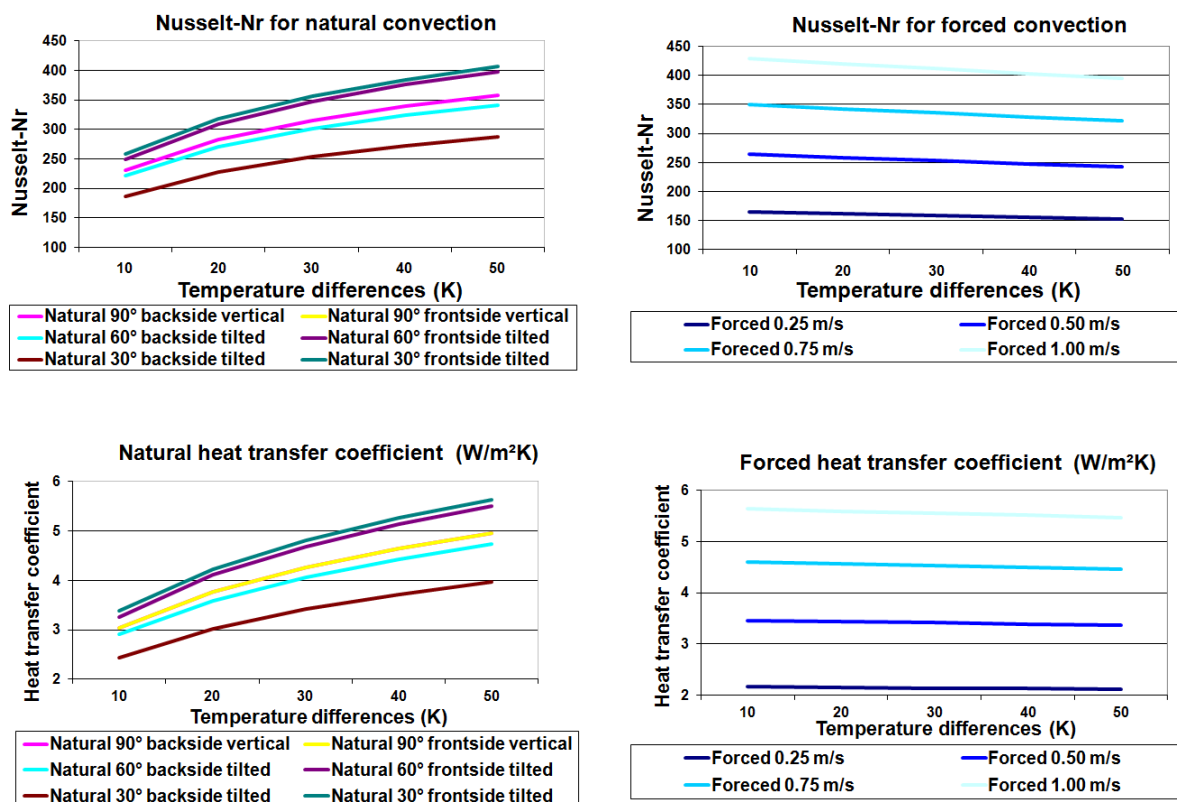


**Figure 7-3 Nusselt-number and heat transfer coefficient of natural and forced convection at different multi-layered configuration and wind speed, respectively.**

It can be seen that the Nusselt-numbers of natural convection are in the range of 200-400, while the Nusselt-numbers of forced convection at 0.25m/s, 0.50, 0.75 and 1.0 m/s are in the range of 150, 250, 350 and 400, respectively. The heat transfer

coefficients of natural convection are in the range of 2.5 – 5.5 W/m<sup>2</sup>K, while those of forced convection are in the range of 2.0 – 5.5 W/m<sup>2</sup>K, respectively. The reduction of the heat transfer coefficient in forced convection is caused by the reduction of heat conductivity of fluids with higher temperature differences. Thus, it can be concluded that the heat transfer coefficient of natural convection is quite comparable to that of forced convection with a wind speed lower than 1.0 m/s.

Even in a standard free-standing PV module, where both the front and backside face the same conditions, natural convection plays a major role in heat dissipation compared to forced convection. This is due to 50% of total wind speed being lower than 1 m/s. Especially for the BIPV application, the natural convection completely takes place at the ventilation behind the PV modules. Therefore, this natural convection has to be considered properly.

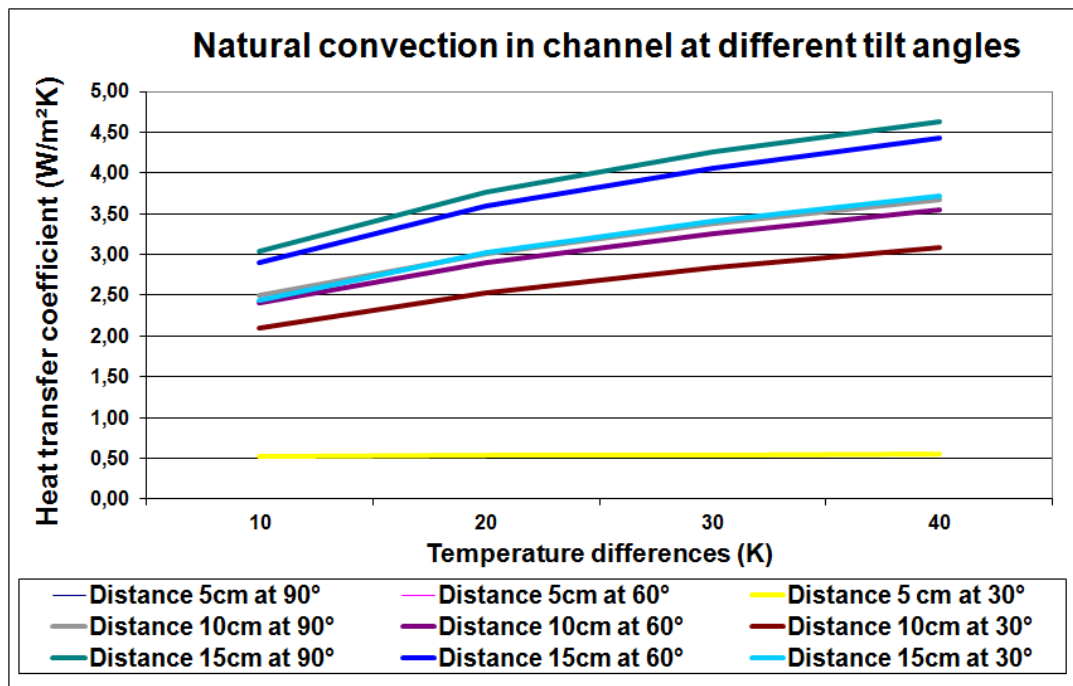


**Figure 7-4 Heat transfer coefficient of natural convection in channels at different distances and tilt angles.**

Figure 7-4 explains the heat transfer coefficient of the natural convection at different temperature differences. This evaluation is based on different gap distances, from 5 – 15 cm, and different tilt angles, from vertical (90°) to horizontal (0°), and for module height 2m and module width 1.2 m. The convection heat transfer increases with temperature differences. The heat transfer coefficient at a 90° vertically tilted angle is higher compared to that at other tilted angles. Compared to other gap distances, the gap distance of 5 cm exhibits a significant reduction in the heat transfer coefficient.

As described in Figure 3-9, the heat transfer coefficient could be seen as the conduction heat transfer coefficient at 5 cm channel distance, wherein the channel distance ( $d$ ) over module length ( $l$ ) is lower than 0.0437. Although the  $d/l$  is lower than 0.109 at a channel distance of 15 cm, the heat transfer coefficient could still be assumed as natural convection without channels due to  $Gr \cdot Pr > 2 \times 10^5$ . M. Ciampi also concluded that energy saving increases as the air channel width  $d$  rises. Nevertheless, such a rise turns out to be particularly limited by  $d < 15$  cm. The use of carefully designed ventilated facades will allow, in the summer cooling of buildings, an energy saving that can even exceed 40% [M.Ciampi-2003].

In order to design the optimum cooling effects of BIPV and achieve the optimum structure construction costs, the air channel width and module length, therefore, have to be taken into account under consideration of these boundary conditions ( $d/l > 0.109$  and  $Gr \cdot Pr > 2 \times 10^5$ ).

## 7.2 Thermal relevant building function

For the determination of these parameters, the accurate values of the external and internal heat transfer coefficients ( $h_i$ ,  $h_e$ ), and the heat transmission coefficient in cavity ( $h_s$ ) are necessary.

In order to determine or identify these coefficients, Table 7-1 describes both summer and winter boundary conditions [EN-410 and EN-13363-2]. These coefficients depend on the operating temperature, surface temperature of the component, ambient temperature, tilt angle, emissivity of surface and the wind speed. The standard values of internal and external heat transfer coefficients can be obtained by EN410 and EN13363-2, while the heat transmission coefficient in the cavity ( $h_s$ ) is defined in EN673 and measured in EN674, EN675 and EN12567. These coefficients have been considered under steady state boundary conditions.

By implementing this validated model in the previous chapter for a different PV module together with conventional building products (laminated glass, insulated glass and composite element), the operating temperature, surface temperature and corresponding heat transfer coefficients can be simulated based on winter and summer boundary conditions for identifying these thermal relevant building functions (Table7-2).

Winter (U-value, g-value)	Summer (Fc-value)
<u>Outside</u> <ul style="list-style-type: none"> <li>○ Solar irradiation 300 W/m<sup>2</sup></li> <li>○ Wind speed 4m/s</li> <li>○ Ambient temperature 5°C</li> </ul>	<u>Outside</u> <ul style="list-style-type: none"> <li>○ Solar irradiation 500 W/m<sup>2</sup></li> <li>○ Wind speed 1m/s</li> <li>○ Ambient temperature 25°C</li> </ul>
<u>Inside</u> <ul style="list-style-type: none"> <li>○ Vertical glazing</li> <li>○ Wind speed 0m/s</li> <li>○ Room temperature 20°C</li> </ul>	<u>Inside</u> <ul style="list-style-type: none"> <li>○ Vertical glazing</li> <li>○ Wind speed 0m/s</li> <li>○ Room temperature 25°C</li> </ul>
<u>Heat transfer coefficient</u> <ul style="list-style-type: none"> <li>○ Internal <sup>1)</sup> = 7,7 W/m<sup>2</sup>K</li> <li>○ External <sup>2)</sup> = 25,0 W/m<sup>2</sup>K</li> </ul>	<u>Heat transfer coefficient</u> <ul style="list-style-type: none"> <li>○ Internal <sup>3)</sup> = 2,5 W/m<sup>2</sup>K</li> <li>○ External <sup>4)</sup> = 8,0 W/m<sup>2</sup>K</li> </ul>

**Table 7-1 Boundary conditions for determination U-value, g-value and Fc-value in summer and winter [EN-410, EN-13363-2]**

The deviation in operating temperatures for PV modules is approximately 8-10 °C in winter and about 18-30 °C in summer compared to conventional building products. However, with respect to different PV multi-layered configurations, the deviation of operating temperatures in winter is less varied from 8°C to 10°C, because the influence of ambient temperature mainly takes place at operating temperature. In summer, the deviation in operating temperature is higher, because the influence of solar irradiation is merely at operating temperature, while the influence of ambient temperature is no longer available.

The deviation in the internal heat transfer coefficient ( $h_i$ ) is around -7% to -12% for PV modules compared to conventional building products. In summer, on the other hand, the deviation is much higher, from +17% to +39%. It can also be concluded that the better the thermal insulation of conventional building products, the lower the deviation in the internal heat transfer coefficient.

The external heat transfer coefficients ( $h_e$ ) are quite similar for all configurations of PV-modules and conventional building products, i.e. around 23,5 W/m<sup>2</sup>K in winter. In summer, the deviation in external heat transfer coefficients is around +6% to +10% compared to conventional building products.

Boundary Conditions		Scenario 1			Scenario 2			Scenario 3		
		Laminated glass			Insulated glass			Composite element		
		Glass	PV	Deviation	Glass	PV	Deviation	Glass	PV	Deviation
Operating temperature(°C)	Winter	9,37	17,43	8,06	7,31	17,46	10,15	5,76	16,66	10,9
	Summer	26,08	44,46	18,38	26,35	51,84	25,49	26,66	57,09	30,43
Internal surface temperature(°C)	Winter	9,68	17,49	7,81	14,92	18,87	3,95	19,3	19,83	0,53
	Summer	26,06	43,79	17,73	25,62	36,26	10,64	25,09	26,43	1,34
Internal heat transfer coefficient(h <sub>i</sub> ) (W/m²K)	Winter	7,99	7,01	-12,27%	7,47	6,61	-11,51%	6,40	5,94	-7,19%
	Summer	6,91	9,59	38,78%	6,67	8,84	32,53%	6,06	7,07	16,67%
External surface temperature(°C)	Winter	9,02	16,42	7,4	7,13	16,44	9,31	5,70	15,72	10,02
	Summer	26,04	43,56	17,52	26,29	50,56	24,27	26,59	55,55	28,96
External heat transfer coefficient(h <sub>e</sub> ) (W/m²K)	Winter	23,50	23,58	0,34%	23,48	23,58	0,43%	23,47	23,57	0,43%
	Summer	12,27	13,01	6,03%	12,28	13,30	8,31%	12,29	13,51	9,93%
Heat transfer coefficient in cavity(h <sub>s</sub> )	Winter	0,0075	0,0075	0,00%	0,2030	0,1920	-5,42%	3,0379	3,0379	0,00%
	Summer	0,0075	0,0075	0,00%	0,1810	0,1590	-12,15%	3,0379	3,0379	0,00%

**Table 7-2 Operating temperature, surface temperature and thermal parameters of different PV multi-layered configuration as well as %-deviation in comparison with conventional building products.**

The values in winter are much higher than in summer, because the wind speed or forced convection has a major effect on the external heat transfer coefficient. With a higher wind speed of 4m/s in winter, the influence of forced convection represents around 99% of the heat transfer coefficient. Therefore, the deviation in the heat transfer coefficient is quite low.

In laminated glass and the composite element, the heat transfer resistivity is quite constant and independent from temperature differences. For insulated glass, the heat transfer resistivity in the cavity is -5% and -12% in winter and summer, respectively. With an increasing operating temperature, the heat transport will increase and leads to a lower heat transfer resistivity in the cavity.

With respect to new thermal parameters in Table 7-2, along with equations 2.2, 2.4, 2.5 and 2.6, the relevant building functions (U-, g- and Fc-Values) can be further evaluated under consideration of PV cell coverage. Figure 7-5 represents the calculation methods for identifying the U-value and secondary heat dissipation toward the interior under consideration of a percentage of PV cell coverage. At the transparent area, the thermal parameters of the conventional glazing will be taken into account, while the new thermal parameters will be considered at PV cell coverage area [Henze-2009].

$$q_i = \left[ \alpha_{glas} \cdot \left( \frac{h_{Glas,i}}{h_{Glas,i} + h_{Glas,e}} \right) \cdot \frac{A_{Glas}}{A_{Modul}} \right] + \left[ \alpha_{PV} \cdot \left( \frac{h_{PV,i}}{h_{PV,i} + h_{PV,e}} \right) \cdot \frac{A_{PV}}{A_{Modul}} \right]$$

$$\frac{1}{U} = \left[ \left( \frac{1}{h_{Glas,e}} + \frac{d_i}{\lambda_i} + \frac{1}{h_{Glas,i}} \right) \cdot \left( \frac{A_{Glas}}{A_{Modul}} \right) \right] + \left[ \left( \frac{1}{h_{PV,e}} + \frac{d_i}{\lambda_i} + \frac{1}{h_{PV,i}} \right) \cdot \left( \frac{A_{PV}}{A_{Modul}} \right) \right]$$

**Figure 7-5 Calculation methods for identify the U-value and secondary heat transfer coefficient emitted inside under consideration of percentage of PV cell coverage**

Table 7-3 shows the U-values of the PV modules under the consideration of the different PV multi-layered configurations and a percentage of PV cell coverage along with the standard values from the manufacturer's specification. The calculations of these standard values are based on normative coefficients of conventional glazing. ( $h_i$  and  $h_e = 7,7$  and  $25 \text{ W/m}^2\text{K}$ ).

With respect to the difference between the outdoor ( $5^\circ\text{C}$ ) and indoor ( $20^\circ\text{C}$ ) temperatures, the U-value will only be considered under winter conditions. The difference between outdoor ( $25^\circ\text{C}$ ) and indoor ( $25^\circ\text{C}$ ) temperatures in summer is zero. In winter, the U-values decrease for all PV modules configuration, up to -8.48% for laminated glass when comparing the manufacturer values and the PV module with a PV coverage of 95%. The better the thermal insulation of conventional building products, the lower the deviation of U-values.



PV-Coverage	U-Value		
	Laminated glass	Insulated glass	Composited element
	Winter	Winter	Winter
Manufacturer-Values	5,7	2,7	0,312
0% (no PV)	5,707	2,635	0,309
50%	5,438	2,614	0,308
55%	5,412	2,612	0,308
60%	5,387	2,610	0,308
65%	5,362	2,607	0,308
70%	5,337	2,605	0,308
75%	5,313	2,603	0,308
80%	5,288	2,601	0,308
85%	5,264	2,599	0,308
90%	5,240	2,597	0,308
95%	5,217	2,595	0,308
% Deviation from Manufacturer-Values	-8,48	-3,90	-1,32
% Deviation from building products (no PV)	-8,59	-1,54	-0,35

**Table 7-3 Comparison of simulated heat transfer coefficient (U-value) of different PV multi-layered configurations under consideration of new PV-specific thermal parameters and different percentage of PV cell coverage based on a validated model**

In order to utilize the solar energy in winter periods and protect the solar energy in summer, the solar heat gain coefficient (g-value) and solar reduction factor (Fc-value) have been simulated together with their boundary condition as defined in chapter 2.2. Table 7-4 represents the simulated solar heat gain coefficient (g-values) in summer and winter for different PV multi-layered configurations with different percentage of PV cell coverage.

PV-Coverage	Laminated glass				Insulated glass			
	g-Value				g-Value			
	Winter		Summer		Winter		Summer	
	old	new	old	new	old	new	old	new
0%	0,826	0,826	0,826	0,840	0,702	0,698	0,702	0,724
50%	0,529	0,516	0,529	0,611	0,467	0,447	0,467	0,542
55%	0,500	0,485	0,500	0,588	0,444	0,422	0,444	0,524
60%	0,470	0,454	0,470	0,565	0,420	0,397	0,420	0,505
65%	0,440	0,423	0,440	0,542	0,397	0,372	0,397	0,487
70%	0,410	0,392	0,410	0,519	0,373	0,347	0,373	0,469
75%	0,381	0,361	0,381	0,497	0,350	0,322	0,350	0,451
80%	0,351	0,330	0,351	0,474	0,326	0,297	0,326	0,432
85%	0,321	0,299	0,321	0,451	0,303	0,272	0,303	0,414
90%	0,292	0,268	0,292	0,428	0,279	0,247	0,279	0,396
95%	0,262	0,237	0,262	0,405	0,256	0,222	0,256	0,378
% Deviation from new and old parameters	-9,45		54,54		-13,16		47,65	

**Table 7-4 Comparison of simulated solar heat gain (g-value) in winter and in summer under consideration of new PV-specific thermal parameters and different percentage of PV cell coverage based on validated model**

In winter, the solar heat gain coefficient (g-value) for PV modules at a PV coverage of 95% with new thermal parameters becomes lower compared to that with old or normative parameters (-9.45% for PV laminated glass and -13.16% for insulating glass). That means the amount of solar heat gain in winter is lower than expected. Likewise, in summer, the solar heat gain (g-value) for PV modules, at a PV coverage of 95% with new thermal parameters, is higher than that with old or normative parameters (+54.54% for laminated glass and +47.65% for insulating glass). Therefore, the amount of solar irradiation that can be emitted inside the room is more than expected [Misara-2011a].

### **7.3 Mechanical Behaviour**

The numerical simulation aims at predicting the mechanical behaviour of laminated glass. Critical issues are the temperature, load duration, type of multilayer laminated glass, and type of the interlayer. Therefore, different load scenarios are needed.

#### **7.3.1 Load scenarios**

Wellershoff has developed the new load scenarios for static calculation on different operating temperature and load duration [Wellershoff-2007]. The scenarios are based on gust wind speed and ambient temperature from DWD-Data from 1970 – 1998 together with his measurement of interlayer temperature of laminated glass with black screen printing glass. The different wind loads can be applied to its corresponding operating temperature of BIPV module. Along with other mechanical loads of snow and own loads, Table 7-5 represents the load scenarios for the numerical simulation. The operating temperature can be classified into 5 scenarios from 0°C to 80°C. In each operating temperature scenario, there are 3 sub-scenarios of different load durations with a corresponding wind load. In addition, the snow and own loads are also considered under each operating temperature scenario. For instance;

- scenario 1.1 represents the PV module at an operating temperature of 0°C together with a mechanical load of 25% wind load, 100% snow load and 100% own load
- scenario 5.5 exhibits the PV module at an operating temperature of 80°C together with a mechanical load of 32% wind load, 0% snow load and 100% own load

Load Scenarios	Operating Temperature	Wind Load (%) (of $w_{max}$ )				Snow Load (%) (of $s_{max}$ )	Own Load (%)
		4 days	10 min	3 sec			
		_1	_2	_3			
1	0 °C	25.0%	50.0%	100.0%	+	100.0%	100.0%
2	0 °C	25.0%	50.0%	100.0%		0%	100.0%
3	20 °C	25.0%	50.0%	100.0%		0%	100.0%
4	50 °C	12.5%	25.0%	50.0%		0%	100.0%
5	80 °C	8.0%	16.0%	32.0%		0%	100.0%

$w_{max}$  = maximum wind load from EN 1991 or DIN 1055

$s_{max}$  = maximum snow load from EN 1991 or DIN 1055

**Table 7-5 Wind load scenarios for the design of laminated glass**

For this numerical simulation, the module dimension was assumed to vary from 500 mm – 2500 mm in both length and width with a multi-layered configuration of 3-0.76-3 mm (front glass, interlayer and back glass). The maximum load scenario was taken from an industry roof with an inclination of 10° from horizontal at 12 m height. The PV module was mounted with a 4-sided mounting system. The location of the building was at wind zone 3 and snow zone 4, as defined in EN 1991, representing maximum wind and snow loads of -2.09 kN/m<sup>2</sup> (pull) and +0.88 kN/m<sup>2</sup> (push), respectively. The own load of this laminated glass is +1.66 kN/m<sup>2</sup> (push).

### 7.3.2 Mechanical evaluation

In order to evaluate the mechanical behaviour of the BIPV Module, the numerical validated model in the previous chapter is determined while considering the operating temperature and load duration. For each analysis, the bending stress and deflection, using glass dimension as the domain, will be evaluated.

Temperature dependency: In Figure 7-6a and 7-6b, the bending stresses and deflection are compared with regard to the different operating temperature of the laminated glass. For a BIPV module at a 60°C operating temperature, the bending stress and deflection are greater compared with a 40°C operating temperature. This is due to the lower elasticity of the interlayer at a higher operating temperature. The bending stress and deflection of laminated glass increase dramatically at an increasing temperature over the glass transition temperature ( $T_g$ ) of the interlayer.

Load duration dependency: The load duration dependency gives a clearer picture of the phenomenon of the increasing bending stress and deflection over the period of exposure. Figure 7-6c and 7-6d describes the difference in mechanical properties with regard to the different load duration. For the BIPV Module with a 4 day load duration, the bending stress and deflection are greater compared to a 3-second load duration. It represents the creep characteristics of the interlayer materials. Therefore, the bending stress and deflection increase with a longer load duration.

These temperature and load duration dependencies agreed well with the theoretical creep and storage modulus characteristics and the computational results [Misara-2011b].

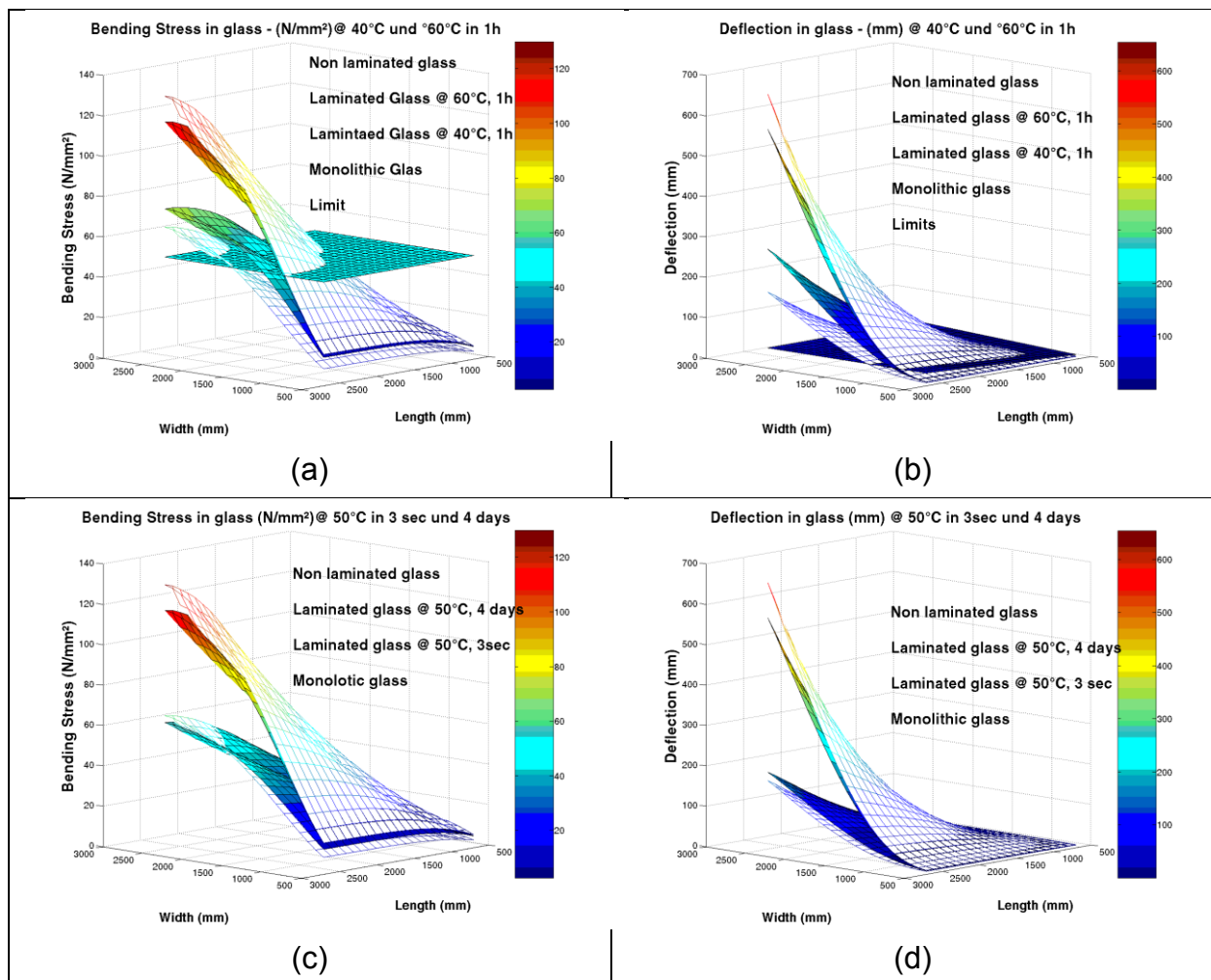


**Figure 7-6 Bending stress and deflection of laminated glass with PVB interlayer at different operating temperature and load duration; Dependency on operating temperature (a, b), Dependency on load duration (c, d)**

Characteristics under different load scenarios: The set of results from different scenarios are compared using all the data collected. Figure 7-7 represents the series of scenarios of monolithic glass and laminated glass. The maximum bending stress for monolithic glass can be found under scenario 1.1 (at 0°C, 4 days, wind and snow loads), whereas the maximum bending stress for laminated glass could be found under scenario 5.1 (at 80°C, 4days, wind load). It can be concluded that, in contrast to monolithic glass, the mechanical behaviour tendency of laminated glass cannot be assumed.

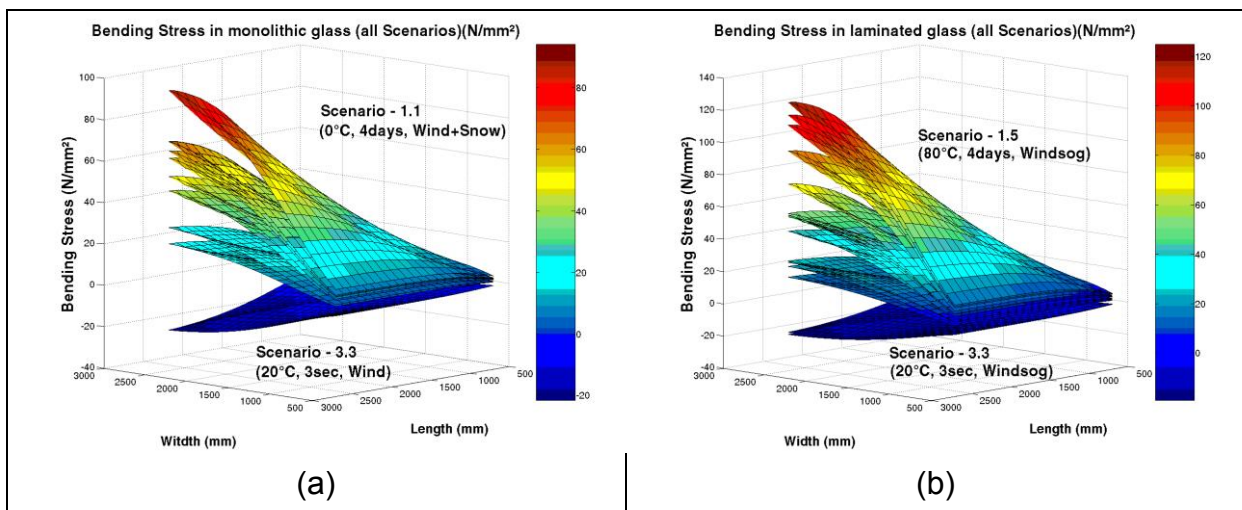


**Figure 7-7 Bending stress of monolithic glass (a) and laminated glass (b) under different load scenarios.**

Interlayer dependency at low operating temperature: In order to closely evaluate the operating temperature dependency on the mechanical behaviour of the laminated glass, a simulation of bending stress and deflection at low operating temperature is determined. At an operating temperature of 0°C, the bending stress and deflection decrease for both laminated glass with PVB and EVA. It also shows better mechanical behaviour than the monolithic glass due to a higher shear modulus of interlayers (Figure 7-8).

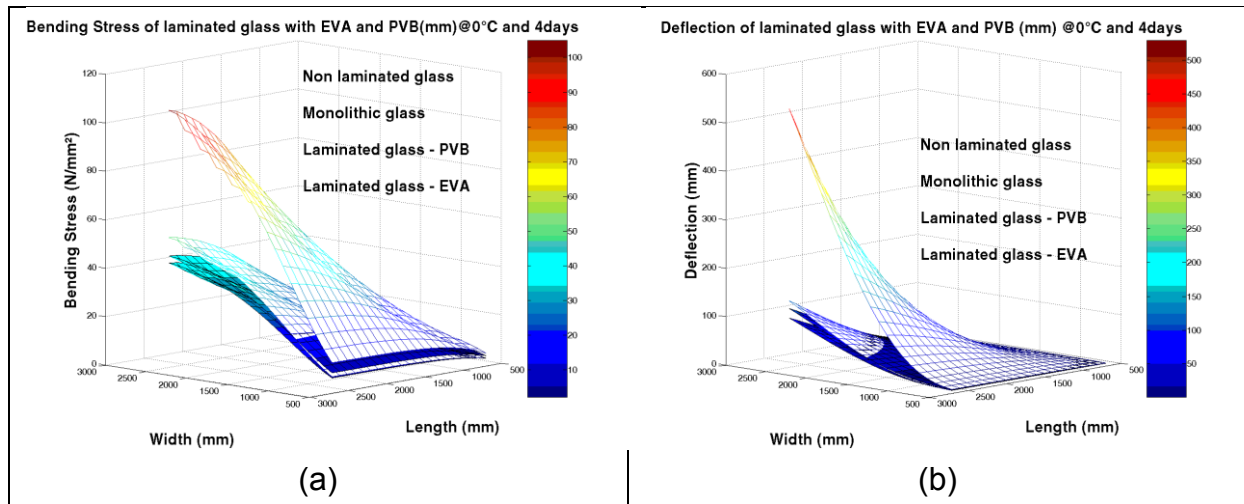


**Figure 7-8 Bending stress and deflection of laminated glass with PVB and EVA interlayers at low operating temperature; (a) bending stress, (b) deflection**

Interlayer dependency at high operating temperature: Contra to a low operating temperature, the computed bending stress and deflection of the laminated glass at a high operating temperature show a reduction in mechanical behaviour, representing the effect of the elasticity of the interlayer materials. The laminated glass with EVA shows much better mechanical behaviour than laminated glass with PVB-interlayer due to lower elasticity of PVB interlayer compared to EVA-interlayer at higher temperature (Figure 7-9a, 7-9b).

Interlayer dependency with different load duration at high operating temperature: With respect to a long load duration at a higher operating temperature, the laminated glass with an EVA-interlayer shows much better mechanical behaviour than with PVB-interlayer due to the better creep characteristic of the EVA-interlayer compared to the PVB-interlayer (Figure 7-9c, 7-9d).

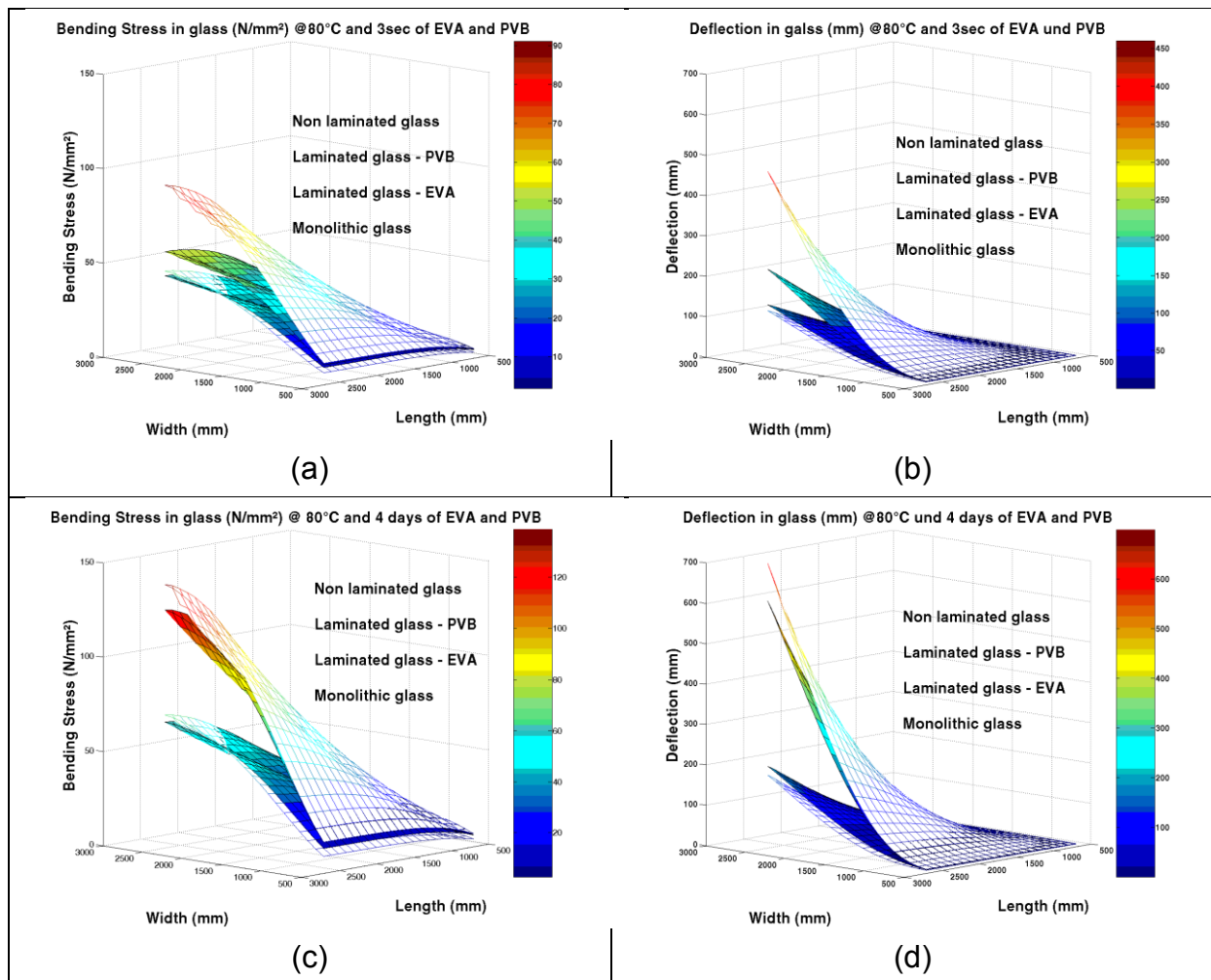


**Figure 7-9 Mechanical behaviors (bending stress and deflection) of laminated glass with EVA and PVB interlayers at high operating temperature; with short load duration (a, b), with long load duration (c, d)**

## 7.4 Software development

Since the thermal and mechanical models have been validated and further evaluated based on different boundary conditions, the corresponding software has been developed with the support of colleagues so that manufacturers can easily simulate the relevant thermal and mechanical building functions of BIPV modules.

### 7.4.1 PV-Therm

Figure 7-10 exhibits the graphic user interface of thermal relevant building functions, the so-called PV-Therm. Users can provide the different glass configuration, glass thickness, module dimension, PV cell efficiency, PV cell coverage and temperature co-efficiency of PV cell. In the case of glass configuration, the laminated glass and insulated glass can be given together with the emission grade of the glass surface.



Moreover, summer and winter boundary conditions can also be evaluated. Finally the thermal relevant building functions, U-value and G-value, can be simulated in comparison to conventional glazing without a PV-cell. In addition, the simulation protocol can also be generated.

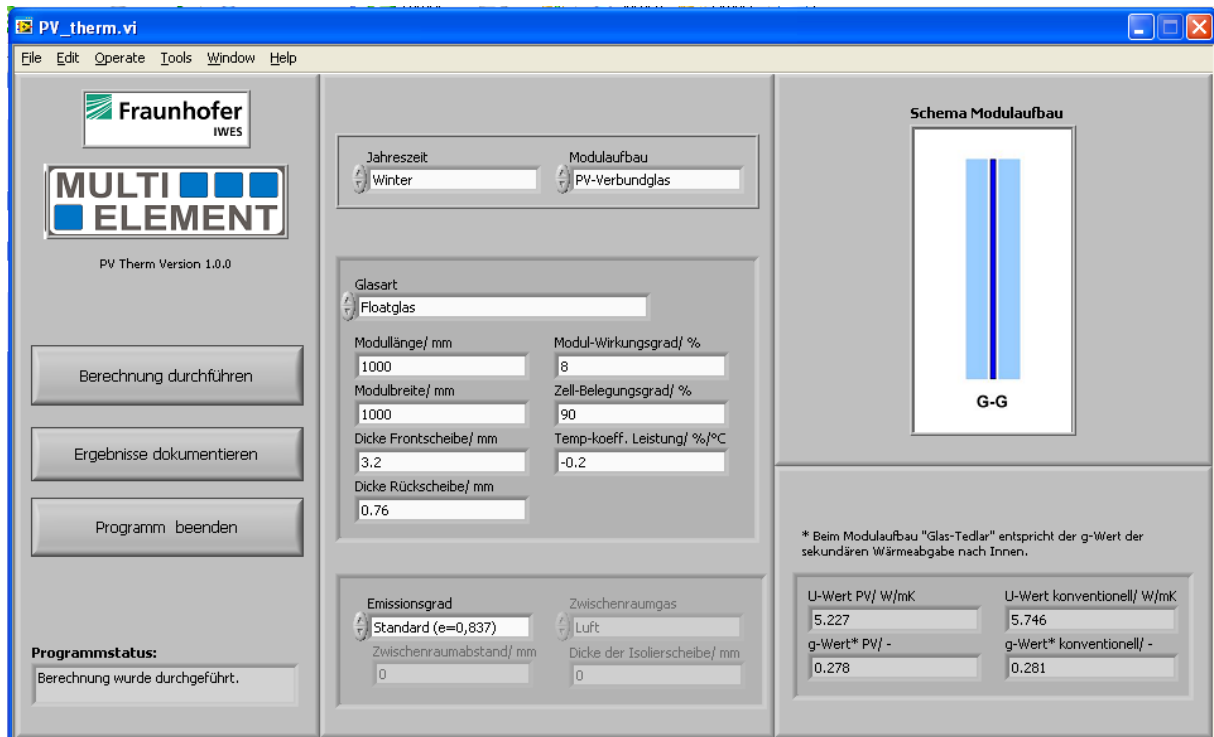


**Figure 7-10 Graphic user interface of thermal relevant building function software (PV-Therm)**

#### 7.4.2 PV-Mech

Figure 7-11 presents the graphic user interface of mechanically relevant building functions under consideration of different operating temperatures and load duration scenarios, so-called PV-Mech. Users can provide the types of mounting system, types of interlayer, module dimension, glass thickness and mechanical load. In the case of the mounting system, only a standard-conform mounting system can be simulated. At the same time, the bending stress and deflection of a certain multi-layered configuration can also be displayed, Figure 7-12.



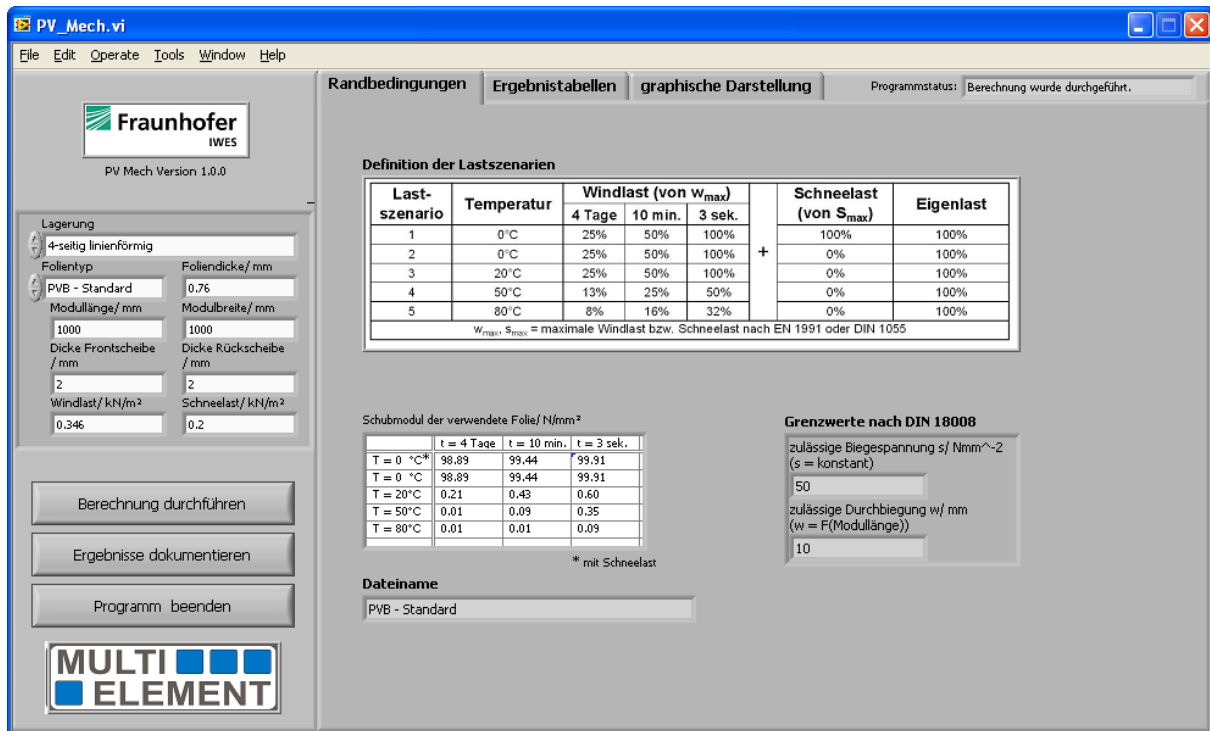


Figure 7-11 Graphic user interface of mechanical relevant building function software (PV-Mech)

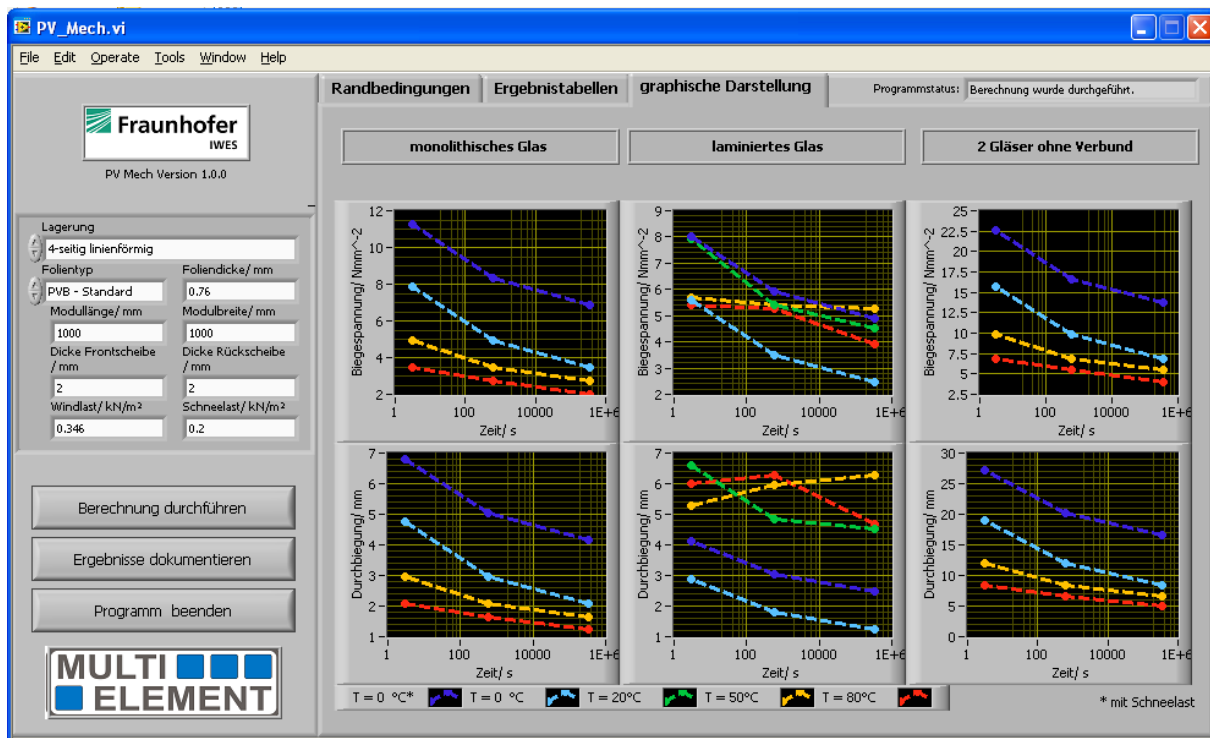


Figure 7-12 Display of bending stress and deflection of certain multi-layered configuration.

## 8 Conclusion

In BIPV application, electrical parameters as well as other relevant building functions have to be taken into account. BIPV applications have to fulfill the requirements of the Construction Production Directive [CPD-89/106-EEC]. In this work, the ‘mechanical resistance and stability’ and ‘energy economy and heat retention’ are considered together with the electrical aspect of BIPV. With respect to the higher operating temperature of BIPV modules compared to conventional building products, all behaviors mentioned above have been changed.

The electrical parameter is influenced mainly by a non-optimally tilted angle and multi-layered module configuration of BIPV applications. The non-optimally tilted angles lead to a higher reflection loss and lower power input to the PV module, while the multi-layered module configuration leads to higher heat conduction resistance, lower surface temperature and corresponding lower power dissipation. In this case, the surface temperature of the module could not be assumed to be equal to the cell temperature as in standard PV modules. This power dissipation can be divided into radiation and convection dissipation, influenced by temperature differences between the surface, surroundings and emission grade of the surface, tilted angle, etc. With lower power dissipation, the higher operating cell temperature is obtained, which leads to a lower module efficiency and lower power output, respectively. In order to predict the real-time power output for energy management application, moreover, the existing implicit and explicit models are not applicable to the BIPV module due to its module heat capacity. It leads to a time-delay of operating temperature and corresponding power output. In order to solve this time-delay operating temperature, the iteration method has to be considered together with its module heat capacity.

The internal and external heat transfer coefficients ( $h_i$  and  $h_e$ ) at PV-Module’s surfaces and heat transfer coefficient in cavity ( $h_s$ ) are the most significant factors in determining the relevant building functions of thermal insulation (**U**-value), solar heat gain (**g**-value) and solar shading (**Fc**-value) of BIPV-modules. They are influenced by surface temperature and the corresponding heat conduction resistance ( $R_{cond}$ ) of multi-layered module configurations. In this case, the module heat capacity ( $C_M$ ) has not been considered because the building functions are considered only under a steady state condition. It needs to be considered for dynamic state condition for real-time building simulation applications.

The mechanical behaviors were defined by bending stress and deflection. The manufacture of PV modules is mostly based on laminated glass configuration.

Therefore, the shear modulus of interlayer used is the most important factor that affects the mechanical behaviour of the PV module. It is influenced by the operating temperature, load amount and load duration. At the same time, the mounting system is also another critical factor for identifying the mechanical behaviour of the PV module. Hence, in this work, the mechanical behaviour has been evaluated based on different load scenarios, operating temperature, load duration and different mounting systems.

In this work, the power balance modeling has been developed based on the iteration method for electrical and thermal evaluation, and the mechanical modeling has been further developed for mechanical evaluation of BIPV modules.

The outdoor and indoor test infrastructures have been developed by validating the models above. For outdoor test infrastructures, the solar irradiation measurement and real-time outdoor PV module measurement have been applied in order to evaluate the input power and thermal power dissipation of the PV system, respectively. For the input power evaluation, the available inclined solar irradiation conversion modeling and distribution of solar irradiation at different tilted angles have been considered. In indoor test infrastructures, the PV variable mounting system and mechanical testing equipment have been developed together with the new test method of back-bias current concept. With the back-bias current concept, the thermal power can be emulated from the solar irradiation, which is not converted into electrical power. With a PV variable mounting system, the power dissipation of the BIPV module can be further validated based on variable tilted angles and multi-layered configurations. At the same time, the mechanical behaviour of the BIPV module can be validated with mechanical testing equipment based on variable operating temperature, load duration mounting systems.

In terms of the power input of PV system, the Hay inclined conversion model has proven to be the most appropriate. To evaluate the operating temperature and power output in following works, however, the applied models seem to be less accurate under these conditions. Therefore, with respect to additional reflection and spectrum losses, the direct measurement by solar cell sensors will be used as power input for the PV modules. For the distribution of solar irradiation at different tilted angles, the distribution in the weak-light range has been increased from 23%, based on European Efficiency (EN50530), to 47% for BIPV application at a 90° tilt angle for east and west orientation. Therefore, the reduction of module efficiency in the weak-light range has to be taken into account properly.

With a good correlation of simulated and measured results in the real-time outdoor PV module measurement and PV variable mounting system test infrastructures, it can be concluded that the operating temperature and thermal power dissipation have been correctly considered in the development of the power balance model. As for the test results, the thermal parameters and corresponding calculation methods of thermal relevant building functions in existing building codes are not applicable to BIPV modules, because the higher operating temperature of the BIPV module has not been considered. Therefore, new thermal parameters and calculation methods are needed for active building products, such as BIPV modules. With respect to higher heat capacity, the existing operating temperature or power prediction models are not applicable for BIPV applications, especially with short time resolution measurement. The time-delay of the operating temperature has not been considered. Therefore, the power balance model together with iteration methods is necessary in order to predict the real-time power output or operating temperature.

With a standard-conform mounting system with laminated glass module configuration, the mechanical model exhibits a good correlation to measurement under different load scenarios. However, this mechanical model is not applicable for other manufacturer specific mounting systems. Therefore, the new parameters for the modelling have to be re-configured. In the glass-backsheet module configuration, the bending stress measurement with strain is not applicable due to the plastic characteristics of the backsheet material. For these measurements, it can be further concluded that the bending stress measurement with strain gauge is only applicable on glass material, while the deflection measurement with displacement sensor is applicable for all multi-layered configuration.

Since the power balance model has been validated, the thermal power dissipation seems to be very important for the electrical and thermal behaviour of BIPV modules. In this case, the thermal power dissipation via radiation mainly depends on the emissivity of material used and slightly on temperature differences, not on front- and backside of PV module or different tilt angles. In terms of thermal power dissipation via convection, the amount of power dissipation through natural convection is quite comparable to that of forced convection with a wind speed lower than 1.0 m/s. With regard to the wind speed measurement, a wind speed lower than 1 m/s represented more than 50% of total wind speed. On the backside of the PV module in the IPV application, moreover, the natural convection is mainly occupied. Therefore, natural convection plays a major role in thermal power dissipation. For the standard PV-laminated glass module with same solar irradiation, the operating temperature of the horizontal PV module is higher compared to that of the vertical PV module due to

lower total heat transfer coefficients. For PV modules as integrated building products, however, the operating temperature of a horizontal PV module is lower compared to that of a vertical PV module due to the thermal power dissipation which is available only at the front-side. With respect to buoyancy forced in natural convection, the more the angle of a vertical to horizontal installation is tilted, the higher the total heat transfer coefficient and thermal power dissipation. For the ventilation behind the PV module, the conduction heat transfer coefficient is considered. This is in the case of a channel distance ( $d$ ) / module length ( $l$ ) smaller than 0.0437. If  $d/l$  is higher than 0.109, the free natural convection without a channel can be assumed. In case  $d/l$  lies between 0.0437 and 0.109, the natural convection within channel is needed. This aspect is very important for the mounting system design in order to optimize the cost of construction with the power output of a PV system.

In terms of thermally relevant building functions, the solar heat gain coefficient ( $g$ -value) of the PV modules with new thermal parameter is lower compared to those with normative parameters for both PV laminated glass and PV-insulated glass in winter. That means the amount of solar heat gained in winter is lower than expected. Likewise, the solar heat gain ( $g$ -value) of the PV modules with new thermal parameters is higher in summer compared to those with normative parameters for both PV-laminated glass and PV-insulated glass. That means more solar irradiation can be emitted inside the room than expected. At the same time, the  $U$ -values, with new thermal parameters, are lower for all PV modules configuration compared to those with normative thermal parameters during the winter period. Moreover, the better the thermal insulation provided by conventional building products, the lower the deviation of the  $U$ -value between new thermal parameters and normative thermal parameters.

Since the mechanical models have been validated, the most-used interlayers in building products and PV modules can be further evaluated; these are PVB and EVA, respectively. At a lower operating temperature, both laminated glass with EVA or PVB interlayers have better mechanical behavior than monolithic glass. On the other hand, laminated glass with an EVA-interlayer shows better mechanical behavior than with PVB-interlayer at a higher operating temperature due to lower storage module reduction. Laminated glass with an EVA-interlayer shows much better mechanical behavior than with PVB-interlayer due to lower creep characteristics, particularly at a longer load duration. Therefore, it has been proven that EVA can be used as a laminated safety glass in building applications.

Finally, so that manufacturers can simulate the relevant thermal and mechanical building functions of their BIPV modules, simulation software has been developed.

## 9 Outlook

Since the electrical, thermal and mechanical characteristics of BIPV have been evaluated, further works are still needed in order to reduce the technical and market barriers of BIPV applications.

In terms of electrical characteristics, the iteration methods of power balance concepts can be further developed in order to reduce the simulation time. This can be achieved by employing other mathematical methods, for example Euler, Runge Kutta methods. With respect to the overload of the PV system in grid integration, the self-consumption of the PV system has been introduced by balancing the PV power output with power consumption locally via an energy management algorithm. Regarding new developments in the Bidirectional Energy Management Interface (BEMI) by Fraunhofer IWES, this power prediction model based on a power balance concept can be further developed together with available solar irradiation forecasting models in order to provide the real-time power output of BIPV modules to BEMI. This can be implemented as the application runs on BEMI.

For thermal characteristics of the BIPV module, the back-bias current concept needs to be further validated with existing measurements in order to provide the cost-saving methods and emulate the actual characteristics of the BIPV module. As active building products generating electricity for the BIPV module, the PV-specific thermal parameters and calculation method need to be re-considered in building codes for the identification of thermally relevant building functions (TC129-WG9), especially the heat transfer coefficient of the gap behind the PV modules in EN6496. Afterwards, the calculation of energy efficiency or energy saving regulations has to consider the BIPV module with new values of PV-specific building functions. With a lower roof surface temperature in PV-on-roof and in-roof application compared to the roof without PV-module, moreover, the energy saving aspect could be considered. With a real-time power balance model, the real-time building function can also be considered in a real-time building simulation in order to simulate the real-time energy consumption. This can be used again to locally balance the energy consumption with energy generation by PV modules. In a mounting system designed for BIPV application, the optimization between the amount of heat dissipation and construction costs have to be investigated together with the cost of PV modules.

In terms of mechanical behaviour, firstly, the bonding characteristics of a new interlayer used in PV-modules have to be investigated on both temperature and load duration dependencies. In order to provide the mechanical behaviour of PV module,

the mechanical modeling, PV-Mech, has to be re-configured with the characteristics of new interlayers. However, this calculation is still based on standard-conform mounting systems. With respect to existing manufacturers' mounting systems in the market, the manufacturer-specific parameters,  $k_1$  and  $k_2$  in table 4.4, have to be re-defined. Furthermore, the bonding characteristics of the interlayer have to be considered by static calculation of a PV module in the building regulation and building codes, like TC129-WG8. According to the mechanical characteristics, laminated glass is completely different compared to monolithic glass. Therefore, the load scenarios of different operating temperature and load duration have to be considered by the static calculation of PV module.

In order to identify the long-term performance of the BIPV module, electrical parameters as well as thermal and mechanical parameters should be considered in long-term outdoor measurement. The thermal and mechanical long-term performance of PV modules can be achieved with heat-flux plate and displacement sensors, respectively.



## 10 Reference

- Armstrong-2010      S. Armstrong, W.G. Hurley, A thermal model for photovoltaic panels under varying atmospheric conditions, *Applied Thermal Engineering* Volume 30, Issues 11–12, August 2010, Pages 1488–1495
- Ayompe-2010      L.M. Ayompe, A. Duffy, S.J. McCormack, M. Conlon, Validated real-time energy models for small-scale grid-connected PV-systems, *Energy*, Volume 35, Issue 10, Pages 4086–4091, October 2010
- Bennison-1999      Bennison, S. J., Davies, A., Jagota, A., Van Duser, C., Smith, R., *Structural Performance of laminated safety glass*. (1999).
- Bhati-2009      Ruhi Bharti, Joseph Kuitche, Mani G. Tamizh-Mani, Nominal Operating Cell Temperature (NOCT): Effects of Module Size, Loading and Solar Spectrum – IEEE 2009
- Blackburn-2012      G. Blackburn, F. Vignola; Spectral distribution of diffuse and global irradiance for clear and cloudy periods, 2012
- Bloem-2008      Bloem JJ. Evaluation of a PV-integrated building application in a well controlled outdoor test environment. *Building and Environment* 2008;43: 205–16.
- Breteque-2009      E.A. de la Breteque, 2009, Thermal aspects of c-Si photovoltaic modul energy rating, *Solar Energy* 83 (2009) 1425-1433
- Brinkworth-2000      B.J. Brinkworth, R.H. Marshall, Z. Ibarahim, A validated model of naturally ventilated PV cladding, *Solar Energy*, Volume 69, Issue 1, 2000, Pages 67–81
- Bucak-2006      Bucak, Ö., Schuler, C., Meißner, M. “Verbund im Glasbau – Neues und Bewährtes. In: *Stahlbau*, Nr. 6, 2006.
- Burger-2009      B. Burger, H. Schmidt, B. Goeldi, B. Bletterie, R. Bruendlinger, H. Häberlin, F. Baumgartner, G. Klein; “Are We Benchmarking Inverters on the Basis of Outdated Definitions of the European

& CFC Efficiency?”, 24th European Photovoltaic Solar Energy Conference, Hamburg, 2009

- Charron-2006      Rémi Charron, Andreas K. Athienitis, Optimization of performance of double-facades with integrated photovoltaic panels and motorized blinds, Solar Energy, Volume 80, Issue 5, Pages 482–491, May 2006
- Ciampi-2003      M. Ciampi, F. Leccese, G. Tuoni; Ventilated facades energy performance in summer cooling of buildings; Solar Energy, Volume 75, Issue 6, December 2003, Pages 491–502
- CPD-89/106/EEC      Construction Products Directive (CPD) – Directive 89/106/EEC
- CSP-2011      Fraunhofer CSP, Shear Modulus of EVA-Interlayer, Personal Communication, 2011
- Cucumo-2006      Cucumo M, De Rosa A, Ferraro V, Kaliakatsos D, Marinelli V. Performance analysis of a 3 kW grid-connected photovoltaic plant. Renew Energy 2006; 31(8):1129e38.
- Davis-2001      M.W. Davis, B.P. Dougherty, A.H. Fanney. Prediction of Building Integrated Photovoltaic Cell Temperatures, Journal of Solar Energy Engineering, Vol. 123, pp. 200-210 August 2001
- DGS-2008      Planning and installing photovoltaic systems: a guide for installers, architects, and engineers / Deutsche Gesellschaft für Sonnenenergie (DGS). - 2nd ed., Page 13, ISBN-13: 978-1-84407-442-6
- Diaz-2010      Oscar Mauricio Diaz Duarte, Untersuchungen zum Tragverhalten von photovoltaischen Elementen, 2010
- Dietrich-2009      Dietrich, S., Pander, M., Ebert, M., “Mechanical challenges of PV-modules and its embedded cells – experiment and finite element analysis”, 24<sup>th</sup> European Photovoltaic Solar Energy Conference, Hamburg, Germany, 21-25 September 2009,

- Dietze-1957      Dietze, Gerhard: Einführung in die Optik der Atmosphäre. Akademische; Verlagsgesellschaft Geest & Portig K.G., Leipzig, 1957.
- Duffie-2006      John A Duffie, William A Beckman, Solar Engineering of Thermal Processes, Volume: 53, Issue: 4, Publisher: Wiley, Pages: 760, ISBN: 0471698679
- Durisch-2007      Durisch W, Bitnar B, Mayor J-C, Kiess H, Lam K-h, Close J. Efficiency model for photovoltaic modules and demonstration of its application to energy yield estimation. Solar Energy Materials and Solar Cells 2007; 91:79–84.
- Eitner-2010      Eitner, U., Kaiari-Schröder, S., Köntges, M., Brendel, R., “Non-linear mechanical properties of Ethylene-Vinyl Acetate (EVA) and its relevance to thermomechanics of photovoltaic modules”, 25<sup>th</sup> European Photovoltaic Solar Energy Conference, Valencia, Spain, 6-10 September 2010
- Faine-2009      P. Faine, Sarah R. Kurtz, C. Riordan, J.M. Olsen, “The influence of spectral irradiance variations on the performance of selected single-junction and multijunction solar cells”, Solar Cells 31 (1991) 259-278
- Fischer-2003      Fischer, Edgar, Neuorientierung der Anwenderschnittstelle und des Berechnungskerns von dem Simulationsprogramm SolEm, Diplomarbeit an der Fachhochschule München, 2003
- Fossa-2008      M.Forsa, C. Menezo, E. Leonardi, Experimental natural convection on vertical surfaces for building integrated photovoltaic (BIPV) applications, Experimental Thermal and Fluid Science, Volume 32, Issue 4, Pages 980–990, February 2008
- Friesen-2007      G. Friesen, R. Gottschalg, H.G.Beyer, S. Williams, A. Guerin de Montgareuil, N. van der Borg, W.G.J.H.M. van Sark, T. Huld, B. Müller, A.C. de Keizer, Y. Niu, Intercomparison of Different Energy Prediction Methods Within the European Project Performance-Results of the 1st Round Robin, 22nd European

Photovoltaic Solar Energy Conference, Milan, Italy, 3-7 September 2007

- Fuentes-1987 M.K. Fuentes, A simplified thermal model for Flat-Plate Photovoltaic arrays, Technical Report, Sandia National Labs., Albuquerque, NM (USA), 1987
- Geyer-2006 D. Geyer et al., Building Integration of Photovoltaic Thin Film Modules in CIS Technology – Results of the Project HIPERPB, 20<sup>th</sup> European Photovoltaic Energy Conference, 2006
- Glotzbach-2008 Thomas Glotzbach, Dr. Christian Bendel, Björn Schulz, Mike Zehner, Christian Vodermayr, Gerald Wotruba, Maurice Mayer, Round-Robin-Test mit Bestrahlungsstärkesensoren, 23. Symposium Photovoltaische Solarenergie, 05.-07.03.2008, Bad Staffelstein
- Glotzbach-2011 T. Glotzbach, Ein Beitrag zur mathematischen Charakterisierung von Photovoltaik-Dünnschichttechnologien auf Basis realer I/U-Kennlinien, Kassel Univ. Diss. 2010, ISBN-978-3-86219-055-3
- Grunow-2004 P Grunow, S Lust, D Sauter, V Hoffmann, Weak light performance and annual yields of PV modules and systems as a result of the basic parameter set of industrial solar cells, 19th European Photovoltaic Solar Energy Conference, Paris, France, 7-11 June 2004
- Hay-1979 J. Hay; Calculation of monthly mean solar radiation for horizontal and inclined surfaces, Solar Energy 1979, 23:301-307
- HBM-2008 Hottinger Baldwin Messtechnik GmbH, The route to measurement transducers – A guide to use of the HBM K series foil strain gauge and accessories, 2008
- Henze-2009 N. Henze, S. Misara, P. Funtan, T. Glotzbach, M. Roos und B. Schulz, 2009, MULTIELEMENT – Multi-Functional Building-Integrated PV-ATCAE Atlas – Technical Conference on

accelerated Ageing and Evaluation; Phoenix, AZ, December 8-9, 2009

- Jones-2001      A. D. Jones and C. P. Underwood, 2011, A thermal model for photovoltaic system, Solar Energy Vol. 70, No. 4, pp. 349–359, 2001
- Jordan-1963      B.Y.H. Liu, R. C .Jordan, “A rational procedure for predicting the long-term average performance of flat-plate solar-energy collectors”, Solar Energy, 1963
- Kenny-2003      R.P. Kenny<sup>1</sup>, G. Friesen<sup>2</sup>, D. Chianese<sup>2</sup>, A. Bemasconi<sup>2</sup>, and E.D. Dunlop<sup>1</sup>, Energy rating of PV modules: comparison of methods and approach, 6P-D5-02, 3rd World Conference on Photovoltaic Energy Conversion May 11-18. 2003 Osaka, Japan
- King-1997a      King, David L.: Photovoltaic Module and Array Performance Characterization Method for All System Operating Conditions Sandia National Laboratories, 1997
- King-1997b      D.L. King, J.A. Kratochvil, W.E. Boyson , Measuring solar spectral and angle-of-incidence effects on photovoltaic modules and solar irradiance sensors, 26th IEEE Photovoltaic Specialists Conference, Anaheim, California September 29-October 3, 1997
- King-2004      King DL, Boyson WE, Kratochvil JA. Photovoltaic array performance model. Report SAND2004-3535. Available from: <<http://www.sandia.gov/pv/docs/PDF/King%20SAND.pdf>>; 2004.
- Knaup-1997      Knaupp, Werner, 1997, Analyse und Optimierung von Photovoltaik-Modulen Shaker-Verlag, Aachen, 1997
- Klausing-2009      Sebastian Klausing, Mechanisches Verhalten laminierter Sandwich-Strukturen mit integrierten Solarzellenstrings, Bachelorarbeit, Fraunhofer CSP, 2009

- Klucher-1979 T. Klucher, "Evaluation of models to predict insolation of tilted surfaces", Solar Energy 1979: 23:111-114
- Kolhe-2003 Kolhe M, Agbossou K, Hamelin J, Bose TK. Analytical model for predicting the performance of photovoltaic array coupled with a wind turbine in a standalone renewable energy system based on hydrogen. Renew Energy 2003; 28 (5):727e42.
- Koomen-1996 E.A. Sjerps-Koomen, E.A. Alsema, W.C. Turkenburg, A simple model for PV module reflection losses under field conditions, Solar Energy, Volume 57, Issue 6, December 1996, Pages 421–432
- Krawczynski-2010 M.Krawczynski, M.Strobel, C.J.Hibberd, T.R.Betts, R.Gottschalg.; Influence of spectral irradiance measurements on accuracy of performance ratio estimation in large scale PV systems; 25th European Photovoltaic Solar Energy Conference and Exhibition (EUPVSEC), Valencia, pp. 4710 - 4714.
- Krauter-1996 S. Krauter, R. Hanitsch, Actual optical and thermal performance of PV-modules, Solar Energy Materials and Solar Cells 41/42 (1996) 557-574
- Krauter-1999 Stefan Krauter, Rodrigo Guido Araujo, Sandra Schroer, Rolf Hanitsch, Mohammed J. Salhi, Clemens Triebel, Reiner Lemoine, Combined Photovoltaic and Solar Thermal Systems for Facade Integration and Building Insulation, Solar Energy, Vol 67, pages 239-248, 1999
- Kutterer-2005 Kutterer, M., Verbundglasplatten – Schubverbund und Membrantragwirkung – Teil I&II, Stahlbau 74(2005) Heft 1 &2
- Matteil-2006 Mattei M, Notton G, Cristofari C, Muselli M, Poggi P. Calculation of the polycrystalline PV module temperature using a simple method of energy balance. Renew Energy 2006; 31(4):553e67.
- Mei-2009 L. Mei a, D.G. Infield, R. Gottschalg, D.L. Loveday, D. Davies, M. Berry, Equilibrium thermal characteristics of a building

- integrated photovoltaic tiled roof, Solar Energy 83, page 1893-1901, 2009
- Miller-2010 David C. Miller, Michael D. Kempe, Stephen. H. Glick, and Sarah R. Kurtz, Creep in photovoltaic modules: Examining the stability of polymeric materials and components; Photovoltaic Specialists Conference (PVSC), 2010 35th IEEE, ISSN: 0160-8371
- Misara-2009 S. Misara, C. Bendel, P. Funtan, T. Glotzbach, N. Henze, Untersuchungen zur Entwicklung von Fertigungs-, Prüf- sowie Einbaumethoden von multifunktional nutzbaren Photovoltaik Bauelementen/ Baugruppen in der Gebäudetechnik, 24. Symposium Photovoltaische Solarenergie, Staffelstein, 2009
- Misara-2010a Misara, Henze, P. Mazumdar, 2010, Temperaturmodell multifunktionaler PV-Bauelemente: Ergebnisse aus dem Projekt MULTIELEMENT, Bad Staffelstein 2010
- Misara-2010b S. Misara, T. Glotzbach, B. Schulz, P. Biswas, 2010, Weak-light irradiation on BIPV applications: Results of the project MULTIELEMENT, 25th European Photovoltaic Solar Energy Conference and Exhibition Valencia EU-PVSEC - 2010
- Misara-2011a Siwanand Misara, Norbert Henze, Alexander Sidelev, Thermal Behaviour of BIPV Modules (U-value and g-value), ISES Solar World Conference, Kassel, 2011
- Misara-2011b Siwanand Misara, Attasit Pornnimit, Mechanical Behaviour of BIPV Modules under different load scenarios and encapsulation, ISES Solar World Conference, Kassel, 2011
- Nolay-1987 Nolay P. De'veloppement d'une me'thode ge'ne'rale d'analyse des syste'mes photovoltaï'ques. MS Thesis, Ecole des Mines, Sophia-Antipolis, France; 1987.
- Nordmann-2003 Nordmann, T.; Clavadetscher, L., Understanding temperature effects on PV system performance, Photovoltaic Energy

- Conversion, 2003. Proceedings of 3rd World Conference, Osaka Japan, 18-18 May 2003, pages 2243 - 2246 Vol.3
- PV-SOL-2000 Benutzerhandbuch PV-SOL Version 2.1, Dr.-Ing. Gerhard Valentin & Partner GbR, Berlin, 2000
- Perez-1986 Perez, Richard; Stewart, Ronald: Solar irradiance conversion models. Solar Cells; Vol.18, 1986, pp. 213-222.
- Quanschning-1996 V. Quaschnig, Simulation der Abschattungsverluste bei Solarelektrischen Systemen, 1. Aufl. -Berlin. Köster, 1996
- Reidl-1990 D. Reidl, W. Beckman, J. Duffie, „Evaluation of hourly tilted surface radiation models”, Solar Energy 1990, 45:9-17
- Reich-2004 N.H. Reich, W.G.J.H.M. van Sark, E.A. Alsema, S.Y. Kan, S. Silvester, Weak light performance and spectral response of different solar cell types, 19th European Photovoltaic Solar Energy Conference and Exhibition Paris, 7-11 June 2004
- Rodrigues-2010 E.M.G. Rodrigues, R. Melício, V.M.F. Mendes and J.P.S. Catalão, Simulation of a Solar Cell considering Single-Diode Equivalent Circuit Model, 2010
- Ross-1976 Ross RG. Interface design considerations for terrestrial solar cell modules. Proceedings of the 12th IEEE photovoltaic specialists conference, Baton Rouge, LA, November 15–18; 1976. p. 801–6.
- Sauer-1994 Untersuchungen zum Einsatz und Entwicklung von Simulationsmodellen für die Auslegung von Photovoltaik-Systemen, DU Sauer – Diploma thesis, TH Darmstadt, 1994
- Schittich-2007 Schittich, C., Staib, G., Balkow, D., Schuler, M., Sobek, W., Glass construction manual (2nd edition), Birkhäuser Publishers, Basel, p. 102., ISBN 3-7643-6077-1, 2007
- Schmid-1995 Jürgen Schmid, Transparente Wärmedämmung in der Architektur. Materialien, Technologie, Anwendungen, 120 S. 21



cm, Kartoniert/Broschiert Müller (C.F.), Heidelberg, 1995, ISBN 3-7880-7485-X

- Schler-2003      Schuler, C., Einfluss des Materialverhaltens von Polyvinylbutyral auf das Tragverhalten von Verbundsicherheitsglas in Abhängigkeit von Temperatur und Belastung. (2003).
- Shen-2010      Y.-L. Shen, Constrained deformation of materials: devices, heterogeneous structures and thermo-mechanical modeling, Springer US; Auflage: 1st Edition. (20. August 2010), ISBN-10: 1441963111
- Sidelev-2011      Alexander Siedele, Untersuchungen des thermophysikalischen Verhaltens von PV-Bauelementen bei verschiedenen Einbausituation, Masterarbeit, Universität Kassel, 2011
- Skoplaki-2009      E. Skoplaki, J.A. Palyvos, Operating temperature of photovoltaic modules: A survey of pertinent correlations. Renewable Energy 34 (2009) 23-29.
- Sobek-1998      Sobek, W., Kutterer, M., Messmer, R.: Rheologisches Verhalten von PVB im Schubverbund. Forschungsbericht 4/98. Institut für Leichte Flächentragwerke, Universität Stuttgart 1998.
- Sobek-2000      Sobek, W., Kutterer, M., Messmer, R.: Untersuchungen zum Schubverbund bei Verbundsicherheitsglas – Ermittlung des zeit- und temperaturabhängigen Schubmoduls von PVB. Bauingenieur 75, S. 41–46, 2000
- Stultz-1978      Stultz JW, Wen LC. Thermal performance testing and analysis of photovoltaic modules in natural sunlight. DOE/JPL LSA task report 5101-31; 1977.
- Sunrise-2008      EU-SUNRISE Project, Barriers for the introduction of Photovoltaics in the building sector, 2008

Swinbank-1963	Swinbank, W.C.: Long-Wave Radiation from Clear Skies. Quarterly Journal of the Royal Meteorological Society 89 (1963).
Tiwari-2006	Arvind Tiwari, M.S. Sodha, Performance evaluation of solar PV/T system: An experimental validation, Solar Energy, Volume 80, Issue 7, Pages 751–759, July 2006,
Tonui-2008	J.K. Tonui, Y. Tripanagnostopoulos; Performance improvement of PV/T solar collectors with natural air flow operation; Solar Energy, Volume 82, Issue 1, January 2008, Pages 1–12
Trinurak-2009	Piyatida Trinuruk, Chumnong Sorapipatana, Dhirayut Chenvidhya, Estimating operating cell temperature of BIPV modules in Thailand, Renewable Energy 34 (2009) 2515–2523
Tsutsui-2005	J. Tsutsui , K. Kurokawa, Comparison of system performance measuring several types of PV modules./ 20 <sup>th</sup> European photovoltaic solar energy conference, 2005
TÜV-1984	TÜV-Rheinland: Atlas über die Sonnenstrahlung in Europa. TÜV-Verlag, 1984
Ultrasonic-2011	Ultrasonic Sensors – Online catalog – 2011-11-23, <a href="http://www.microsonic.de/DWD/_111327/pdf/1033/microsonic.pdf">http://www.microsonic.de/DWD/_111327/pdf/1033/microsonic.pdf</a>
Waermeatlas-2008	VDI Wärmeatlas : Wärmeübergang durch freie Konvektion in geschlossenen Fluidschichten – Teil Fc. and Ka, 2008
WBCSD	World Business Council for Sustainable Development <a href="http://www.wbcsd.org/work-program/sector-projects/buildings/overview.aspx">http://www.wbcsd.org/work-program/sector-projects/buildings/overview.aspx</a>
Weller-2009	Weller, B., Hemmerle, C., Kothe, M., “Testing procedures for building integrated photovoltaics”, 24 <sup>th</sup> European Photovoltaic Solar Energy Conference, Hamburg, Germany, 21-25 September 2009,

Weißner-1998	M. Weißner, O. Menges, „Multifunktionale Photovoltaik-Fassade im Vergleich – funktional und wirtschaftlich“, Berufspraktische Studienarbeit, Kassel 1998
Wellershoff-2007	Wellershoff, F., Bemessungsschubmodulwerte für Verbundglas-scheiben, Stahlbau 76 (2007), Heft 3
Widjaja-2009	Widjaja, Eddy ; Holschemacher, Klaus ; Schneider, Klaus-Jürgen, “Baustatik – einfach und anschaulich: Baustatische Grundlagen, Faustformeln, neue Wind- und Schneelasten”, 2009
Wrigger-2008	Peter Wriggers, Nonlinear Finite Element Methods; Springer, 2008; ISBN 3540710000
Yamada-2001	Takao Yamada, Hiroyuki Nakamura, Tadatoshi Sugiura, Koichi Sakuta, Kousuke Kurokawa, Reflection loss analysis by optical modeling of PV module, Solar Energy Materials and Solar Cells, Volume 67, Issues 1–4, March 2001, Pages 405–413

#### Standard and Building Codes

EN 12488	Glass in building - Glazing requirements - Assembly rule – 2003-09
ISO 12567	Thermal performance of windows and doors - Determination of thermal transmittance by hot box method; 2009,
VDE 0126-21	Photovoltaic in building, 2007
EN 13363-2	Solar protection devices combined with glazing - Calculation of solar and light transmittance - Part 2: Detailed calculation method; 2005,
DIN 18008	Glas im Bauwesen – Bemessung- und Konstruktionsregeln – Teil 1 & 2, 2006
EN 410	Glass in building - Determination of luminous and solar characteristics of glazing; 2011,

DIN 4108-2	Wärmeschutz und Energie-Einsparung in Gebäuden – Teil 2: Mindestanforderungen an den Wärmeschutz; 2003
EN 50530	Overall efficiency of grid-connected photovoltaic inverters; En%0530:2010
IEC 61215	Crystalline silicon terrestrial photovoltaic (PV) modules – Design qualification and type approval (IEC 61215:2009)
IEC 61646	Thin-film terrestrial photovoltaic (PV)modules – Design qualification and type approval (IEC 61646:2009)
EN 61853	Photovoltaic (PV) modules performance testing and energy rating, Part 1: Irradiance and temperature performance measurements and power rating; part 2: spectral response, incidence angle and module operating temperature measurements (IEC-61853:2010)
ISO 6946	Building components and building elements – thermal resistance and thermal transmittance – calculation method (ISO-6946-2007)
EN 673	Glass in building - Determination of thermal transmittance (U value) - Calculation method; 2011,
EN 674	Glass in building – determination of thermal transmittance (U-value) – Guarded hot plate method; 2011
TRLV	Technische Regeln für die Verwendung von linienförmig gelagerten Verglasung; TRLV; 2006